CHAPTER 1

INTRODUCTION

1.1 Overview of the Schlieren Technique

Flow Visualization in its broadest terms represents any technique used to recognize the motion of the fluid and extract additional information about the flow by making the flow visible. The 15th century, Leonardo Da Vinci is believed to be the pioneer in flow visualization quest by sketching a turbulence of water jet issuing from a square hole to a pool [1]. Figure 1.1 shows the Leonardo Da Vinci's half art half science sketch of free water jet turbulence.

Understanding flow characteristics using visualization has tremendously progressed in association with optical imaging technology. The advents of optical apparatuses such as lenses and concave and convex mirrors made by Robert Hooke in the 17th century helped to visualize gaseous inhomogeneous media for the first time.

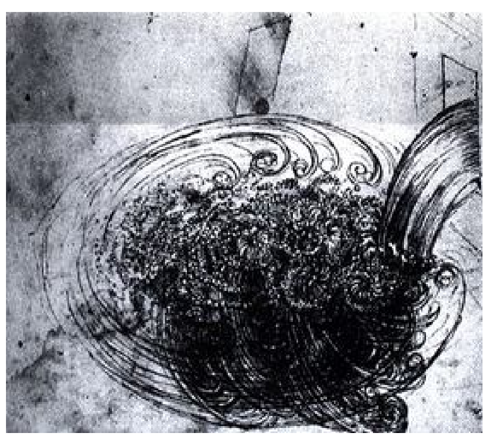

Figure 1.1: Leonardo Da Vinci's water jet visualization sketch [1]

Hooke used two candles and a lens to visualize thermal air disturbance against a distant dark boundary by a human eye. He used one candle as a light source to illuminate the concave lens to the eye of the observer. The second candle flames was placed near the lens and refracted some light rays so that they fell outside the pupil and were blocked [2]. This resulted in the visualization of the convective plume of the candle due to the changes in intensity. This Hooke's technique of visualizing optical inhomogeneities is considered as the first ever made Schlieren setup.

Schlieren is an expression which is derived from a German word 'schliere' which means 'streaks' [3]. Schlieren are optical inhomogenities in the transparent material resulting from localized differences in the optical path length causing light deviations [4]. Figure 1.2 shows Hooke's first Schlieren system and a candle plume image recorded by adapting Hooke's setup.

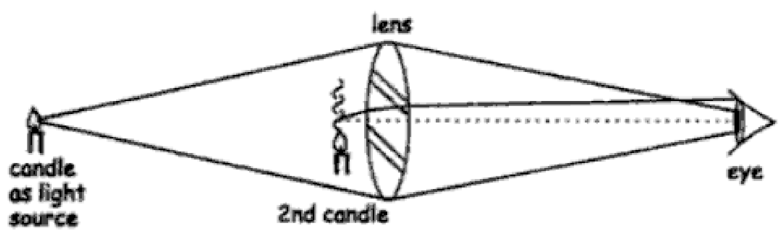

Figure 1.2: Hooke's Schlieren setup [2]

Despite Hooke's primary endeavour on studying optical heterogeneous media, August Toepler was acclaimed as the principal developer of the conventional Schlieren system. Toepler prepared optical devices such as Knife edge cut-off, Lantern Light source, long focus lens and a telescope for viewing the image to facilitate his Schlieren setup [2]. Toepler had also investigated the convection from his hand against air temperature differences within 1^{o}C and the effects of light diffraction using his setup. Figure 1.3 shows Toepler's original Schlieren Apparatus.

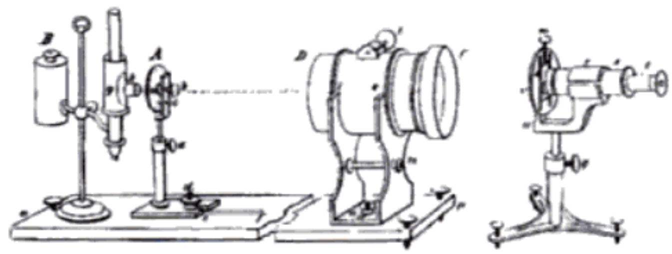

Figure 1.3: Toepler's Schlieren apparatus [2]

Hubert Scharadin's exploration in the field of high speed physics and media of inhomogenities enlightened the 20th century research on the Schlieren technique. He discussed how the working principles and applications of the conventional Schlieren technique could be employed. According to Settles [2], since Scharadin's PhD dissertation and his publication "Schlieren Methods and Their Applications" [5] the publication rate in the area of optics of inhomogenities increased from a handful of yearly publications to hundreds of papers per year.

Figure 1.4 shows the basic working principle of a conventional Schlieren system. Light rays, from the point source (S), are colliminated by the first lens (L1) into parallel rays which pass through the flow field. When there are no inhomogeneities in the field the light rays travel undisturbed through the media until they encounter the second lens (L2) which focuses them back down to a point which is recorded as bright regions in the image plane. In cases where there are inhomogenities (change in indexes of refraction) the light rays are refracted slightly. This effect will cause these refracted light rays not to be focused down to a point by the second lens. The refracted rays are blocked instead by the knife edge or the filter causing a darker region to be recorded in the Schlieren image.

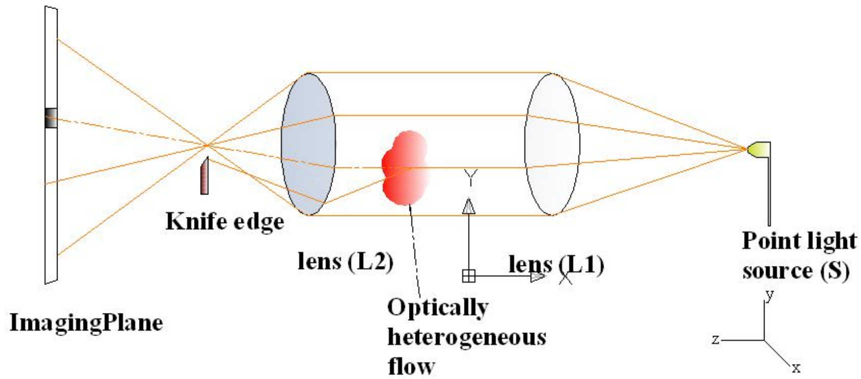

Figure 1.4: Conventional Schlieren setup.

These light beam deflections caused by the optical inhomogenities (change in flow structure) provides information about the index of refraction and hence the density of the media. Nowadays, the Schlieren technique has various applications in glass technology, aerodynamics, ballistics, heat transfer and convection studies, explosion and shockwave research, gas leak detection, boundary layer studies, and combustion research [6 and 7].

1.2 Problem Statement

Since 1999's BOS invention, the technique has been applied in various applications such as density field measurements, blade tip vortex estimation and heat convection profile study. However, all the flow fields studied under BOS are transparent and assumed to have uniform lighting conditions. In addition, most of the light deflection algorithms were originally developed for PIV technique which assume a pure translation motion of pixels in certain correlating windows.

This research has attempted to extend BOS imaging to different lighting conditions so as to allow the technique to be able of measuring any flow media with variable intensity. Moreover, a pure translation motion in a pixel and its immediate neighbourhood assumption doesn't give good results for large correlating windows. In this thesis, an optical flow equation which takes the change in intensity into account and an estimation motion model that considers both translational and rotational deflections are developed.

Velocity field of a flow is usually measured by light sheet techniques such as PIV and LDA. The light sheet techniques utilize sheet illumination from a tunable, pulsed laser source with a right angle detection of the scattered light using a solid state array detector. However, light sheet techniques have certain shortcomings. To mention some:

1. They require a powerful laser illumination source together with sheet forming optic and an imaging system consisting of 2D photo detector collection optics. This equipment requirement makes these tools quite expensive.

2. The experimental setup tasks are more complex than the line of sight methods and calibration of these methods is also rather difficult

3. Most of this light visualization techniques require flow seeding. Ensuring uniform seeding of the whole flow under visualization is not easy. Moreover, the main drawback of seeding is that the tracer particles may not follow the flow trajectories especially for compressible fluid flows which can result in false data.

4. The use of high power laser beams raises health-safety issues.

In this thesis, an alternative velocity field measurement technique based on BOS data is shown. The other problem this research tackles is the difficulty of extracting multiple thermodynamic parameters from single dataset. This project proposed a method, which gives accurate quantitative results of temperature, species concentration and velocity for varying density flows at any flow speed.

1.3 Research Objective

The objective of this research was to develop a quantitative Schlieren method in order to measure multiple thermodynamic parameters: species concentration, temperature and velocity. Finding out these parameters helps to understand various behaviours of the flow in various fields of research such as oil and gas research, aerodynamics, explosion and shockwave research.

In order to achieve the objective of the research the following original contributions were made:

1. A novel light deflection vector estimation using wavelet basis functions was developed.
2. Multiple thermodynamic parameters were extracted from a single experimental data set.
3. Velocity vector fields were determined from the quantitative Schlieren data.

1.4 Scope of the Research

This research addressed both reacting and non reacting axi-symmetric flows only. But the results of this study can easily be extended to any type of flow by employing additional image recording setup.

This research specially addressed the following issues:

1. The developed deflection vector estimation model must work for any variable flow lighting conditions. Unlike many digital correlation algorithms, the developed model considered both rotational and translational displacements of the background feature.
2. The reconstructed density information was based on optical tomography. Since all the flow setups used under this study were assumed and verified as axi-symmetric flows, a single-view image was taken and projected in all direction during reconstruction.
3. Three different gaseous flows were used for investigating the developed tool. These flows were injected compressed natural gas, open methane flame and round hot air jet.

1.5 Research Methodology

Experimental data collection, mathematical model development, and algorithm preparation to extract thermodynamic parameters were the paramount tasks of this project. A wavelet based background was recorded by a high speed camera with and without the different flows mentioned in Section 1.4. Based on the correlation made by a pair of images using the mathematical model and algorithms developed, the temperature, concentration and velocity fields of the flow were extracted. To support the huge amount of calculations required a computer code was developed in MATLAB.

The detailed research methodology is discussed in Chapters 3 and 4. Figure 1.5 shows the basic steps adopted as a methodology to corporate this research.

As shown in the Figure 1.5, the methodology followed can be categorized as experimental data collection, image processing and thermodynamic parameters extraction. The experimental data collection procedure includes collecting Background Oriented Schlieren (BOS) data of a CNG jet, methane flame, and hot air jet. A validation experiment of thermocouple and hot wire anemometry readings are conducted. The image processing task includes developing a new optical flow algorithm that computes the deflection vector of the background features and reconstructing index of refraction using computed tomography. The index of refraction field is used to calculate density temperature and velocity of a flow. Temperature and velocity results are compared with thermocouple and hot wire anemometry readings.

1.6 Thesis Outline

This thesis is divided into six chapters. Chapter 1 briefly defined the Schlieren method and described the problem statement, research objective and scope of the research. The second chapter reviews the existing optical visualizing methods and their working principles. The chapter also provide detailed coverage on Schlieren techniques and it’s supporting theories and models. Chapter 4 describes the theoretical background and the modified mathematical modelling. The developed mathematical model focuses on deflection vector estimation; wavelet based optical flow model and its algorithm design, index of refraction data reconstruction and thermodynamic parameter extraction. The fourth chapter expresses the experimental setups used in this study. Chapter 5 discusses the results obtained. The last chapter draws conclusions and delivers recommendations for future work.

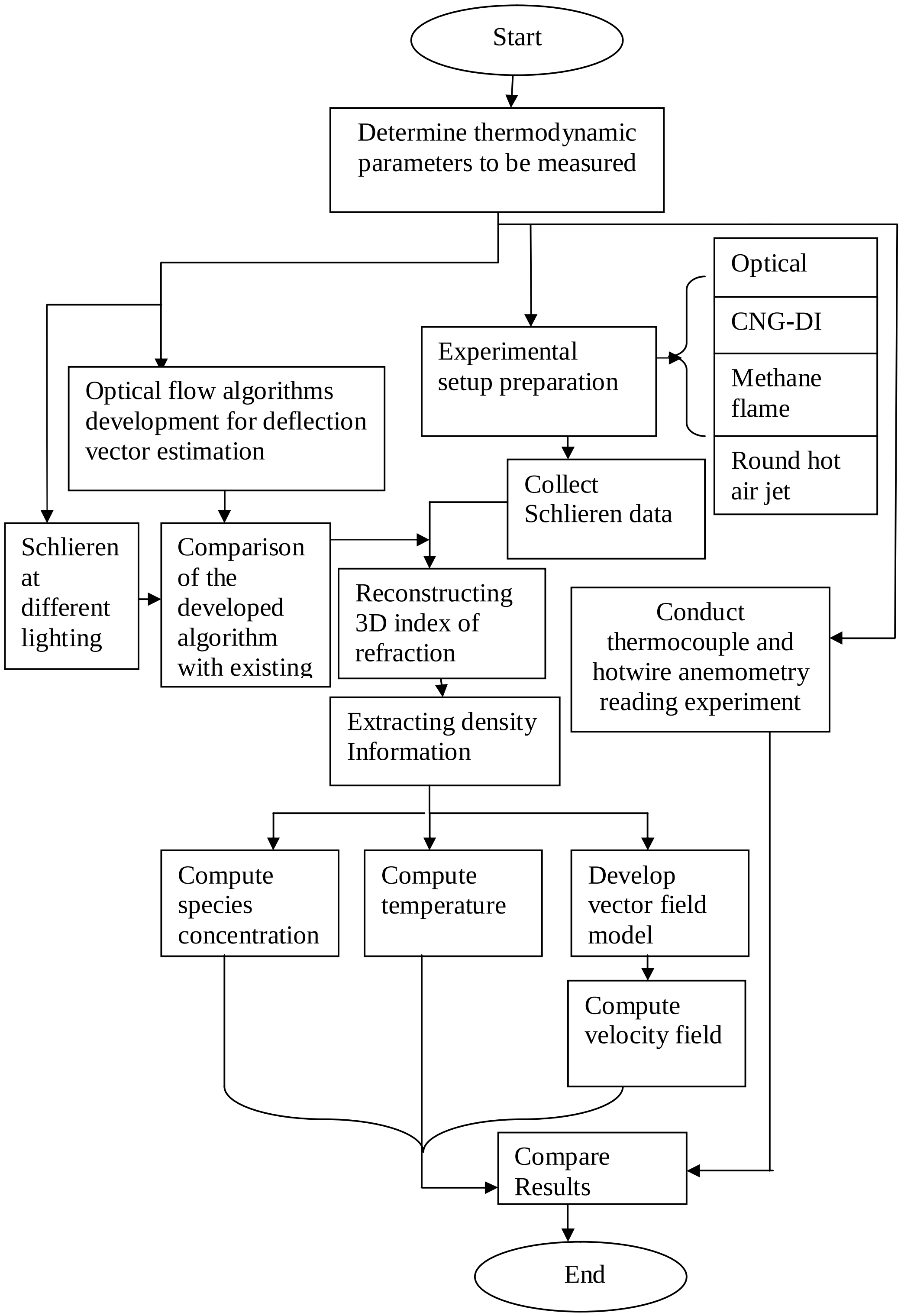

Figure 1.5: Flow diagram of the research methodology

CHAPTER 2

LITERATURE REVIEW

2.1 Introduction

In this chapter various flow visualization techniques are discussed. These tools are divided into two categories; geometric (macroscopic), and thermodynamic parameters measurements. Conventional Schlieren is usually used to provide qualitative information and/or geometric flow parameters. In contrast, quantitative Schlieren is typically employed for thermodynamic parameters measurements like density and temperature. In this chapter, detail coverage of the background, working principles and applications of Background Oriented Schlieren (BOS) technique is presented since this technique was used in the current study to extract quantitative multiple thermodynamic parameters.

2.2 Geometric Flow Parameters Measurement

Recently many direct photographic imaging and image processing experiments were conducted to measure macroscopic gaseous and fuel vapor flow parameters. These flow parameters include flow penetration length, near- and far-field angles, flow bulk velocity, average gas area density, fuel area expansion and flow-symmetry. The most common techniques of macro spray parameters are direct photographic imaging and the conventional Schlieren technique. Since the majority of these geometric parameter measurements are frequently used in the areas of combustion and engine research, some important contributions made by researchers in this field are mentioned below.

Endoscopic digital camera imaging was implemented by many researchers to image sprays and flame evolution. The spray imaging required external illumination as it is non luminous. Pastor *et. al,* [8] identified the sources of errors and uncertainties for these systems as optical distortion, illumination orientation and repeatability, perspective distortion, window fouling and spray segmentation. They used software that corrected the optical distortion of the spray segmentation and calculations of the geometrical parameters. By using the Red-Green-Blue (RGB) values of the flame images the temperature of flame was obtained.

Sellens *et. al,* [9] developed a non orthogonal optical spray pattern analysis to give an alternative for camera positioning, especially for cases where it would be practically impossible to put the camera directly downstream from the spray nozzle. However, this system requires a perspective and intensity corrections in order to find the final spray parameters.

Shao and Yan. [10] and Shao and Yan [11] described the application of a direct photographic imaging and image processing system for the quantitative characterization of diesel sprays. A high-resolution CCD camera with a flashlight source was used to capture images of sprays in an optically accessible constant volume chamber. They developed image processing software which is capable of spray segmentation, outline extraction and parameter quantification. Using this system, they studied the effects of varying injection pressure, chamber pressure and type of nozzle on spray parameters- tip penetration, spray angle, fuel area density, and spray tip velocity.

Petit *et. al.* [12] made a direct visualization a diesel spray image re-centering by using logarithmic average. They calculated a different symmetry axes based on grey levels of the plume or on the plume boundary. They used the logarithmic distance to characterize the spray plume internal symmetry.

Video imaging was used to explore the characteristics of diesel sprays [13]. An Nd:YAG pulsed laser was used as the illumination source for an optically accessible engine and shadowgraphy was employed to find the spray penetration with respect to time and spray cone angle at different injection pressures.

2.3 Thermodynamic Flow Parameter Diagnostic Tools

Density, temperature, flow velocity, species concentration and pressure are the universal parameters to describe the thermodynamic behaviour of a flow.

Eckberth [14] and Mielke [15] rigorously surveyed optical thermodynamic parameters measurement techniques such as: Laser Induced Florescence (LIF), Rayleigh Scattering, Raman Scattering and Coherent Anti Stokes Raman Spectroscopy (CARS). Other techniques which provide thermodynamic flow parameters are Laser Doppler Velocimetry (LDV) Particle Image Velocimetry (PIV), Background Oriented Schlieren (BOS) and Color Schlieren.

All these methods can be divided into Molecular and Particle flow diagnostic techniques. An outline of frequently used thermodynamic optical flow visualization tools are shown in Table 2.1.

2.3.1 Molecular Based Techniques

Molecular based techniques involve either elastic (non-energy exchanging) or inelastic (energy-exchanging) light scattering processes from atoms or molecules. Since the gas molecule properties are directly determined without involving seeding, these techniques are capable of providing gas temperature and density information which couldn’t be found using particle-based techniques [16]. These techniques includes: Rayleigh scattering, Raman scattering, Coherent Anti-Stokes Raman Spectroscopy (CARS), Laser-Induced Fluorescence (LIF), Laser-induced gratings, Molecular tagging techniques, Diode laser absorption and Collective light scattering.

When a laser beam is passed through a gas, the molecules cause inelastic and elastic light scatterings. The inelastic scattering is called Raman scattering and the elastic one is known as Rayleigh scattering. Three popular molecular based techniques (Rayleigh scattering, Raman scattering and laser induced fluorescence) principles’ and applications’ are discussed in Sections 2.3.1.1 to 2.3.1.3.

Table 2.1: overview of optical diagnostic tools

Optical measurement	Scientific approach	Major equipments	Measured Parameters
Rayleigh Scattering,	Detecting elastic scattered light when light sheet meets atoms/molecules	Laser beam source, Signal detectors, Additional optical apparatuses	Density, Velocity, Temperature
Raman Scattering	Detecting in-elastic scattered light when light sheet meets atoms/ molecules	Laser beam source, Signal detectors, Additional optical apparatuses	Species-concentration Temperature
Coherent Anti Stokes Raman Spectroscopy (CARS)	Two laser beams of different wavelength interact inside flow and create a third beam with different wavelength. The shape of the spectral signature and the intensity of the third beam is used to measure flow parameters.	Laser beam with pulse durations of the order of 10 ns Signal processor and detectors	Species-concentration Temperature
Planar Laser induced Flouresence (PLIF)	Laser light resonance with species wavelength excites atoms/ molecules to higher electronic energy states light is emitted when these molecules relax back to a lower energy state.	Laser beam ,CCD Camera, seed generator, optical filter	Species-concentration Temperature, Velocity, Pressure
Laser-Doppler Velocimetry (LDV)	By Measuring Doppler's frequency shift from the difference between the frequencies of the received and incident laser which is scattered from a moving particle velocity can be calculated	Continuous laser beam photo detector, a signal receiver and processor, Additional optical aparatuses	Velocity and Turbulence
Particle Image Velocimetry (PIV)	the scattered light from illuminated particles is recorded at different times and correlating the particles' positions in pair of frames gives velocity and turbulence vectors	Laser beam, CCD, Camera, seed generator, Optical filter	Velocity and Turbulence
Phase Doppler Interfero-metry (PDI)	The difference between the received and incident laser light is used to measure particle diameters	Continuous laser beam photo-detector, signal receiver and processor, Additional optical- apparatuses	Droplet size and velocity
Background Oriented Schlieren (BOS)	Light beam refraction due to change in the refraction index is measured using deformation of background images	Light source, high-frequency background, Camera	Density, concentration Temperature
Rainbow schlieren	The light beam refraction due to a change in the refraction index is measured using color change of the recorded images	Light source, graded filter, camera	Density, concentration Temperature

2.3.1.1 Rayleigh Scattering

Rayleigh scattering is the elastic scattering of light from molecules or atoms with dimensions much smaller than the wavelength of the light, where the signal strength, Doppler frequency shift, and spectral line width of the scattered light provide measurements of density, velocity, and temperature, respectively [15]. A typical Rayleigh scattering setup is shown Figure 2.1

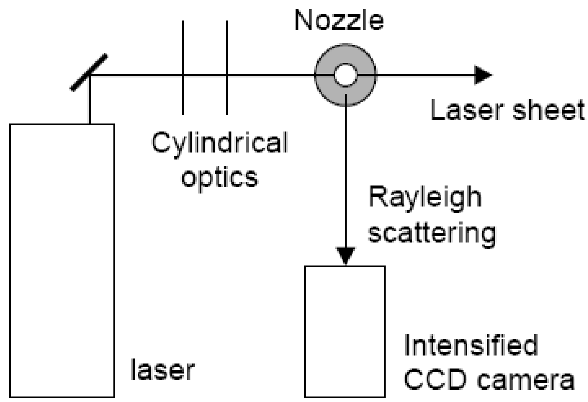

Figure 2.1: Rayleigh scattering Setup [17]

Forkey *et. al* [16] presented experimental results using Filtered Rayleigh Scattering to make planar measurements of velocity, temperature and pressure in ambient air and in a Mach 2 free jet. When the scattered light is imaged directly by a camera, all frequency information is lost and the intensity at each pixel will be a measure of the local flow density only. If, on the other hand, the light is imaged through a notch frequency filter, the signal at each pixel will also be a function of the flow velocity, temperature and pressure, due to the overlap between the scattered line shape and the filter notch.

Dam [17] used Rayleigh scattering of ultra-violet laser light as a diagnostic tool to record gas density distributions in a supersonic nozzle flow. An intensified CCD camera with ultra violet objective lens was used to record the Rayleigh scattered light in a direction perpendicular to the light sheet.

In 2003, an air density measurement system based on molecular Rayleigh scattering was built in a large nozzle test facility at NASA Glenn Research Center [18]. The applied technique used light scattered by gas molecules present in air and no artificial seeding was added. Light from a single mode, continuous wave laser was transmitted to the nozzle facility through optical fibbers, and light scattered by gas molecules, at various points along the laser beam, was collected and measured by photon-counting electronics.

Mielke [15] claimed that simultaneous measurements of gas temperature, velocity and density were achieved using molecular Rayleigh scattering. The experimental set up contained Fabry- perot Interferometer and four different photo multiplier tubes (PMT).

2.3.1.2 Raman Scattering

Like Rayleigh scattering, the Raman scattering depends upon the polarizability of the molecules. For polarizable molecules, the incident photon energy can excite vibrational modes of the molecules, yielding scattered photons which are diminished in energy by the amount of the vibrational transition energies [19]. In contrast to Rayleigh scattering some of the molecules will be radiated with a frequency other than the incident beam frequency. This phenomenon is called inelastic scattering.

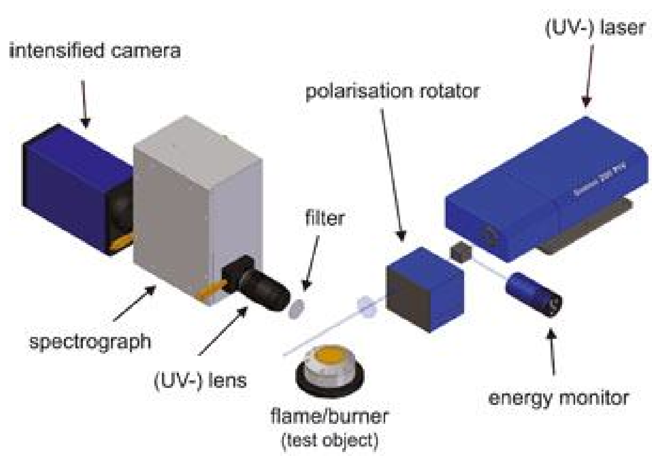

Figure 2.2: Raman scattering setup [20]

A Raman Radiation scattered with a frequency lower than that of the incident beam is known as stokes radiation, while a radiation of a higher frequency than that of the incident beam is called anti-stokes [21].

2.3.1.3 Laser Induced Flouresence(LIF)

LIF, sometimes called as PLIF (an acronym for planar laser induced fluorescence), methods can be used to measure concentration, temperature, velocity, and pressure quantitatively. When the laser wavelength is resonant with an optical transition of a species in the flow some of the laser light is absorbed. This effect excites the absorbing molecules or atoms to higher electronic energy states resulting in re-emission of light at a different wavelength from the incident illumination. This occurrence is referred to as fluorescence. The measured spectral properties of the fluorescence depend on the temperature, pressure, velocity, and species concentration of the flow field. The fluorescence signal is usually recorded by photomultiplier tubes for point measurements or charge-coupled devices (CCDs) for planar measurements. Filtering is often necessary to eliminate stray laser light and background light [15].

Paa *et al*. [22] used a tuneable, thin-disk laser with a 1 kHz repetition rate and pulse energies in the 5 mJ range to excite and measure turbulence of OH radicals. Jiang [23] demonstrated NO PLIF imaging at greater than 100 kHz repetition rate in a Mach 2 jet using a megahertz repetition rate pulse-burst laser system. This laser setup was developed at the Ohio State University in combination with a Princeton Scientific Instruments' ultra-high frame rate camera.

Verbiezen. *et. al* [24] presented LIF applications for measuring local in-cylinder NO concentration in a heavy duty diesel engine. Quantitative concentration histories during the combustion stroke were also shown.

2.3.2 Particle Based Techniques

As the name implies, particle based measuring techniques make use of light reflection (Mie scattering) by seeding particles when a light beam passes through the flow in order to measure flow parameters such as velocity and turbulence. Laser Doppler anemometry (LDA), Planar Doppler Velocimetry (PDV) and Particle Image Velocimetry (PIV) are the more frequently used particle based measuring techniques.

2.3.2.1 Planar Doppler Velocimetry (PDV)

Elastically scattered light from particles entrained in the flow and illuminated by a stable-frequency narrow line width laser light sheet is imaged through an atomic or molecular vapor filter. The Doppler shifted light is split into two paths; one path is imaged directly and in the other the light is imaged through the molecular filter. It is a common practise to image both the reference and signal images side by side on a single CCD detector. PDV is suitable for high velocity measurements because of its good spatial resolution, whereas its short comings are the complexity of multi component system and high cost [15, 25, and 26].

2.3.2.2 Particle Image Velocimetry (PIV)

PIV is one of the most commonly used flow velocity measurement techniques. Particles in a flow are illuminated by a double-pulsed laser and the scattered light is collected by a camera at right angle to the light sheet in double frames. By correlating the particles' positions in the two frames within the given time interval the velocity vector can be calculated. A single CCD camera gives an in plane (two dimensional) velocity vectors. Three component measurements have also been demonstrated using conventional PIV for the in-plane velocity components and a planar Doppler technique for the out-of-plane component [27].

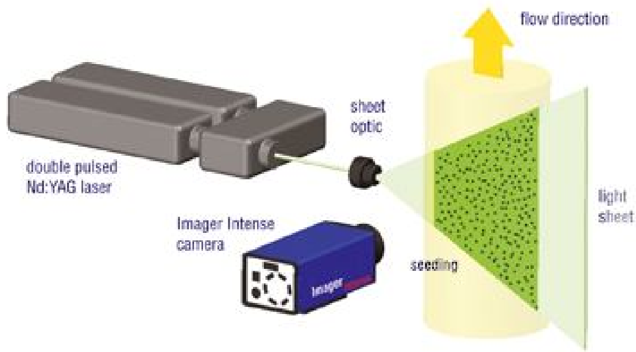

Figure 2.3: PIV setup [21]

2.3.2.3 Laser Doppler Annemometry (LDA)

Laser Doppler anemometry is based on the Doppler shift of laser light scattered from small particles carried along with the moving fluid. The incident and scattered light wave directions define the direction of the measured velocity component. LDA crosses two beams (usually generated by splitting a single beam) of collimated, monochromatic, and coherent laser light in the flow field. The two beams are made to intersect at their focal point so as to generate a set of straight fringes. The sensor is then aligned to the flow such that the fringes are perpendicular to the flow direction. When particles pass through the fringes, they reflect light from the regions of constructive interference into a photo detector, and since the fringe spacing is known, the velocity can be calculated. [28].

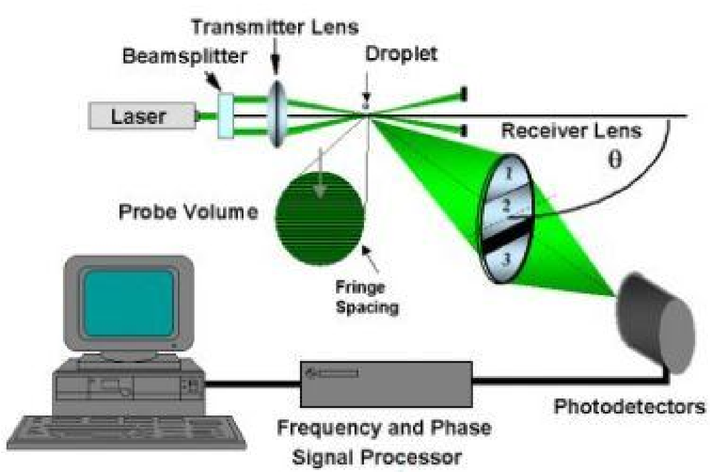

Figure 2.4: LDA/ PDI setup [21]

2.3.2.4 Phase Doppler Interferometry (PDI)

PDI uses a similar setup as LDA and can be used to measure the diameter and velocity of small droplets. It is based on the laser light wavelength which is known to high accuracy. The particle sizing is independent of light intensity so attenuation and window contamination have a minimal effect on drop sizing performance [20]. Figure 2.4 shows typical PDI setup.

2.4 Quantitative Schlieren

Quantitative Schlieren methods are capable of measuring the light deflection angles in two spatial directions, and the spatial integration returns the projected density gradient field. Qualtitative Schlieren techniques, which deal with inspecting Schileren photos or flow geometric data, fail to provide data like gas density, concentration temperature or velocity information. Studies made by Schardin [5] and Skotinov [29] discussed different quantitative Schlieren methods used for gas dynamics study.

2.4.1 Color Schlieren

Applications of color coding or using color contrast in Schlieren photography provide additional information on density gradients and directions. A color Schlieren system comprises of a small aperture (slit) with a matching color filter on a conventional Schlieren set-up. These color filters label each deflected ray with different hue according to its deflected angle instead of blocking the deflected light rays as in the conventional Schlieren technique. The recorded color Schlieren image, which depends on the light ray path taken to get there, gives quantitative information on the light deflection angle at each point in the image [30]. Oren *et. al* [31] described color Schlieren as a useful method of visualizing combustion flow because of its sensitivity and ability to respond to a range of gradients allowing one to visualize a flame and simultaneously detect fluid motion in the surrounding gases.

Color Schlieren techniques can be classified either by the shape, number, and orientation of the color filters or the aperture hole. Settles classified these techniques into thirteen different categories [32]. In this study, the two most commonly used Color Schlieren methods: Rainbow and Bullseye Schlieren are reviewed.

In 1896, Rheinberg [33], replaced a knife edge by a cut-off filter with concentric color rings, which are also called bullseye, to make a color contrast in the flow field. Ghoneiem [34] implemented Rhienberg's concentric circular rings of different color (bullseye) for the measurement of vorticity structures in turbulent combustion fields. A tricolor Bulleseye Schlieren was used to visualize and study premixed and diffusion flames in an unsteady swirling flow within a cylinder [31].

Rainbow Schlieren follows the same working principle as bulleseye Schlieren, but it uses a special type of filter which contains different bands of color with the hue smoothly varying in a single direction. Howes [35] deviced the first applicable Rainbow Schlieren setup by replacing the ordinary Schlieren knife edge cut-off with a radial rainbow filter having a transparent center and an opaque surround. Howes studied rainbow Schlieren's practical applications for measuring thermodynamic parameters (temperature and density) for more than 15 applications including air jet and flames. Furthermore he claimed his method as a good way for the quantitative measurement based on the change in the index of refraction [35, 36].

Greenberg *et.al.* [37] developed the rainbow schlieren defelectometry which had a color filter that was represented by a unique hue using HSI (Hue, Saturation, Intensity) model. This color filter of linearly varying hue was placed in the position of the cutting edge. The light deflected by the density variation in the test section passed through the color filter at a different point creating a unique Hue on the image plane. The other notable contribution made by Greenberg's work was their use of an iterative procedure to optimize the filter such that the filter transmissivity curve was linear [30, 37]. This procedure was followed to provide a uniform change in hue which resulted in a uniform sensitivity.

Butuk [38] used rainbow schilieren to measure temperature in a heated air jet using a computer-generated continuously graded filter.

The measured deflections were inverted to reconstruct the three dimensional temperature field of a hot air jet using computer tomography. Al-Ammar *et.al* [30] used rainbow schilieren deflectometry to measure oxygen concentration in discharged helium. Both authors [30, 38] compared and achieved a good agreement between the Rainbow Schlieren measurements with probe sampling data. They pin pointed increasing the sampling interval without introducing under-sampling or signal aliasing was vital for accurate Schlieren reconstructions.

Both Butuk [38] and Al-Ammar *et.al.* [30] used a color filter having a varying Hue line spectrum along the width. This gave the values of displacement and gradients of index of refraction along one direction only. Figure 2.5 shows the rainbow filter used by Al-Ammar *et.al.*

Figure 2.5: Rainbow Schlieren filter [30]

Wu *et. al* [39] developed a light source with digital color filter on a computer and projected it by an LCD projector. The projected light was mixed with a diffusing lens to produce a white light source. Due to the change in the index of refraction a different color images were recorded by the CCD camera. However the paper did not discuss the digital color filter calibration and its application to provide quantitative flow information.

Cross beam rainbow Schlieren was implemented to measure turbulent flows such as low density gas injection on far field region and the combustion processes by Satti [40]. Crossbeam rainbow Schlieren deflectometry was used to measure thermodynamic scalar properties across the three fields (Laminar, transition, turbulent).

Satti [40] and Agrawal [41] developed a miniature rainbow deflectometry which was capable of providing scalar measurements at high spatial resolution. This miniature rainbow deflectometry was used to probe micro-scale fluid flows and also to aid in resolving the finest scales of turbulence in jets and flames.

2.4.2 Laser Schlieren

Verma [42] used low powered (15 W) laser diode. The light passing through the test section was received by an array of Photodiodes placed on the opposite direction of the shock wave. The photo diode contained 16 element linear silicon PIN photo diode array. When the laser sheet touched a test area, the diffracted light appeared periodically and a time trace obtained from the array of photo diodes showed unsteady voltage signal, which was correlated to the fluctuating density field.

Buttsworth [43] designed a low cost pulsed current circuit which to drive LED's in Schlieren flow visualization systems. Though quantitative flow visualization was not incorporated in this technical paper, samples of visualization results obtained with hot air jet were presented.

The other applications of lasers in a Schlieren set up is to minimize optical aberrations specially astigmatism and coma. Increasing the accuracy of optical setup is required to minimize these aberrations. Setting a Schlieren system to peak accuracy is a time consuming task. Laser alignment was used to locate the correct position and orientation of Schlieren apparatuses in order to increase the accuracy of optical alignment [44].

2.4.3 Background Oriented Schlieren (BOS)

BOS works by recording a high frequency background image which is placed behind flow field to be studied. A calibration background image is recorded without the flow field. Based on the translation vector of the background feature on the pair of images (recorded with and without the flow field), the index of refraction of the flow can be computed. The direct relationship between the refraction index and density of a fluid can be used to measure the density and other thermodynamic parameters of the flow.

Meier [45] and Dalziel [46] invented a quantitative Schlieren technique that measured the density variation which was used to measure mainly scalar flow parameters and they named it “Background Oriented Schlieren (BOS)” and “synthetic Schlieren” respectively. Though, Settles [47] argues the correct name for the tool should be “Synthetic Background-Distortion Schlieren Imaging.” Since the commonly used term for this technique by flow visualization researchers is the name proposed by Meier [45], in this research this quantitative Schlieren measurement is referred as “Background Oriented Schlieren.”

Preliminary studies on Background Oriented Schlieren by [48-50] have shown several possible applications of BOS; these include density fields of helicopter-generated vortices, gas flames and supersonic jets, but these studies were predominantly qualitative with no comparisons with existing qualitative measurements or thermodynamic or fluid dynamics theories.

Venkatakrishnan and Meier [51] developed a three dimensional density distribution of an air jet by using computed tomography. They computed the index of refraction as a line integral and based on filtered back projection algorithm, they developed a 3-dimensional density field. Goldhahn and Seume [52] considered projections taken with BOS as gradient information and showed the possibility of directly employing a computed tomography to the deflection measurement of BOS. Leopold [53, 54] attempted to apply a color background pattern in order to increase the BOS system resolution. Eight different color patterns were extracted from the colored background and the assessment of image deformation for all 8 patterns was achieved separately. Averaging with the aid of standard deviation criterion was used to achieve an increased accuracy. The colored BOS measurements gave good result when compared with numerical simulation data. But the measurements superiority in accuracy over the monochromatic BOS technique was not investigated. Feng *et. al.* [55], Venkatakrishnan and Meier [51] implemented inverse tomographic algorithms which could extract two dimensional slices of index of refraction or density fields from a three dimensional flow.

Klinge et al [56] have performed BOS in combination with PIV measurements in order to derive quantitative flow velocity and density data of a wing tip vortex. Klinge [57] further extended Meier's [51] work by developing a technique to measure a velocity field of incompressible flow by using the density field of a fluid parcel as a marker but this method worked for flow velocity of Mach 0.3 and below only. This was because beyond this velocity limit the compressibility effect varied the density of the flow and it becomes difficult to trace particles based on their density.

The first task in BOS data processing is to find the angular deflection vectors of the refracted light beams. Earlier literatures show that most of the deflection vector computation was performed by PIV like region based optical flow techniques. Atcheson *et. al*. [58] compared different optical flow techniques for BOS vector calculation. In general, the computer vision community classified the optical flow techniques as differential techniques, region based matching, phase based methods and energy based techniques [59]. Differential techniques estimate the motion by studying the intensity gradient of the first and second order spatial and temporal derivatives. Research works by Horn and Schunck [60] and Lucas and Kanade [61] are considerd as pioneer approaches of solving optical problems using the differential techniques. In most BOS and PIV evaluations, region based matching was the most commonly used motion estimation technique. Phase-based methods work by an initial decomposition of the image into band-pass channels with multi-scale representation. This technique is stable for certain extents of changes in mean intensity and contrast. Energy based correlation, on the other hand, fundamentally works on the output energy of displacement based filters [62]. Brox *et. al* [63] used the main energy function minimized for the computation of optical flow as a combination of appearance and smoothness terms of the time-lagged pair of images globally.

Liu *et. al* [64] used a multi resolution approach of hierarchical representation of the images to solve an optical flow based on differential techniques. Rakshit and Anderson showed the trade-off between accuracy and computation cost was largely dependent on the redundancy of the image representation [65]. Pan *et. al*, on the other hand, proposed an optical flow algorithm that utilizes a correlation-feedback technique [66].

Vaseduva *et. al* [67] and Meier [68] implemented elliptical partial differential equation (Poisson equation) to estimate a two dimensional index of refraction. Klinge used an Abel inversion method, a tomographic technique for axi-symmetric flow, to find the local density of a wind flow from the measured deflection angle. Kindler *et.al* [55] Goldhahn *et.al* [52] Venkatakrishnan and Meier [51] used filtered back projection reconstruction techniques to calculate three-dimensional density distributions of a gas flow. Three-dimensional information reconstruction techniques are discussed in the next chapter. The major Researchers' important contributions towards the current BOS technology are shown in Table 2.2.

Table 2.2: Researchers' and their role towards today's BOS

Authors / year	**Contributions**	**Constraints**
Schardin/1942 [4,5]	Presented refractive objects to be based on their distortion of a patterned background.	Provide qualitative measurements only
Koepf /1972 [69]	Measured density field by using the displacement of a laser speckle pattern caused by a candle flame.	---
Meier/ 1999 [45]	Invented and applied for BOS patent	Provide qualitative measurements only
Dalizel/1999 [46]	Reported BOS as 'Synthetic Schlieren'	Qualitative measurements only
Sutherland *et. al*/1999 [70]	Attempted measuring density and velocity fields of internal waves in a stratified fluid using 'synthetic Schlieren'	The light deflection integratedalong the optical path and provide 2 dimensional measurement only.
Richard *et. al* /2000 [48]	Attempted to investigate BOS applications in a supersonic jet, a turbulent flame, and the blade tip vortices a helicopter	Provide qualitative information only
Augensteine *et.al*/2001 [71]	Compared BOS with holographic filters	---
H Richard and M Raffel /2001 [49]	Demonstrated usage of BOS to study compressible vortices of a helicopter blade	Provide qualitative measurements only
Klinge *et.al* 2002 [72]	Measured local density information of a helium jet by means of BOS	Used an Abel inversion reconstruction technique, a technique susceptible to noise

Table 2.2: Table 2.2: Researchers' and their role towards today's BOS. Continued...

Authors / year	Contributions	Constraints
Elsinga *et. al* /2003 [73]	evaluated and compared applications of BOS and color Schlieren	---
Klinge *et. al*/2003 [56]	Used BOS and PIV to measure velocity and density data of a wing tip vortex generated by an airfoil. Computed optimum BOS setup. Used 'Abel Inversion' to reconstruct refraction index	Velocity was measured using the PIV technique. BOS was used to measure density only
Venkatakrishnan and Meier/ 2004 [51]	Used inverse tomographic algorithms to reconstruct two-dimensional slices from a three-dimensional flow over a cone cylinder model	They have used poisson equation to compute density field. But since the measurements taken with the BOS-Method are gradient information, they that can directly used into the filtered back projection algorithm [52]
Goldhahn and Seume/2007 [52]	Studied the sensitivity, accuracy and resolution of BOS in 3D density fields. Computed 3D density field directly from deflection angle using computed tomography.	Only density fields were measured.
Leopold/2007 [53]	Applied color background pattern in order to increase the BOS system resolution.	No comparison of results with other methods were made
Kindler et. al/2007[74]	Applied BOS and computed Tomography to study rotor blade tip vortex measurement	----
Baur and Tapee /2008 [75]	Studied system sensitivity and the effective distances among BOS apparatuses	No thermodynamic parameters were measured
Berger *et. al*/2009 [76]	Presented a 4D (3D and time) resolved gas volume information using BOS.	No thermodynamic parameters were measured No comparison of results with other methods were made
Atcheson et.al/2009 [58]	Assessed optimum optical flow algorithm for deflection vector estimation in BOS.	-----
Hargather and. Settles/2010 [77]	Used natural background for BOS measurement.	----
Bichal and Thurow / 2010 [78]	Studied the effects of sensitivity and correlation window on BOS	No thermodynamic parameters were measured

2.5 Summary

This chapter reviewed the significant developments in the field of optical flow diagnostic technology. It was shown that, most of the current state of the art measuring techniques are light sheet based techniques. These tools use high-tech apparatus particularly laser beam setup and signal detectors. In addition to the complexity of these tools, the price of these apparatus being expensive was the major motivation of this research to look at other optical tool options. Quantitative Schlieren and more specifically the Background Oriented Schlieren were considered as an alternative tool to the light sheet based methods. Our review showed that Background Oriented Schlieren was a promising tool to measure several thermodynamic parameters. From this survey, it is concluded that, a further improvement in deflection vector estimation algorithm and a mathematical model can help to extract multiple thermodynamic parameters from single BOS data set. The next chapter is devoted to carry out these two tasks.

CHAPTER 3

THEORY AND MATHEMATICAL MODELLING

3.1 Introduction

In this chapter, the theoretical background and the mathematical model developed to extract multiple thermodynamic parameters using Background Oriented Schlieren (BOS) are discussed. Methods like BOS and Rainbow Schlieren investigate the deformation of the recorded images due to the flow field being studied, and compute the deflection (deformation) vectors. Once the deflection vector is obtained, by inverting geometric optics equation, the index of refraction of the flow can be found. The direct relationship between the index of refraction of the flow and density helps to further extract additional flow parameters.

This chapter discusses the theoretical background and the developed deflection vector estimation algorithm. Index of refraction and flow parameters extraction are computed based on the deflection vector estimation in the following subsections.

3.2 Theoretical Background

The basic principle of BOS is based on the evaluation of image variations due to changes in the refractive index of the propagating medium. An image is a convolution between its target object (the background feature) and the transfer channel (intermediate media). A change in one of these two parameters changes the image captured by the camera. BOS exploits this phenomenon by comparing images with normal and disturbed transfer channel. The background usually made of high frequency features which allow tracking a slight deflection of the light recorded by the camera. The background feature can be developed as random dots or intentionally placed features in transparency or any material that allows light passage. In this research, a wavelet noise is used as background. The advantages and principles of using wavelet noise background is discussed in Section 4.3.2

The basic BOS setup is shown in Figure 3.1. The camera records pairs of images of the background image with and without the intermediate flow. The deflection of the background features created due to the flow can be computed by optical flow techniques. The numbers 1 to 5 in Figure 3.1 represents camera, background pattern, flow, Data acquisition system and the light source respectively.

1. Camera
2. Background pattern
3. Flow
4. Data acquisition system
5. Light source

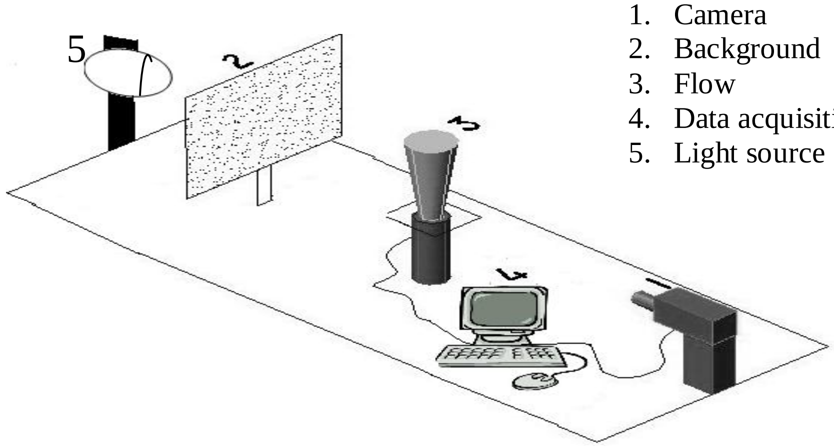

Figure 3.1: BOS setup

During deflection vector estimation, local neighbourhood approximation and image down-sampling using wavelet like basis functions were used by researchers [64] in order to alleviate the ‘aperture problem.’

In this study, wavelet basis functions are used to down-sample images. Down-sampling is a technique of reducing sampling rate of an image so as to acquire more compact and less resolution images. Wavelets are finite windows through which the signal can be viewed. In order to move the window about the length of the signal, the wavelets can be translated about time in addition to being compressed and widened. The wavelet transform provides signal decomposition onto a hierarchical set of basis functions. The discrete wavelet transform is an efficient frame work to store a multi resolution images and it also gives a powerful insight into an images spatial and frequency characteristics [79].

Each level of wavelet decomposition creates four types of images: One approximation image and three detail horizontal, vertical and diagonal images. In this study, the approximate image is repeatedly decomposed using wavelet transform to achieve successive approximation coefficients. Figure 3.2 shows one stage wavelet decomposition of the input image.

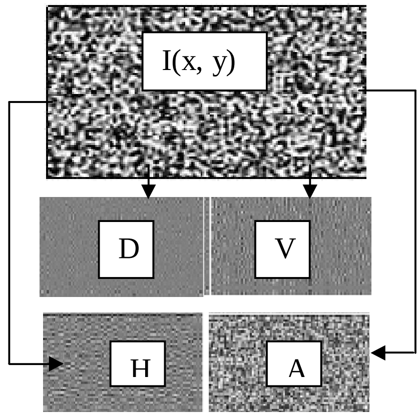

Figure 3.2: Discrete wavelet transform image decomposition

As shown in the Figure 3.2 the the background image has been decomposed into different types of image details. A represents the coarse approximation of *I (x, y)*. H, V and D are detail sub-images, which represent the horizontal, vertical and diagonal directions of the image *I (x, y)*.

The distinctive wavelet behaviors of separablity, scalability, orthogonality and multi resolution compatibility [79] are ideal properties to solve the optical flow problems in multi resolution analysis. Low frequency components are decomposed to the next pyramidal level. Each level ends up by providing an optical flow equation. Decomposing the low frequency components is recurred until a sufficient number of equations are obtained to extract displacement vectors.

The deflection vector can be easily converted into light beam angular deflection in accordance with relative positions between apparatuses in BOS setup and focal length of the camera lens.

3.3 Light Beam Deflection Vector Estimation

Light is a form of electromagnetic radiation in which any or all of its characteristics may be altered when it is transmitted through transparent medium due to the interaction with the medium [80]. Light and optical phenomena can be treated in either physical optics or geometric optics [81].

Fermat's principle states that the path taken between two points by a ray of light is the path of least time [82]. Fermat's principle and index of refraction n, which is the ratio of light speed in a vacuum c relative to the light speed in the medium v, define the law of light refraction or Snell's law [83]. Snell's law states that the ratio of the index of refraction of the media and the sines of the angles of incidence is constant and depends on the characteristics of the media [84]. Figure 3.3 shows the light ray refraction as the medium in which the light passes change.

$$n_1 \sin \theta_1 = n_2 \sin \theta_2 \tag{3.1}$$

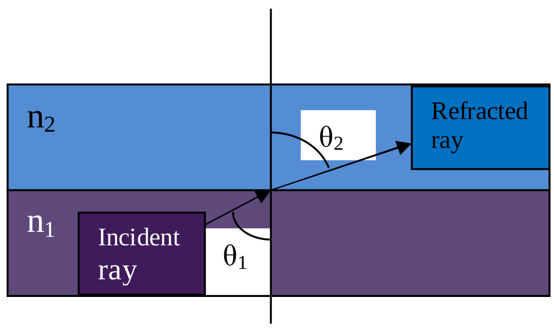

Figure 3.3: Principle of light refraction

Physical optics (wave theory) states light wave's wavelength, an intermediate between long radio waves and short x-rays, as sufficiently short so that it can be observed as rectilinear motion [80]. Geometrical light rays can be defined as rays orthogonal to surfaces with equal optical path length (L) [85]. These surfaces are called wave fronts.

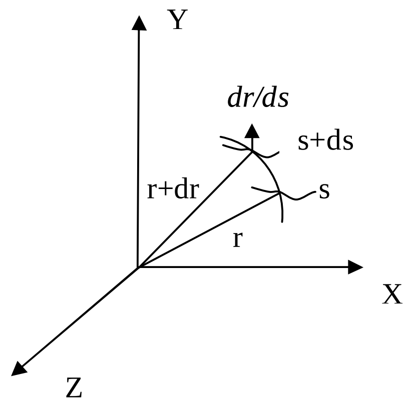

Figure 3.4: Wave fronts of a light beam

The geometrical-optics limit of maxwell's equation (Equation 3.2) states the square of the gradient of optical length ∇L is equal to the index of refraction of the media.

$$[\nabla L(r)]^2 = n(r)^2 \tag{3.2}$$

As it is shown in the Figure 3.4 the wave front is represented by an arc length of s and position vector r. It can be seen that dr/ds is a tangent unit vector to the ray curve, and Equation 3.2 becomes

$$\nabla L = n \, dr/ds \tag{3.3}$$

The differential equation of geometric ray can be derived by using directional derivative of ∇L with respect to dr/ds as Equation 3.4. The derivation of Equation 3.4 is shown in Appendix A.

$$\frac{d}{ds}\left(n \, dr/ds\right) = \nabla n \tag{3.4}$$

The following two assumptions were considered [2, 4, and 7].

1. parallel illumination in the *x* and *y* directions of the understudy flow with no change in lighting condition along the optical axis in *z* direction of Figure1.4.
2. the displacement of the light beam inside the media from its original rectilinear path is negligible.

Hence, Equation 3.3 is simplified and the well known relationship between gradients of index of refraction and deflection vector of light rays is obtained [2].

$$\frac{\partial^2 x}{\partial z^2} = \frac{1}{n}\frac{\partial n}{\partial x}$$
$$\frac{\partial^2 y}{\partial z^2} = \frac{1}{n}\frac{\partial n}{\partial y} \tag{3.5}$$

Integrating Equation 3.5 along the optical axis (z) provides geometric ray deflection angle (ε_x and ε_y) provides

$$\varepsilon_x = \frac{1}{n}\int \frac{\partial n}{\partial x}\partial z$$
$$\varepsilon_y = \frac{1}{n}\int \frac{\partial n}{\partial y}\partial z \tag{3.6}$$

An accurate extraction of the deflection vector field from the pair of background images is the first and the most important task of BOS image processing. Optical flow techniques are used to compare the change (displacement) of the background features created due to the inhomogeneity of the media. Optical flow is a technique which deals with tracking specific features (points) in an image across multiple frames taken at t and $t+\delta t$ at every pixel position [59].

In a 2D plane image, a certain point of spatial coordinates x and y recorded at time t with image intensity I moves by δx and δy at time $t+\delta t$. This situation can be described as image constraint equation [67]:

$$I(x, y, t) = I(x+\delta x, y+\delta y, t+\delta t) \tag{3.7}$$

Taylor series can be applied in Equation 3.7 if the deflection vectors are assumed to be small:

$$I(x+\delta x, y+\delta y, t+\delta t) = I(x, y, t) + \frac{\partial I}{\partial x}\delta x + \frac{\partial I}{\partial y}\delta y + \frac{\partial I}{\partial t}\delta t + H.O.T. \tag{3.8}$$

H.O.T. stands for higher order terms. Combining Equations 3.7 and 3.8 and truncating higher order terms gives:

$$\frac{\partial I}{\partial x}\delta x + \frac{\partial I}{\partial y}\delta y + \frac{\partial I}{\partial t}\delta t = 0 \tag{3.9}$$

Assuming $\delta t = 1$ for simplicity purpose and replacing $\frac{\partial I}{\partial x}$ by I_x and $\frac{\partial I}{\partial y}$ by I_y $\frac{\partial I}{\partial t}$ by I_t :

$$I_x \delta x + I_y \delta y = -I_t$$

Or (3.10)

$$\nabla I^T . \overline{X} = -I_t$$

where $\overline{X}$ represents angular deflection vector

The single Equation 3.10 holds two unknown sets of vectors namely: δx and δy. In optical flow this situation is known as 'aperture problem.' Finding out the unknown deflection vectors requires another set of equations. All distinctive optical flow procedures supply additional constraints or conditions to determine the unknown flow motion.

In all BOS research works mentioned in the literature review, an optical flow method was used with its basic assumptions i.e, the global intensity of imaged points was invariant and the local motion was continuous. However, BOS background images are taken through a different index of refraction field compared to ambient air. For image intensity, which is a convolution between the background function and the transfer medium function, variation in global intensity value of background features is expected when the calibration (without flow) and BOS images are compared. In this thesis, the optical flow equation is modified to account for intensity variation and wavelet based image decomposition is used to solve the 'aperture problem'. The aperture problem is a condition where, the optical flow equations contain more unknowns than the number of equations. The other assumption used commonly in earlier optical flow techniques involves a pure translation motion in a certain neighbourhood. This assumption is modified in this research, by incorporating mathematical motion model that accommodates both translational and rotational shift of the background features.

In the following sub sections, the motion estimation model is derived and plugged into the basic optical flow equation. The optical flow equation is analytically solved by using wavelet based decomposition.

3.3.1 Estimating Motion

In most BOS experiments, the deflection vectors were computed under the assumptions that a certain pixel and its neighbourhood undergo a pure translation. This assumption works well if a small correlation window size is used. In PIV and other light sheet based techniques an interrogation window of less than 16 x 16 pixels is considered as small correlation window. Even though a small interrogation window provides a high resolution, it is affected by certain drawbacks. To mention some, since the pair of background features correlated is in small pixel areas, the deflection vector may result in low signal to noise ratio and smaller number of optical flow equations. These two conditions make smaller interrogation windows susceptible to noise and 'aperture problem' [86]. Losses of pairing and feature truncation are other problems that the small interrogation windows suffer [87].

A large interrogation window, on the other hand, provides a robust estimation but a pure translation motion of a certain pixel neighbourhood can't be assumed. In this thesis, to estimate the deflection motion, Affine-like motion model is used [63, 64]. Affine motion model represents translation, rotation, dilation and shear. This property gives flexibility for the estimation of the local Affine motion model as

$$\begin{pmatrix} \Delta x \\ \Delta y \end{pmatrix} = \begin{pmatrix} a & b \\ c & d \end{pmatrix} \begin{pmatrix} x \\ y \end{pmatrix} + \begin{pmatrix} e \\ f \end{pmatrix} \tag{3.11}$$

where *a, b, c, d* are rotation, shear and dialation terms, *e* and *f* are affine translation terms whereas Δx and Δy are deformation measured in the x and y directions. The deflection motion of BOS lies on the same background plane. This makes the rotational and translational motion estimation terms sufficient enough to model the deflection vector by simplifying the equation. Removing the shear and dilation coefficients and using single rotational coefficient simplifies Equation 3.11 as

$$\begin{pmatrix} \Delta x \\ \Delta y \end{pmatrix} = \begin{pmatrix} 0 & \alpha \\ -\alpha & 0 \end{pmatrix} \begin{pmatrix} x \\ y \end{pmatrix} + \begin{pmatrix} \mu \\ \upsilon \end{pmatrix} \tag{3.12}$$

where α is the rotational term and μ and υ are translation terms along x and y axis.

3.3.2 Incorporation of Intensity Variance

The fact that optical flow methods assume intensity invariance, renders them unsuitable for optical imaging techniques like BOS. Since image intensity is a convolution of the background function and the transfer medium function, the change in transfer medium affects the image intensity of the background object.

To alleviate this problem, an optical flow algorithm that takes into account the change of intensity variation due to the flow field is proposed. The original optical flow equation (Equation 3.7) can be re stated as

$$I_t(x,y,t) = I_{t+1}(x+\Delta x, y+\Delta y, t+\Delta t) \tag{3.13}$$

where x and y are spatial coordinates, t and $t+\Delta t$ represents successive frames and Δx and Δy are the spatial translations to be computed. Assuming the image intensity varies linearly, Equation 3.13 is modified by taking change in intensity variation into account as shown below.

$$AI_t(x,y,t) + B = I_{t+1}(x+\Delta x, y+\Delta y, t+\Delta t) \tag{3.14}$$

A and *B* are constants that multiply and add up to the original image intensity. Based on Taylor series, $I_{t+1}(x+\Delta x, y+\Delta y, t+\Delta t)$ can be written

$$I_{t+1}(x+\Delta x, y+\Delta y, t+\Delta t) = I_t(x,y,t) + \partial I/\partial x\,\Delta x + \partial I/\partial y\,\Delta y + \partial I/\partial t\,\Delta t + H.O.T \tag{3.15}$$

Substituting Equation 3.15 into Equation 3.14 and truncating higher order terms provides Equation 3.16.

$$(1-A)I_t(x,y,t) + \partial I/\partial x\,\Delta x + \partial I/\partial y\,\Delta y + \partial I/\partial t\,\Delta t - B = 0 \tag{3.16}$$

In order to solve the unknowns of Equation 3.16 (A, B, Δx and Δy), a wavelet based multi-resolution approach was followed. Mallet's [88] multi-resolution signal decomposition using wavelet basis was extended by Bernard [89] to propose a wavelet based multi-resolution optical flow estimation. Wavelets superior localization properties in both spatial and frequency domains and its orientation sensitive filters are the main reasons why wavelets can be used as powerful tools for motion detection algorithms.

Suppose $\psi_{u,s}{}^{l}$ represents a wavelet function whose shifts and rescalings form a basis function for $L^2(R^2)$. Shift and rescaling parameters are represented by u and s whereas l stands for the level of the transform. The modified optical flow Equation 3.16 can be represented as a weighted sum of a wavelet basis equation. The inner product between Equation 3.16 and the wavelet function can be written as:

$$\left\langle ((1-A)I_t(x,y,t) + \partial I/_{\partial x}\,\Delta x + \partial I/_{\partial y}\,\Delta y + \partial I/_{\partial t}\,\Delta t - B), \psi^{\,l}_{u,s} \right\rangle = 0\,,\ \ \forall l = 1 \ldots L^2 \tag{3.17}$$

L is the maximum wavelet transform level. Considering the bilinear properties of an inner product, Equation 3.17 can further be modified

$$\langle ((1-A)I_t(x,y,t)), \psi^{\,l}_{u,s} \rangle + \left\langle \partial I/_{\partial x}\,\Delta x, \psi^{\,l}_{u,s} \right\rangle + \left\langle \partial I/_{\partial y}\,\Delta y, \psi^{\,l}_{u,s} \right\rangle + \left\langle \partial I/_{\partial t}\,\Delta t, \psi^{\,l}_{u,s} \right\rangle - \langle B, \psi^{\,l}_{u,s} \rangle = 0 \tag{3.18}$$
$$\forall l = 1 \ldots L^2$$

3.3.3 Modifying Optical Flow Equation

The displacement vectors Δx and Δy of the background points are represented based on Affine motion model as mentioned in Equation 3.12. Δx and Δy in Equation 3.12 are given as:

$$\Delta x = \alpha y + \mu$$
$$\Delta y = -\alpha x + \upsilon$$

Putting this model in Equation 3.8 gives:

$$\begin{aligned} &\langle (1-A)I, \psi^{\,l}_{u,s} \rangle + \alpha \left\langle \partial I/_{\partial x}\, y, \psi^{\,l}_{u,s} \right\rangle + \mu \left\langle \partial I/_{\partial x}, \psi^{\,l}_{u,s} \right\rangle - \alpha \left\langle \partial I/_{\partial y}\, x, \psi^{\,l}_{u,s} \right\rangle \\ &+ \upsilon \left\langle \partial I/_{\partial y}, \psi^{\,l}_{u,s} \right\rangle + \left\langle \partial I/_{\partial t}\,\Delta t, \psi^{\,l}_{u,s} \right\rangle - \langle B, \psi^{\,l}_{u,s} \rangle = 0, \forall l = 1 \ldots L^2 \end{aligned} \tag{3.19}$$

Bernard and Mallat [88, 89] computed the inner product of two functions (suppose *f* and *g*) by integrating their convolution. Integrating *f**g* by parts has a unique property of:

$$\left\langle f, \frac{dg}{dx} \right\rangle = -\left\langle \frac{df}{dx}, g \right\rangle \tag{3.20}$$

This property further modifies Equation 3.19 as

$$\begin{aligned} &\left\langle (1-A)I, \psi^{l}_{u,s}) \right\rangle - \alpha \left\langle Iy, \frac{\partial \psi^{l}_{u,s}}{\partial x} \right\rangle - \mu \left\langle I, \frac{\partial \psi^{l}_{u,s}}{\partial x} \right\rangle + \alpha \left\langle Ix, \frac{\partial \psi^{l}_{u,s}}{\partial y} \right\rangle + \\ &- \upsilon \left\langle I, \frac{\partial \psi^{l}_{u,s}}{\partial y} \right\rangle + \left\langle \frac{\partial I}{\partial t} \Delta t, \psi^{l}_{u,s} \right\rangle - \left\langle B, \psi^{l}_{u,s} \right\rangle = 0, \forall l = 1 \ldots L^{2} \end{aligned} \tag{3.21}$$

Δt is the time difference between the successive frames. In this thesis it is taken as unity for simplification purpose. The temporal intensity derivative $\partial I / \partial t$ in Equation 3.21 was found using Horn-schunk derivative computation method [60]. Successive image frames were convolved by a filter f and added together.

$$\frac{\partial I}{\partial t} = I_{t} \otimes f \; + I_{t+1} \otimes (-f) \tag{3.22}$$

where $f = 0.25[1 \quad 1]$ and $\otimes$ stands for convolution.

The five unknowns (α, μ, υ, *A* and *B*) in Equation 3.20 were solved using multi- resolution analysis. The first task in the multi-resolution analysis was selecting the wavelet basis. Since this study was using wavelet transform for image down-sampling, not for reconstructing, compactly supported complex wavelets were used.

Wavelet decomposition was conducted for levels at least equal to the number of unknowns (which are 5). Figure 3.5 shows how the low frequency component images are decomposed at different levels. The approximation image and the three detail images created by wavelet down-sampling were presented shown in Figure 3.2. The size of the pair original images were 1280 x 512 pixels.

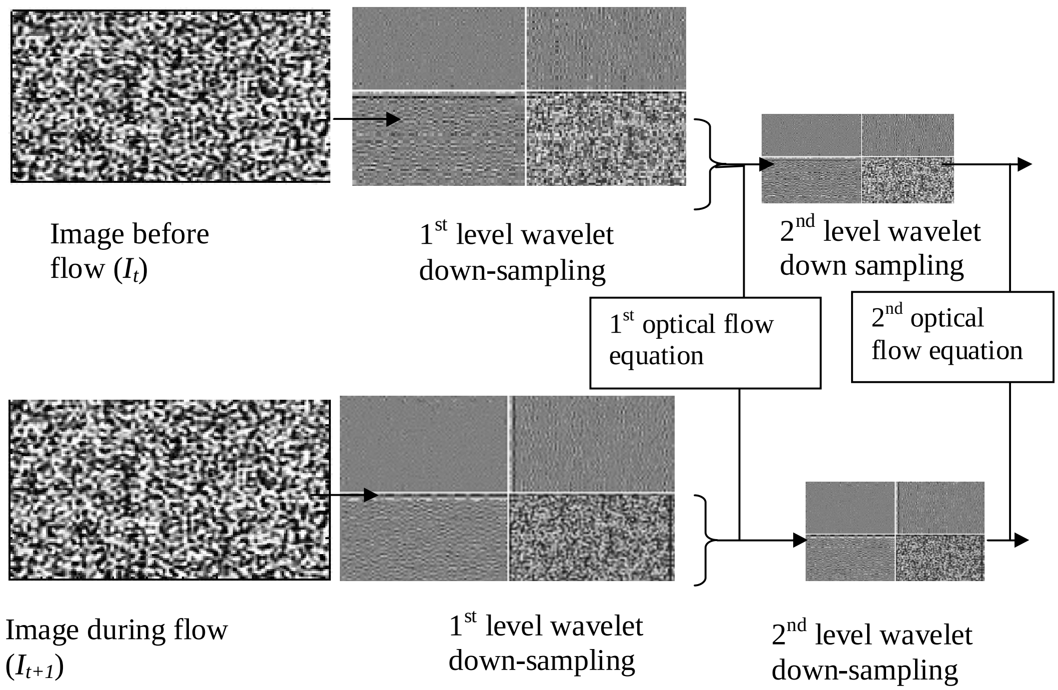

Figure 3.5: Approximate coefficients decomposition of 1280 x 512 pixels image

Each level provided one optical flow equation and this approximation coefficient decomposition were repeated until sufficient numbers of equations were obtained to solve the unknowns of Equation 3.21. The five levels of approximate images are shown in Figure 3.6.

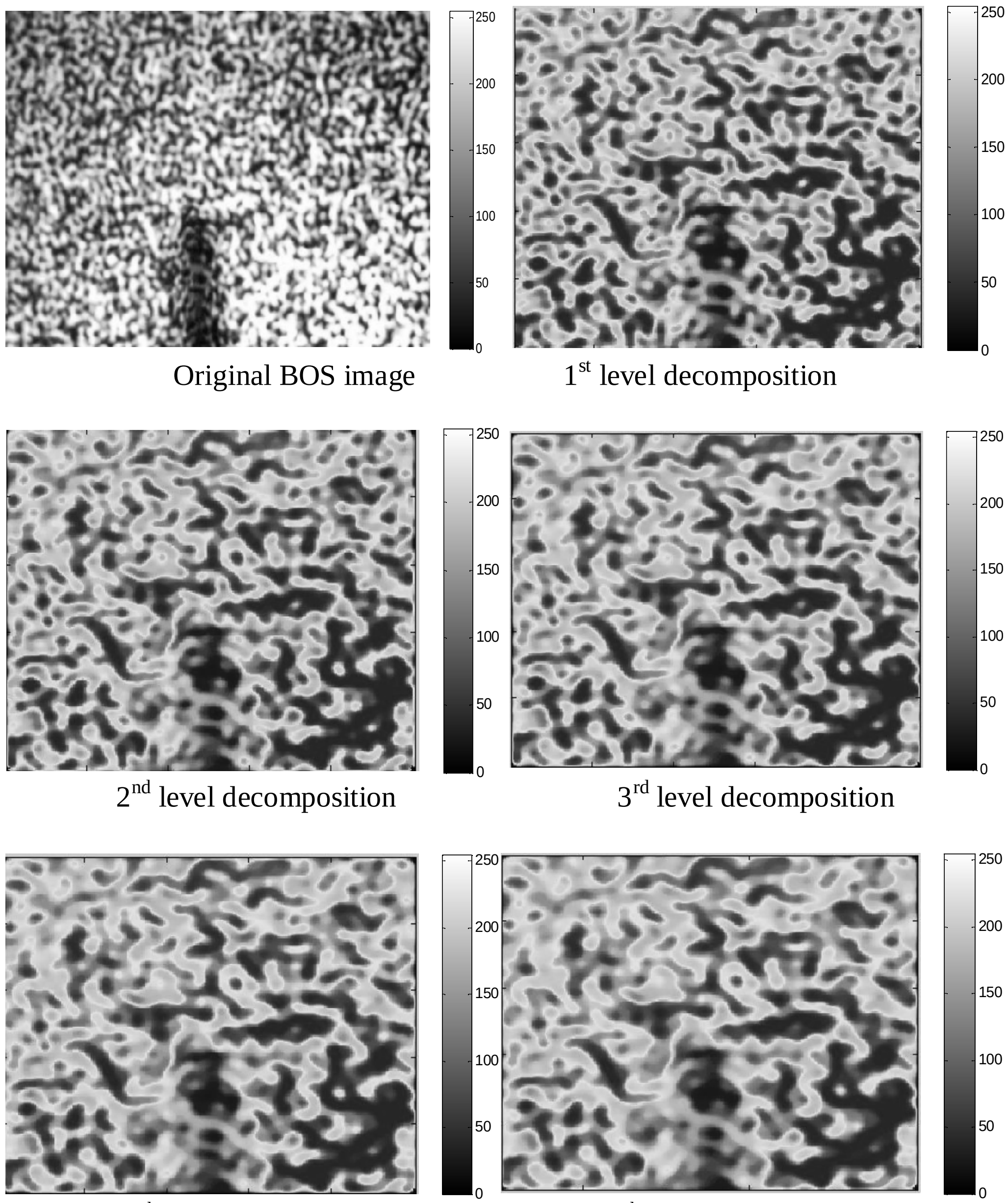

Original BOS image | 1^{st} level decomposition

2^{nd} level decomposition | 3^{rd} level decomposition

4^{th} level decomposition | 5^{th} level decomposition

Figure 3.6: The five levels of BOS image down-sampling of 1280 x 512 pixels image

Five decomposition levels were used to obtain the following five optical flow equations to find the five unknowns of Equation 3.21.

$$\left\langle (1-A)I_0,\psi^0_{u,s}\right\rangle - \alpha\left\langle I_0 y, \frac{\partial\psi^0_{u,s}}{\partial x}\right\rangle - \mu\left\langle I_0, \frac{\partial\psi^0_{u,s}}{\partial x}\right\rangle + \alpha\left\langle I_0 x, \frac{\partial\psi^0_{u,s}}{\partial y}\right\rangle + -\upsilon\left\langle I_0, \frac{\partial\psi^0_{u,s}}{\partial y}\right\rangle + \left\langle \frac{\partial I}{\partial t}\Delta t, \psi^0_{u,s}\right\rangle - \left\langle B,\psi^0_{u,s}\right\rangle = 0 \quad (3.23)$$

$$\left\langle (1-A) I_1, \psi_{u,s}^1 \right\rangle - \alpha \left\langle I_1 y, \frac{\partial \psi_{u,s}^1}{\partial x} \right\rangle - \mu \left\langle I_1, \frac{\partial \psi_{u,s}^1}{\partial x} \right\rangle + \alpha \left\langle I_1 x, \frac{\partial \psi_{u,s}^1}{\partial y} \right\rangle + -\upsilon \left\langle I_1, \frac{\partial \psi_{u,s}^1}{\partial y} \right\rangle + \left\langle \frac{\partial I}{\partial t} \Delta t, \psi_{u,s}^1 \right\rangle - \left\langle B, \psi_{u,s}^1 \right\rangle = 0 \quad (3.24)$$

$$\left\langle (1-A) I_2, \psi_{u,s}^2 \right\rangle - \alpha \left\langle I_2 y, \frac{\partial \psi_{u,s}^2}{\partial x} \right\rangle - \mu \left\langle I_2, \frac{\partial \psi_{u,s}^2}{\partial x} \right\rangle + \alpha \left\langle I_2 x, \frac{\partial \psi_{u,s}^2}{\partial y} \right\rangle + -\upsilon \left\langle I_2, \frac{\partial \psi_{u,s}^2}{\partial y} \right\rangle + \left\langle \frac{\partial I}{\partial t} \Delta t, \psi_{u,s}^2 \right\rangle - \left\langle B, \psi_{u,s}^2 \right\rangle = 0 \quad (3.25)$$

$$\left\langle (1-A) I_3, \psi_{u,s}^3 \right\rangle - \alpha \left\langle I_3 y, \frac{\partial \psi_{u,s}^3}{\partial x} \right\rangle - \mu \left\langle I_3, \frac{\partial \psi_{u,s}^3}{\partial x} \right\rangle + \alpha \left\langle I_3 x, \frac{\partial \psi_{u,s}^3}{\partial y} \right\rangle + -\upsilon \left\langle I_3, \frac{\partial \psi_{u,s}^3}{\partial y} \right\rangle + \left\langle \frac{\partial I}{\partial t} \Delta t, \psi_{u,s}^3 \right\rangle - \left\langle B, \psi_{u,s}^3 \right\rangle = 0 \quad (3.26)$$

$$\left\langle (1-A) I_4, \psi_{u,s}^4 \right\rangle - \alpha \left\langle I_4 y, \frac{\partial \psi_{u,s}^4}{\partial x} \right\rangle - \mu \left\langle I_4, \frac{\partial \psi_{u,s}^4}{\partial x} \right\rangle + \alpha \left\langle I_4 x, \frac{\partial \psi_{u,s}^4}{\partial y} \right\rangle + -\upsilon \left\langle I_4, \frac{\partial \psi_{u,s}^4}{\partial y} \right\rangle + \left\langle \frac{\partial I}{\partial t} \Delta t, \psi_{u,s}^4 \right\rangle - \left\langle B, \psi_{u,s}^4 \right\rangle = 0 \quad (3.27)$$

where I_L, for L equals to 0 to 4, is an averaged and lower resolution of the image I_0 which is created by computing trends along rows of I_0 followed by trends along columns.

In order to solve the wavelet partial differential equations and the intensity time differential term ($\frac{\partial I}{\partial t}$), the following procedures were followed.

1. Numerical forward differentiation is conducted to solve the spatial derivatives of wavelet down-sampling coefficients as shown in Equation 3.28.

$$\frac{\partial \psi_{u,s}^{l}}{\partial x} = \frac{\psi_{u_x+1,s}^{l} + 2\psi_{u_x,s}^{l} + \psi_{u_x-1,s}^{l}}{h^2}$$

$$(3.28)$$

$$\frac{\partial \psi_{u,s}^{l}}{\partial y} = \frac{\psi_{u_y+1,s}^{l} + 2\psi_{u_y,s}^{l} + \psi_{u_y-1,s}^{l}}{h^2}$$

   In Equation 3.28, a central explicit differentiation was performed. During the spatial derivatives computation of the wavelet coefficients, the right and left values of the shifting terms were used. The variable h is a small interval between successive coefficient values.

2. The image intensity time derivative was computed as shown in Equation 3.22.

3. The time difference (Δt) between the background images with and without intermediate flow taken to be unity. This assumption works well because the

time difference is only required when the rate of displacement (velocity) is studied.

Once all terms in Equations 3.23 to 3.27 are converted to numerical values, matrices of equation were developed. Equation 3.29 shows the global matrix equation of the developed mathematical model.

$$\begin{bmatrix} \left\langle I_L, \psi_{u,s}^L \right\rangle & \left\langle I_L, \frac{\partial \psi_{u,s}^L}{\partial x} \right\rangle & \left\langle I_L, \frac{\partial \psi_{u,s}^L}{\partial y} \right\rangle & \left\langle I_L, \frac{\partial \psi_{u,s}^L}{\partial x} \right\rangle & \left\langle I_L, \frac{\partial \psi_{u,s}^L}{\partial y} \right\rangle & \psi_{u,s}^L \end{bmatrix} * \begin{bmatrix} -(1-A) \\ \alpha y \\ \mu \\ -\alpha x \\ \upsilon \\ B \end{bmatrix} = \left\langle \frac{\partial I}{\partial t}, \psi_{u,s}^L \right\rangle \tag{3.29}$$

The discretization technique for solving time dependant differential equations stability criretia is computed as a function of h of Equation 3.28. The central explicit method is known to be numerically stable and convergent as long as $1/h^2 \leq 1/2$.

3.3.4 Algorithm Design

The algorithm shown in Figure 3.7 portrays the channel of procedures followed to compute the required deflection vectors. Sets of pairs of images with and without intermediate flow were loaded. Data enhancement was performed using median filters. This step helped to reduce the data size. The next step of the algorithm was initializing wavelet data sampling followed by computing the intensity temporal and spatial derivatives. This step was repeated until the number of equations equals the number of unknowns. The last step of the algorithm was estimating the deflection vectors based on the computed unknowns. The pseudo-code of the algorithm is shown in Appendix B.

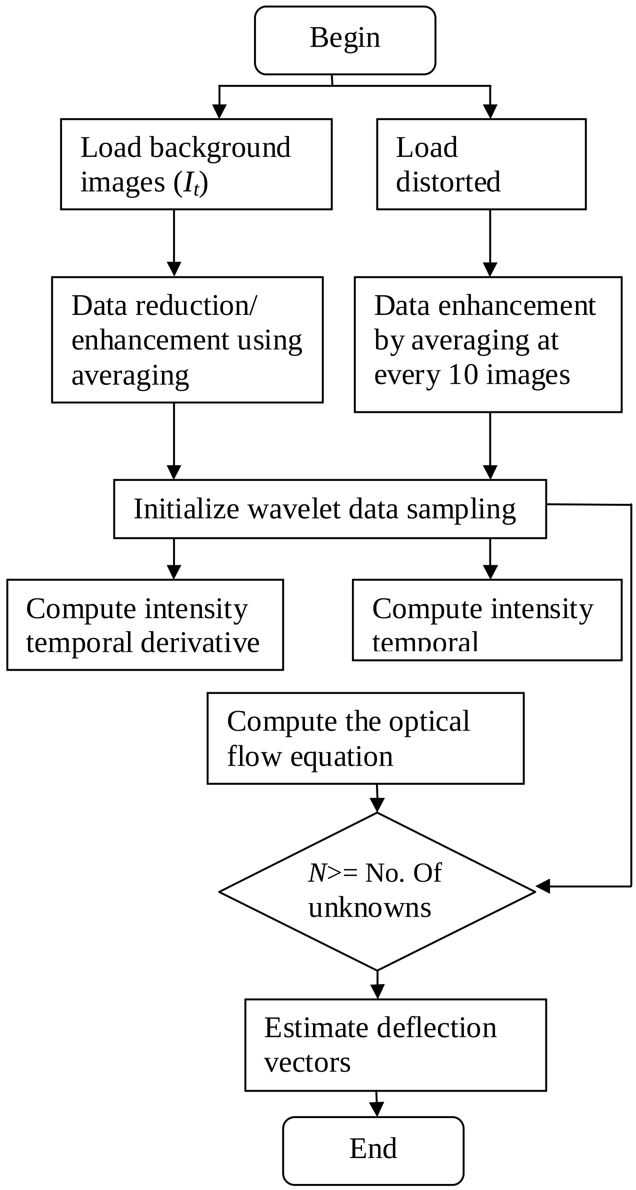

Figure 3.7: Algorithm of the optical flow estimation

The algorithm complexity was measured using floating point operation (flop). It is a common practise to assume optical flow maps in $O(N)$ flops, where N is the number of pixels.

The computational cost of the main procedures of wavelet image decomposition, pre-filtering and the wavelet and its' derivatives inner product with decomposed images are roughly estimated to be a function of $2N^2$-1. Whereas the cost of the array inversion and solving the linear system solution can be estimated as $4/3N^3$

$$flops = (2+2P)(2N^2-1) + \tfrac{4}{3}N^3 \tag{3.29}$$

$$\text{where } P = \begin{cases} 1, & \text{for algorithms either with intensity or motion correction model} \\ 2, & \text{for algorithms with both intensity and motion correction model} \end{cases}$$

The computational cost of the developed algorithm was compared with Bernard's for four different image sizes as shown in Figure 3.8.

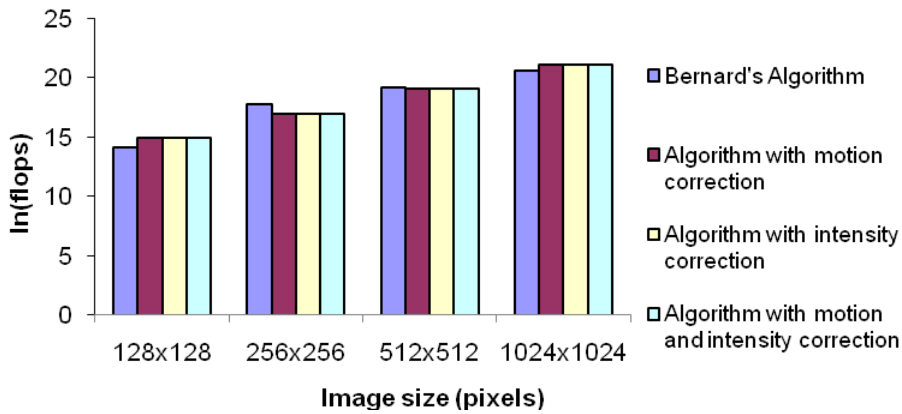

Figure 3.8: Comparison of the developed algorithm complexity

3.4 Computed Tomography

Tomography helps to determine the internal flow or distribution of a material and gives an access to visualize the internal flow structure of the test object by reconstructing data taken from images projected from different angles. In this research, it was used to illustrate the three dimensional concentration field of an injected jet from BOS displacement vector data.

Data reconstruction approaches are divided into three basic types, namely algebraic reconstruction, back-projection and Fourier- based reconstruction.

1. Algebraic reconstruction is an iterative approach. The iteration starts by initial guess of the internal flow structure and computing the deflection angle (for cases like BOS). The calculated deflection angle is compared with the measured angular deflection and the internal flow approximation will be corrected accordingly. This procedure is repeated until the deference between calculated and measured deflection is below the assigned threshold value. This technique is useful for tomographic efforts when certain projections are missing.

2. Back-projection: The deflection vectors are back projected onto a grid and added within the space covered by projections. Filtered back-projection alleviates this problem. Filtered back projections are accomplished by convoluting the projection with filtering functions. The correct choice of filter is extremely important for accurate reconstruction. The convolution process follows three main steps [90]:

- Computing the Fourier transform of the measured deflection vector *E(s)*
- Multiplying *E(S)* by weighting function *W* provides *Sq'*
- Calculating the inverse Fourier transform of *Sq'* and summing it over a spatial domain.

Figure 3.9 shows the flow of filtered back-projection process.

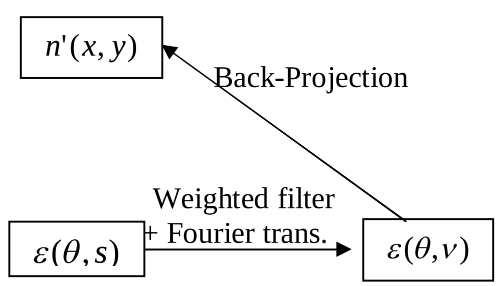

Figure 3.9: Flow of filtered back projection reconstruction

3. Direct Fourier transform applies Fourier slice theorem (FST) to relate the deflection vector $\varepsilon(\theta,s)$ to the 2D Fourier transform of the gradient of index of refraction gradient $\overline{N}(k,l)$. As shown in Figure 3.10, 1-dimensional Fourier transform of the measured deflection vector was used to compute the 2-dimensional Fourier transform of the gradient of index of refraction. Inverse of 2-dimensional Fourier transform of the $\overline{N}(k,l)$ provides the required gradient of index of refraction.

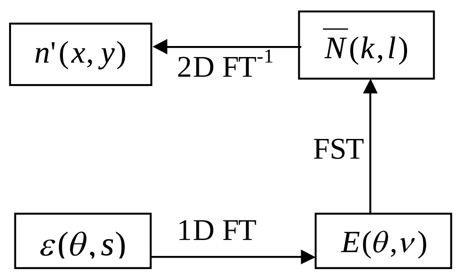

Figure 3.10: Flow of direct Fourier transform algorithm

Image reconstruction principles, from the concentration distribution measurement perspective, are discussed below.

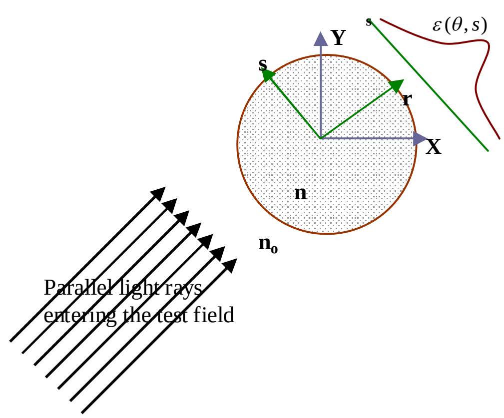

Figure. 3.11: The light rays deflection in plane *r* and *s*

The theory of geometric optics states that an angular deflection of a light beam passing at an angle θ (shown in Figure 3.11) to *X* axis can be described as a function of gradient of index of refraction of the media it passes through. Had there not been a change in index of refaction due to the existence of a different media, all parallel light rays entering the test field would come out undeflected beams. However, the change in refractive medium would redirect the light beams recorded by $\varepsilon(\theta, s)$. This relationship between the light deflection angles and index of refraction can be shown as:

$$\varepsilon(\theta, s) = \int_l grad\, n\{x, y\} dr \tag{3.30}$$

where r and s are the directions of line of sight and deflection projection line respectively.

Equation 3.30 is simplified in the following steps

$\varepsilon(\theta, s) = \int_l {\delta n}/{\delta s}\, dr$, but since $x \sin\theta - y \cos\theta = S$

where S is the distance of line of sight from r. So the above equation can be written as:

$$\varepsilon(\theta, s) = \iint {\delta n}/{\delta s}\, \delta(s - x\sin\theta - y\cos\theta) dxdy \tag{3.31}$$

The $\delta()$ is the Dirac delta (kronecker delta for discrete line of sights) function which is infinite for argument zero and zero for all other arguments and it will be integrated to one. The collection of $\varepsilon(\theta, s)$ at all θ is called radon transform of $grad\, n(x, y)$.

Equation 3.31 in finite projection angles and line of sights can be simplified in the following matrix form

$$\varepsilon(\theta, s) = R\, n' \tag{3.32}$$

where n' is the normalized change in refraction and R is the radon transform matrix.

In order to find out the index of refraction Equation 3.32 needs to be inverted. Reconstruction of the index of refraction from the measured deflection vectors can be made using either iterative or non-iterative methods.

The most commonly used non-iterative reconstruction algorithm in fluid flow diagnostics is the convolution back projection method (CBP). In order to obtain an accurate result the, CBP technique requires a proper selection of weighting filter function and the nyquist sampling criteria (that is all projections are available in all viewing angles) must be attained. The other well-known non-iterative method is a direct matrix inversion method. But this method can only be applied where there is an exact solution. Since most tomography problems are ill posed, the direct matrix inversion ends up providing a less accurate result in many fluid flow visualization techniques [91-93]. The iterative methods, on the other hand, work by initial estimation to the inverse problems and followed by calculating the projection data and comparing it to the measured experimental data. This process is repeated by correcting the initial approximation until the required minimum error criterion is achieved. Iterative techniques usually consume much time and memory.

Reconstruction of the gradient of index of refraction can be made based on inverse Radon transform.

The Fourier transform of gradient of index of refraction ($n'(x,y)$) is:

$$\overline{N}(k,l)=\int_{-\infty}^{\infty}\int_{-\infty}^{\infty} n'(x,y)e^{-2\pi i(kx+ly)}dxdy \tag{3.33}$$

Variables k and l are frequency components. $N(k,l)$ can be determined using Fourier slice theorem. Fourier Slice theorem relates the 2D Fourier transform of gradient of index of refraction ($N(k,l)$) and the 1D Transform of deflection angle $\varepsilon(\theta,s)$ as $E(\theta,\nu)$. The Fourier Slice theorem states that the value of the 2D FT of $n'(x,y)$ along a line at the inclination angle θ is given by the 1D FT of $\varepsilon(\theta,s)$.

Since $E(\theta,\nu)=\overline{N}(k,l)$. with enough projections of $E(\theta,\nu)$, k-l space can be filled to generate $N(k,l)$. As an intermediate step to reconstruct the index of refraction, the Fourier slice theorem is implemented below:

Let's first compute $N(k,l)$ at l=0.

$$N(k,0)=\int_{-\infty}^{\infty}\int_{-\infty}^{\infty}n'(x,y)e^{-2\pi ikx}dxdy \tag{3.34}$$

$$N(k,0)=\int_{-\infty}^{\infty}(\int_{-\infty}^{\infty}n'(x,y)dy)e^{-2\pi ikx}dx \tag{3.35}$$

Applying Fourier slice theorem gives

$$N(k,0)=\int_{-\infty}^{\infty}(\varepsilon(\theta=0,x)e^{-2\pi ikx}dx \tag{3.36}$$

Rotating θ at different angles and computing 1-D Fourier transform provides the whole $\overline{N}(k,l)$ .Once $\overline{N}(k,l)$ is obtained, the required $n'(x,y)$ can be computed using inverse Fourier transform as shown in Equation 3.37.

$$n'(x,y)=\int_{-\infty}^{\infty}\int_{-\infty}^{\infty}\overline{N}(k,l)e^{2\pi i(kx+ly)}dkdl \tag{3.37}$$

The relationship between the gradient index of refraction and the media's refraction index can be related as: $n' = {n-n_o}/{n_0}$ Rearranging this gives:

$$n=n_o(n'+1) \tag{3.38}$$

Equation 3.38 gives the normalized index of refraction of the injected jet in a plane perpendicular to the jet axis. The density distribution in the same plane can be obtained using Gladstone-Dale equation [7]. Three dimensional density fields are obtained by stacking up the above two dimensional density distribution slices.

3.5 Thermodynamic Data Extraction

Merzkirch [94] assumed the resonant frequencies of the gas molecules from the incident light frequency and presented the following relationship between index of refraction and other gas molecule properties.

$$n-1=\frac{\rho L}{2\pi m}\frac{e^2}{m_e}\sum_i\frac{f_i}{(v_i^{\ 2}-v^2)} \tag{3.39}$$

where ρ is the gas density, e and m_e are the charge and mass of an electron, m is the molecular weight, v and v_i are the frequency and resonance frequency of the electrical field created by the light beam, f_i is the oscillator strength which is a number between 0 and 1.

Excluding ρ from the right hand side of Equation 3.30, and replacing by G gives the famous Gladstone -Dale relation (Equation 3.40):

$$n-1=G\rho \tag{3.40}$$

where G is a Gladstone-Dale constant with dimension of $1/\rho$.

This equation can be modified as Equation 3.41 when the understudy gas is a mixture of several species.

$$n-1=\sum_i G_i\rho_i \tag{3.41}$$

where, i is a chemical species. Appendix C shows Gladstone-Dale constants of several gas. The density result which can be found using Equation 3.41 is further exploited to extract additional thermodynamic parameters. These parameters are temperature, concentration and velocity.

3.5.1 Temperature and Concentration Field of a Non-reacting Flow

For non reacting flow, concentration profiles can be treated as single gas and by using an ideal gas equation, the concentration measurement of species mole fraction can be found out using Equation 3.42

$$n-1=\frac{P}{\overline{R}T}\sum_i G(\lambda)_i X_i M_i \tag{3.42}$$

where X_i is the species mole fraction and M_i is species molecular weight.

Similarly, the temperature field of non reacting flow can be computed by combining the Gladstone-Dale equation (Equation 3.37) and ideal gas equation as:

$$T = \frac{\rho_o}{\rho} T_o = \frac{n_o - 1}{n - 1} T_o \tag{3.43}$$

where ρ_o and ρ are ambient density and density of the hot air. Variables n_o and n are ambient index of refraction and hot air index of refraction respectively. T_o is the ambient temperature.

3.5.2 Temperature and Concentration Field of a Reacting Flow

For the case of reacting flow, both the temperature and concentration field measurements of the flow can be obtained by utilizing the ideal gas equation and Gladstone-Dale equation for gas mixtures [30] as

$$n - 1 = \sum_i G(\lambda)_i \rho_i \tag{3.44}$$

where i is the species type generated during flame combustion. The temperature and new species created by the chemical reaction of the fuel and the oxidant can be calculated by using software tools that deal with chemical kinetics, thermodynamics, and transport processes. Under this research, CANTERA software was used. CANTERA is a software tool for solving complex chemical kinetics problems. It solves several reaction combinations to develop a comprehensive understanding of a particular process, which might involve multiple chemical species, concentration ranges, and gas temperatures. The computational capabilities of CANTERA allow for a complex chemical process to be studied in detail, including intermediate compounds and trace compounds [95]. The Gladstone-Dale constant ($G(\lambda_i)$), real gas constant ($\overline{R}$) and species molecular weight (M_i) can be found from thermodynamics data books (sample values are shown in Appendix D). Based on this given information, the index of refraction was calculated using Equation 3.28. The calculated index of refraction values were compared with the index of refraction (n)

which was computed using Equation 3.38. Once the index of refraction values calculated by the two methods match, the respective temperature and concentration values are obtained.

Simultaneous temperature and species concentration measurements can be made for a reacting flow. For fast reacting flames, Bilger [96] noted that some scalars, for example mixture fractions, are uniquely related to major species concentrations in the reacting flow. Based on Bilger’s assumption, Agrawal et. al [41] inferred temperature and species mole from rainbow schlieren measurements of the refractive index difference of pure hydrogen.

3.5.3 Velocity Field Measurement

The velocity field investigated under this study is an axi-symmetric flow. The density value obtained by Equation 3.36 is incorporated into continuity equation as in Equation 3.45.

$$\partial/\partial t \iiint_V \rho dv = -\oiint_s \rho \vec{V}.\overrightarrow{dS} \tag{3.45}$$

where ρ is density, $\vec{V}$ is velocity , $\overrightarrow{dS}$ is cross sectional area of the mass flow rate calculated.

Modifying $\overrightarrow{dS}$ as a product of a cross sectional area dS and its normal vector $\vec{n}$ results in:

$$\partial/\partial t \iiint_V \rho dv = -\oiint_s \rho \vec{V}.\vec{n}ds \tag{3.46}$$

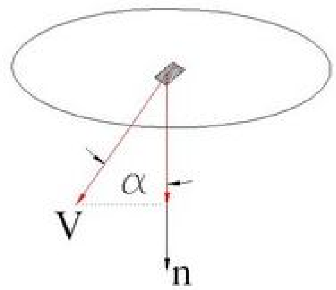

Figure 3.12: The velocity and the normal vector of an elemental area

The velocity $\vec{V}$, which passes through an elemental area as shown in Figure 3.12, has both components $\overrightarrow{V_r}$ and $\overrightarrow{V_z}$. But the continuity equation takes into account only the velocity vector which is perpendicular to the elemental area (or velocity vector along the normal of the area). Only the $\vec{n}$ component of $\vec{V}$ is stated in Equation 3.46 earlier.

In the developed model, the density is given on elemental areas in a plane which is perpendicular to the jet axis (Z axis). Hence our elemental areas has a normal of $\vec{n}$, which is along the z axis.

$$\overrightarrow{V_z} = \vec{V}.\vec{n} = Vn\cos\alpha \tag{3.47}$$

A differential cross sectional area on a plane perpendicular to the jet axis has a normal vector along the jet axis (along $\vec{Z}$ axis). $\overrightarrow{dS}$ can be modified as $\overrightarrow{dS} = \overrightarrow{dz}ds$.

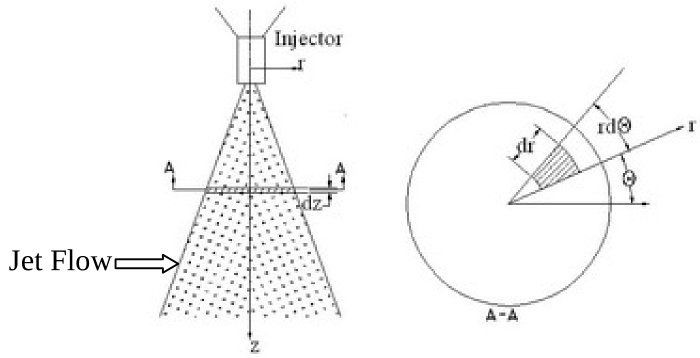

(a) (b)

Figure 3.13(a): Cross sectional view of a Model for (a): Axi-symmetric jet's frontal view (b): Cross sectional area of a jet along a plane perpendicular to the jet axis

As shown in the Figure 3.13, the cross sectional area $ds = r\,dr\,d\theta$ and volume $dv = r\,dr\,d\theta\,dz$ can be used as in Equation 3.47.

$$\partial/\partial t \oiiint_V \rho r dr d\theta dz = -\oiint_s \rho \overrightarrow{V_z} r dr d\theta \quad (3.48)$$

Differentiating Equation 3.48 by $\partial r \partial\theta$ is shown in Equation 3.49.

$$\partial/\partial r\partial\theta \left(\partial/\partial t \oiiint_V \rho r dr d\theta dz \right) = \partial/\partial r\partial\theta \left(-\oiint_s \rho \overrightarrow{V_n} r dr d\theta \right) \quad (3.49)$$

In Figure 3.13 (a), it is also shown that $\overrightarrow{dz}$ is constant. Thus, it can be taken out from the derivative and Equation 3.49 is simplified as Equation 3.50.

$$(\partial/\partial t(\rho r))dz = \rho V_n r \quad (3.50)$$

Rearranging Equation 3.45 gives the axial velocity component.

$$V_z = \frac{(\partial/\partial t(\rho r))dz}{\rho r} \quad (3.51)$$

Since the tangential velocity is zero in axi-symmetric flows, removing the tangential components from a momentum equation for variable density flow on axial direction gives Equation 3.52.

$$\partial(\rho V_z)/\partial t + V_r \, \partial(\rho V_z)/\partial r + V_z \, \partial(\rho V_z)/\partial z = -\partial P/\partial z \tag{3.52}$$

where V_z is calculated in Equation 3.51 and p can be estimated from real gas equation. Thus, the radial velocity can be computed as:

$$V_r = -\left(\frac{\left(\partial p/\partial z\right) + \partial(\rho V_z)/\partial t + V_z \left(\partial(\rho V_z)/\partial z\right)}{\partial(\rho V_z)/\partial r} \right) \tag{3.53}$$

Equations 3.51 and 3.53 give the Eulerian velocity components of the flow in cylindrical coordinate. The numerical derivative computation of Equations 3.51 and 3.53 are solved as follows.

$$\left.\begin{aligned} \frac{\partial(\bullet)}{\partial r} &= (\bullet)_t \otimes f_1 + (\bullet)_{t+1} \otimes f_1 \\ \frac{\partial(\bullet)}{\partial z} &= (\bullet)_t \otimes f_2 + (\bullet)_{t+1} \otimes f_2 \\ \frac{\partial(\bullet)}{\partial t} &= (\bullet)_t \otimes f_3 + (\bullet)_{t+1} \otimes f_3 \end{aligned}\right\} \tag{3.54}$$

where $(\bullet)$ are functions whose derivatives are to be computed: $\rho r, P, \rho V_z$,

$\otimes$ represents convolution

$f_1 = 0.25[-1\ 1 : -1\ 1]$

$f_2 = 0.25[-1\ -1\ ;\ 1\ 1]$

$f_3 = 0.25[1\ 1\ ;\ 1\ 1]$

Once the axial and radial velocity components are obtained, the next task is to study its turbulence statistics. Velocity variance correlation and power spectral density (PSD) of the velocity field are the parameters used to study the turbulence of the velocity.

3.5.4 Turbulence Statistics

The fluctuating velocity component is denoted by

$$V_{\perp i}(\overrightarrow{X},t)=u_{\perp i}(\overrightarrow{X},t)-U_{\perp i}(\overrightarrow{X}) \tag{3.55}$$

where $\perp$ represents either radial or axial component fluctuation, V_i represents the fluctuation component of velocity $u_{\perp i}(\overrightarrow{X},t)$ at position $\overrightarrow{X}$ and time *t*.

The mean velocity $U_{\perp i}(\overrightarrow{X})=\frac{1}{T}\int_{t=0}^{t=T}u_{\perp i}(\overrightarrow{X},t)dt$ (3.55)

The variance of velocity is measured as $\overline{v_{\perp i}v_{\perp i}}=\frac{1}{T}\int_{t=0}^{t=T}v_{\perp i}(\overrightarrow{X}).v_{\perp i}(\overrightarrow{X})dt$ (3.56)

The conventional power spectral density is defined as Fourier transform of two velocity correlation components $v_{\perp i}(\overrightarrow{X})$ separated by a time *t* [97]. The PSD data provides valuable information about the frequency contents of the velocity value and helps to measure the velocity values periodicities.

$$G_{v_{\perp k}v_{\perp k}}(f;\overrightarrow{X})=\frac{1}{T}\int_{t=0}^{t=T}\overline{v_{\perp k}v_{\perp k}}(\tau;\overrightarrow{X})e^{-i\omega\tau}d\tau \tag{3.57}$$

G is power spectral density, *T* is the total time and τ is the frequency of the periodicity.

3.6 Summary

In this chapter, the theoretical background behind BOS's working principle is discussed. Almost all existing literature on BOS assumes that the deflection vector in a certain neighbourhood is pure translation. The rotation term is usually ignored. In this chapter, in order to include both translation and rotation terms, an Affine motion-like model was incorporated. This chapter also presented an improved means of quantitatively estimating the distortion field observed in a (BOS) system specifically to accommodate scenes where the optical medium absorbs or emits light. Wavelet based down-sampling was used in order to obtain a sufficient number of equations to solve the unknowns in the optical flow equations. With the developed algorithm, a time-resolved concentration, temperature and velocity measurements of the flow can be determined. The BOS technique was further extended to compute a velocity field of axi-symmetric jets.

CHAPTER 4

EXPERIMENT SETUP

4.1 Introduction

In this chapter, the experimental apparatuses used and procedures followed are discussed. Different types of flows representing reacting and non reacting gaseous flow conditions were used during the Background Oriented Schlieren experiments. The BOS experimental setup basically can be divided into two as: BOS optical setup and fluid flow setup and fuel injection system. This chapter also discusses the experiments used to validate the BOS data.

4.2 BOS Working Principles

The BOS system is used to measure the index of refraction gradients of a medium, resulting from the light ray refraction and deflection due to localized heating or composition gradients in a gas. BOS employs computer generated high frequency images as background so as to register their movement when there is a change in intermediate flow. This background pattern is placed behind the phase object. Atcheson *et. al* [58] used a wavelet noise as the random dot pattern on one side of a flow while the camera was placed on the opposite side. The wavelet background was generated using procedure discussed in Section 4.3.2. Two types of images were taken, one with the varying density effects and the other without. The displacements of the dots were calculated using correlation algorithms. The light beam deflection principle is portrayed in Figure 4.1.

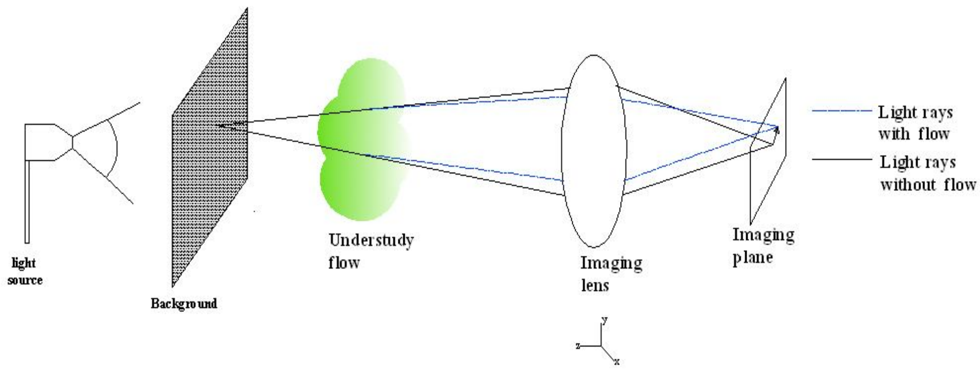

Figure 4.1: Light beam deflection in BOS setup

In order to achieve an accurate measurement, BOS setup need to be optimized and should exhibit good sensitivity and resolution. Klinge [56] pointed out spatial resolution as the most important criterion for a quantitative BOS set-up. He additionally showed that the sensitivity of the BOS setup decreased as the distance between background and the imaging plane increased. In contrast, the spatial resolution increased as the distance between the background and flow field increased.

Goldhahn and Seume [52] demonstrated that the sensitivity increased with larger focal length as well as with the reduction in the distance between the object closer and the camera. Unlike Klinge [56], they showed that the overall length of the set-up played a minor role. Other researchers [51, 68] showed that the system sensitivity increased as the ratio of the distances between the background and flow to background and the camera increased.

4.3 BOS Optical Setup

The optical measurement (BOS) setup consists of a wavelet noise generated background pattern, optical lenses, Xenon white light, Photron Fastcam-x 1280 PCL high speed camera with Nikkor optical lens of 60 mm focal length and Fastcam Control software. The camera's resolution, shutter speed and frame rates are shown in Tables 4.1 and 4.2. A wavelet noise developed by Cook and DeRose [98] was generated and printed on transparency so as to allow light to pass through the background.

4.3.1 Camera Setup

The high speed camera used in the BOS experiments was photron Fastcam-x 1280 PCL camera. Since the spatial resolution and temporal resolutions are inversely related, a need to select an optimum frame rate, resolution and exposure time was required. The two constraints considered to select these camera setup parameters were the flow media behavior and attaining an observable deflection in the background.

The flows considered are open flame, round hot air jet and CNG injected fuel. All these flows exhibited an axi- symmetry (shown in chapter 5). The open flame and round hot jet are continuous flows where as the CNG jet is an intermittent flow with injection duration of 3ms. This behavior allows the open flame and hot air jet to be recorded with relatively slower frame rate. But CNG jet required a higher frame rate so as to record sufficient no of images during injection.

Then again, a higher spatial resolution was required in order to acquire a detectable deformation of the background. A candle plume is used to measure the sensitivity of the camera at different parameters.

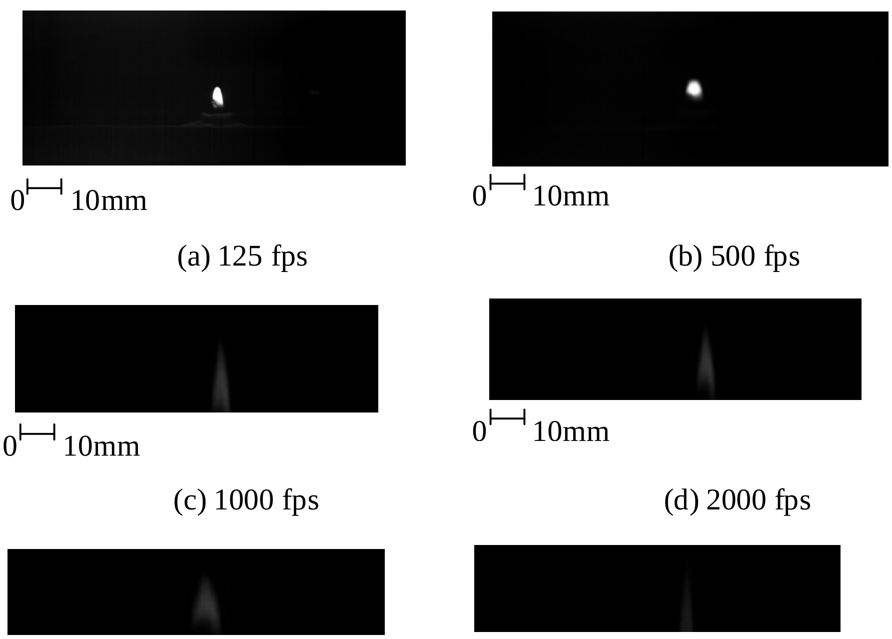

(a) 125 fps (b) 500 fps

0 10mm 0 10mm

(c) 1000 fps (d) 2000 fps

0 10mm 0 10mm

(e) 4000 fps (f) 8000 fps

Figure 4.2: Direct visualization of a candle plume at different frames per second

Figure 4.2 shows an image of a candle plume recorded at different frame rates. As shown in the Figure 4.2, increasing the temporal resolution has reduced the spatial resolutions and at high frame rate the candle plume became almost invisible. The relationship between framing rate against image resolution capabilities of Photron Fastcam-x 1280 PCL camera is shown in Table 4.1.

Table 4.1: Framing rate for different image resolutions [99]

Resolution (pixels)	Framing rate (FPS)								
	60	125	250	500	1000	2000	4000	8000	16000
1280x1024	○	○	○	○	-	-	-	-	-
1280x512	○	○	○	○	○	-	-	-	-
640x512	○	○	○	○	○	-	-	-	-
1280x256	○	○	○	○	○	○	-	-	-
640x256	○	○	○	○	○	○	-	-	-
320x256	○	○	○	○	○	○	-	-	-
640x128	○	○	○	○	○	○	○	-	-
320x128	○	○	○	○	○	○	○	-	-
160x128	○	○	○	○	○	○	○	-	-
640x64	○	○	○	○	○	○	○	○	-
320x64	○	○	○	○	○	○	○	○	-
160x64	○	○	○	○	○	○	○	○	-
80x64	○	○	○	○	○	○	○	○	-
320x32	○	○	○	○	○	○	○	○	○
160x32	○	○	○	○	○	○	○	○	○

Similarly increasing Shutter speed has a reducing effect in image resolution as shown in Figure 4.3. The relationship between framing rate with shutter speed is shown in Table 4.2. The scale used on the horizontal axis is same as the vertical scale. This is because the imaging is conducted by direct visualization and the image pixels are of square shape.

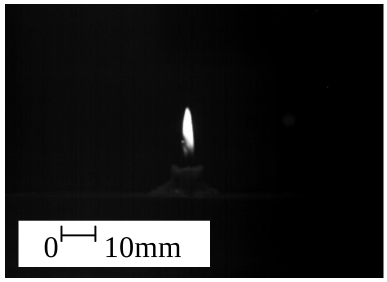

(a) 1/60 sec

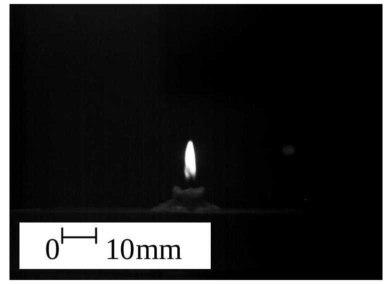

(b) 1/125 sec

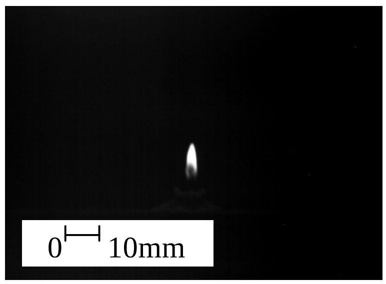

(c) 1/1000 sec

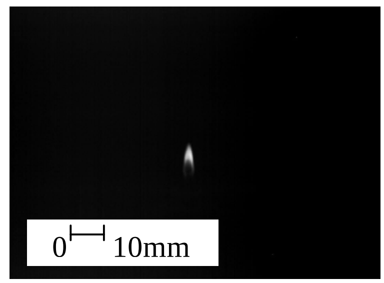

(d) 1/250 sec

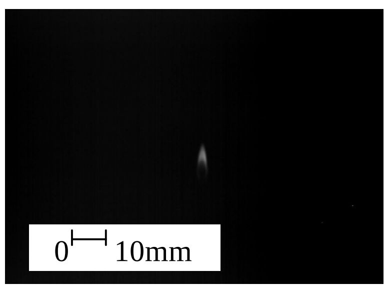

(e) 1/2000 sec

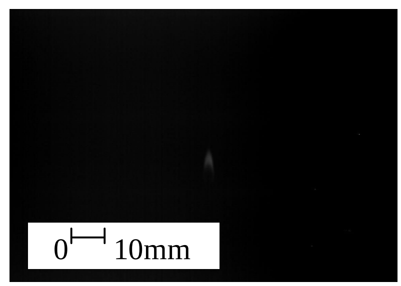

(f) 1/4000 sec

Figure 4.3 direct visualization of a candle plume with different shutter speed at 60 fps

Figure 4.3 designates effects of increasing the shutter speed. It is shown that a larger exposure time provides high resolution images.

Table 4.2: Shutter speed for different framing rates [99]

Shutter speed	Framing rate (FPS)								
	60	125	250	500	1000	2000	4000	8000	16000
1/60s	○	-	-	-	-	-	-	-	-
1/125s	○	○	-	-	-	-	-	-	-
1/250s	○	○	○	-	-	-	-	-	-
1/500s	○	○	○	○	-	-	-	-	-
1/1000s	○	○	○	○	○	-	-	-	-
1/2000s	○	○	○	○	○	○	-	-	-
1/4000s	○	○	○	○	○	○	○	-	-
1/8000s	○	○	○	○	○	○	○	○	-
1/16000s	○	○	○	○	○	○	○	○	○
1/32000s	○	○	○	○	○	○	○	○	○
1/64000s	○	○	○	○	○	○	○	○	○
1/128000s	○	○	○	○	○	○	○	○	○

4.3.2 Background Selection

Several background features had been implemented by researchers. Some of the most commonly used BOS background patterns are: random dot pattern [45,48-52], lined background [77] and wavelet noise background [58, 98]. Figure 4.4 shows these types of background features used in BOS.

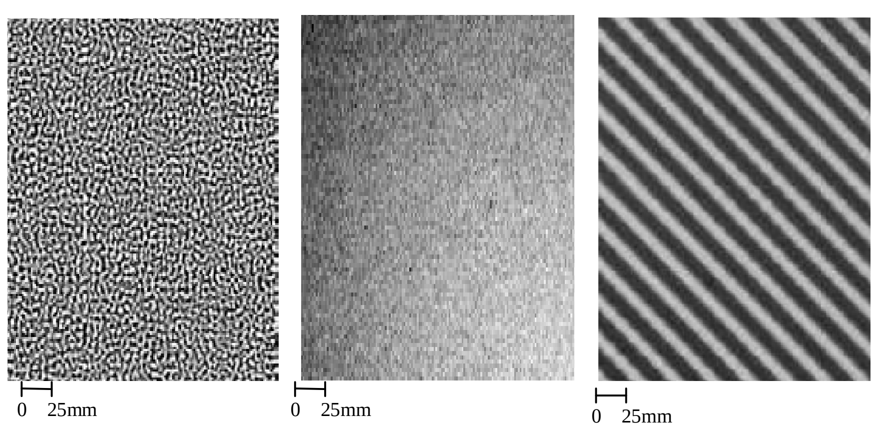

(a) (b) (c)

Figure 4.4: Different backgrounds of BOS (a) wavelet noise (b) random noise (c) lined background

The random dot pattern usually requires to be redeveloped by changing the size of dots and the number of dots density in certain pixel area for every other BOS setup to increase sensitivity and resolution. This requirement is same with lined background. The space between the lines, the thickness and the orientation of the lines has to be frequently redesigned for every new BOS setup and flow condition. Wavelet noise can be used as another background feature option in BOS measurement. Wavelet noise can be developed using the following procedures [98]:

- Create a random noise
- Down-sample the image using wavelet basis function
- Up sample the down sampled image to reconstruct the original image using wavelet basis functions
- Subtract the original image from newly up-sampled image

The remaining (residual) noise is called wavelet noise. Wavelet (multi-scale) background avoids the tedious reprint of the background pattern for the appropriate experimental configuration and helps to safely down-sample the images in order to handle large displacements without the loss of accuracy [58]. This reason made wavelet noise to be used as a background in all BOS experiments conducted under this study.

4.3.3 Overall BOS Set-up

The BOS setup was designed to optimize higher sensitivity and compact setup. Sensitivity can be defined as the minimum deflection (shift) in the background measured at imaging plane for a slight change of media's index of refraction. In Figure 4.5, defection of δy_b in the background is recorded as δy_i in the imaging plane. Had there not been a change in media, the line of sight would look like the path shown using hidden line. But the change in refraction made the point to be recorded δy_i distances away from the undisturbed intermedium flow. It was estimated the light beam is deflected by ε angle.

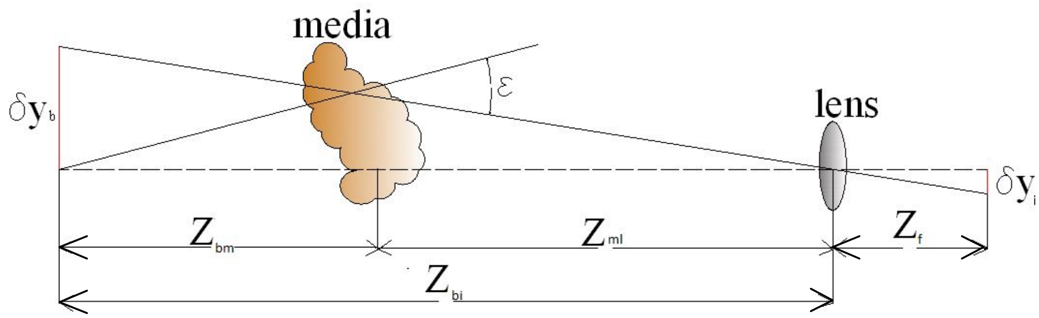

Figure 4.5: Simplified BOS setup

where Z_{bm} is the distance between background and flow media,Z_{ml} is the distance between flow media and lens, Zbi is the distance between background and lens, Z_f is the focal length of the camera, δy_b and δy_i are imaginary deflection vector on the backgroundand the deflection recorded in the camera respectively.

From triangular similarity: $$\delta y_b / Z_{bi} = \delta y_i / Z_f \qquad (4.1)$$

For very small deflection angle ε it can be assumed that

$$\tan \varepsilon \approx \varepsilon = \delta y_b / Z_{bm} \qquad (4.2)$$

Rearranging equations 4.1 and 4.2 provides

$$\delta y_i / Z_f = \delta y_b / Z_{bl} = \varepsilon Z_{bm} / Z_{bl} \qquad (4.3)$$

Equation 4.3 can be rewritten as $$\delta y_i = \varepsilon Z_{bm} Z_f / Z_{bi} \qquad (4.4)$$

Equation 4.4 shows the sensitivity can be enhanced by increasing distance between the background and the media (Z_{bm}) or by increasing the focal length (Z_f) and by decreasing the distance between the background and the camera (Z_{bi}). Thus the sensitivity was optimized by increasing the distance between the media and the background (Z_{bm}). This is because the focal length of the lens available in hand was 60mm and decreasing the distance between the camera and the background (Z_{bi})

decreases the distance between the background and the camera (Z_{bm}) as well. The effects of the relative distances between BOS apparatuses are shown in Figure 4.6. As it is shown in the figure, the system sensitivity decreases when distance Z_{bi} was increased. On the other hand, extending the distance Z_{bm} increases the sensitivity.

Even though, increasing Z_{bm} increases the sensitivity of the system, the camera's field of view and laboratory room space limits Z_{bm}'s length.

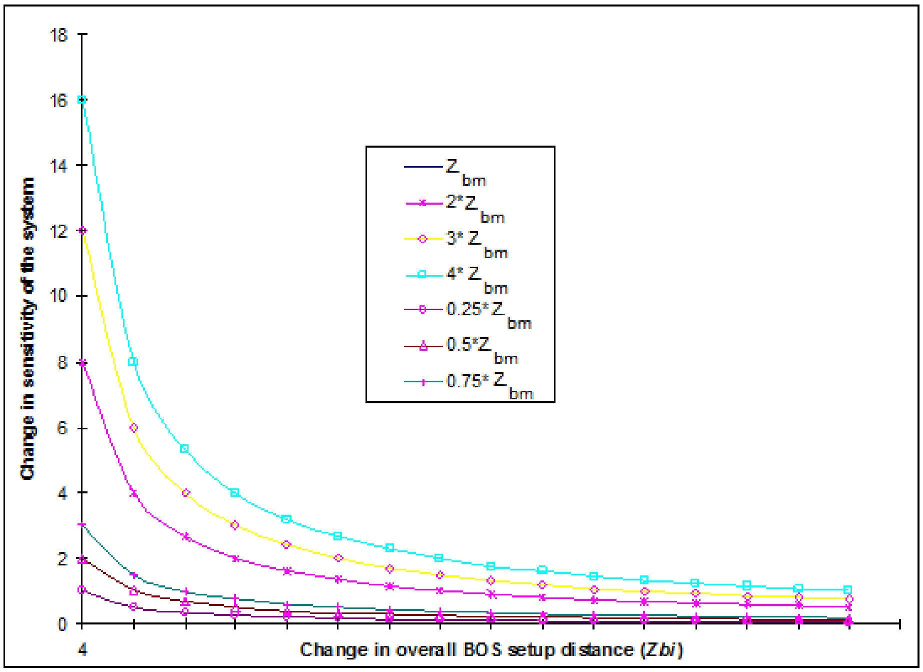

Figure 4.6: Effects of distances between camera, background and flow media in BOS sensitivity

4.3.4 Experimental Error Analysis

The main sources of error could be classified as experimental and data processing errors. The experimental errors could be caused by defects in the optical apparatus, vibrations, flow disturbances, and imperfection of the jet nozzle, whereas, the main sources of error during data processing were computational inaccuracies that could occur during deflection vector estimation, reconstruction algorithms, and velocity field computation.

Researchers [30, 38] proposed the spatial uncertainty of a quantitative Schlieren technique can be assumed as half of its list count sensitivity (δ_{yi}). The uncertainty in the normalized index of refraction is propagated by Equation 4.5.

$$\sigma_{n^l} = n^l \frac{\delta y_i}{2} \tag{4.5}$$

where σ_{n^l} is the uncertainty of the gradient index of refraction *n'*

The uncertainty calculation of the density field measurement based on error propagation can be computed using Equation 4.6 below.

$$\sigma_{\rho^l} = \frac{n^l}{\rho}\sigma_{n^l} = \frac{n'^2}{\rho}\frac{\delta y_i}{2} \tag{4.6}$$

where σ_{ρ} is the uncertainty of the density of the flow.

The temperature measured using BOS is a function of ambient temperature, density of the media and ambient density.

$$T = f(T_o, \rho, \rho_0) \tag{4.7}$$

But, hence, T_o and ρ_o are constant ambient temperature and pressure values the uncertainty of the temperature measured using BOS can be calculated as [52]:

$$\sigma_T = T\frac{\sigma_\rho}{\rho} = T\frac{n'^2}{\rho^2}\frac{\delta y_i}{2} \tag{4.8}$$

where σ_T is the uncertainty of the temperature of the flow.

The axial velocity (V_z) can be expressed as function of flow density (ρ) and the radial distance (*r*) whereas the radial velocity (V_r) is a function of the flow density (ρ) and the radial distance(*r*) and the axial velocity (V_z).

$$\begin{aligned} V_z &= f(\rho, r) \\ V_r &= f(\rho, r, V_z) \end{aligned} \tag{4.9}$$

In order to study the propagation of uncertainty created due to the density measurement error, the radial distance (r) assumed to be constant. Based on Equation 3.46, Equation 3.48 and error propagation property for multiplication and division, the uncertainty of the axial velocity and radial velocity were calculated using Equation 4.10. Figure 4.7 shows the coefficient of error propagation of the concentration, temperature radial and axial velocities. As it shown in Figure 4.7, the radial velocity has the maximum error propagation as the uncertainty of the deflection vector increases. The main reason behind this is the radial velocity is computed based on the already calculated values of density temperature even axial velocity.

$$\begin{aligned} \sigma_{V_z} &= V_z \sqrt{2\left(\frac{\sigma_\rho^2}{\rho}\right)^2} \\ \sigma_{V_r} &= V_{rr} \sqrt{3\left(\frac{\sigma_\rho^2}{\rho}\right)^2} \end{aligned} \tag{4.10}$$

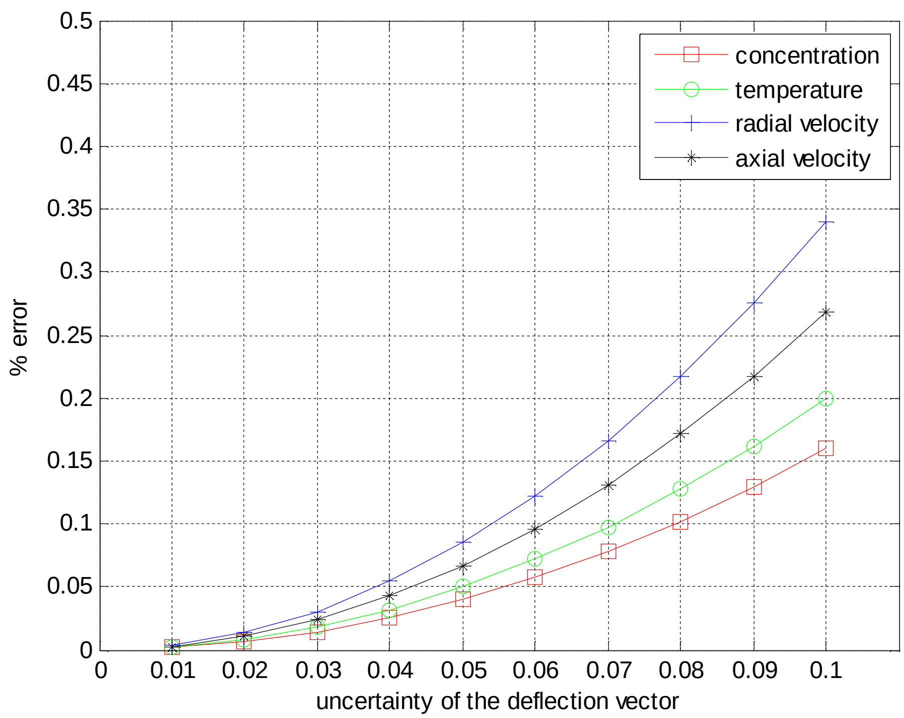

Figure 4.7: Percentage error propagation against uncertainty of the deflection vector

4.3.5 Experimental Verification on the Developed Model

The first experimental task was to verify the importance of modifying the existing optical flow model. The wavelet noise background image was recorded through different flow conditions. These flow conditions included an injected natural gas, natural gas flame and a smoke created by a 2010 FOG Generator. The comparison was made for 200 successive frames and the root mean square error (RMSE) of intensity variation created by the intermediate flows on the background images is shown in Table 4.3. The variation in intensity was found to be insignificant for the injected natural gas but the variation increased for the gas flame and the generated smoke.

Table 4.3: Change in intensity of a background image under different flow conditions.

Flow type	% RMSE
Injected natural gas	1.534
Natural gas flame	10.15
Smoke	9.873

where % RMSE is $|\Delta I_m| = \sqrt{\sum_{i=1}^{i=m}\sum_{j=1}^{j=n}\frac{(I_{(t+1)}(m,n) - I_t(m,n))^2}{m\,X\,n}}\; X100\%$

The change in intensity due to changes in the transfer medium was large for flame and smoke media. But the change in the background intensity was minimal for the injected natural gas case. The reasons behind this effect will be discussed in the next section.

In order to validate the developed algorithm, the wavelet noise background was translated by a known translation vector. For the newly translated background image, the intensity variations caused due to different flow conditions in 8x8 neighborhood pixels were added. The proposed modified flow equation was then used to calculate the translational vectors. Finally, the computed translational vectors were compared with the known translational vectors that were introduced in the beginning. Figure 4.8 shows the validation algorithm. Here, four different optical flow techniques were used, including the proposed one, to compute the deflection vectors.

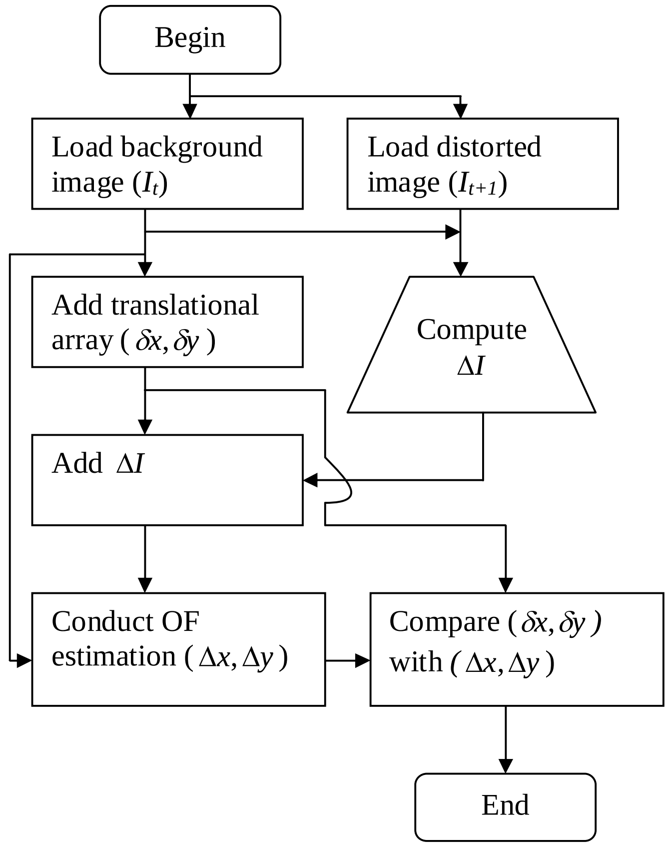

Figure 4.8: Validation algorithm

4.4 Fluid Flow/Injection Set-up

Three types of flows were used under this study: CNG injected fuel, methane flame and hot air. These flows were used to measure temperature, concentration and velocity fields. The temperature and concentration measurement was made for both reacting and non reacting flows. The CNG injected fuel was used to measure concentration of non reacting flow. The methane flame served to measure the concentration and temperature field of a reacting flow based on BOS principles. The hot air measurement was used to measure the temperature field of non reacting flow and the velocity distribution measurement using BOS.

4.4.1 CNG DI Set-up

The Orbital CNG-DI injection system and constant volumetric chamber that has optical window for provision of optical access were the main components of the fuel injection system. Fuel exit pressures are varied from 12 bars to 18 bars. The fuel injection parameters are shown in Table 4.4.

Table 4.4: Fuel injection parameters

Injection Parameters	**Type/Amount**
Fuel	CNG
Injection Pressures	12 bars, 14 bars , 18 bars
Injection Temperature	20^{o} C
Downstream Pressure	0.1007MPA
Downstream Temperature	27.1^{o}C
Injector Nozzle diameter	2 mm

The distance between the background pattern and the centre of the nozzle was 1112.11mm; whereas the distance between the camera lens and the centre of the nozzle was 281.14mm. Having a larger distance between the background pattern and the density field than the distance between the camera and the density field increases the system sensitivity. The resolution of the camera and the shutter time used were 1280x1024 and 1/1000 sec respectively.

4.4.2 Methane Flame Set-up

Simultaneous temperature and fuel species concentration measurements were made for a methane flame. The experimental setup comprises of the LABOGAZ 206 gas flame delivery system in addition to BOS optical setup. Table 4.5 shows the optical distance setup between the flame and BOS apparatuses

Table 4.5: Optical measurements setup

BOS setup distances (mm)	
Focal length	60
Distance between Background and centre of the nozzle	1300
Distance between nozzle centre and camera lens	300

4.4.3 Hot Air Flow Set-up

The hot air setup used, as it is shown in the Figure 4.9, is a centrifugal blower to create a constant mass flow rate of air. The blown air was heated while passing through two heater jackets of 400 and 600 watts. The heated air was then injected to ambient environment with a nozzle diameter of 6mm. The jet exit temperature was measured by thermocouple probes. When the temperature set by the thermostat was read by the probe thermocouples, the thermostat cuts off the power supply of the heaters. The thermostat again connects the power supply, once the thermocouple reading was below the set value.

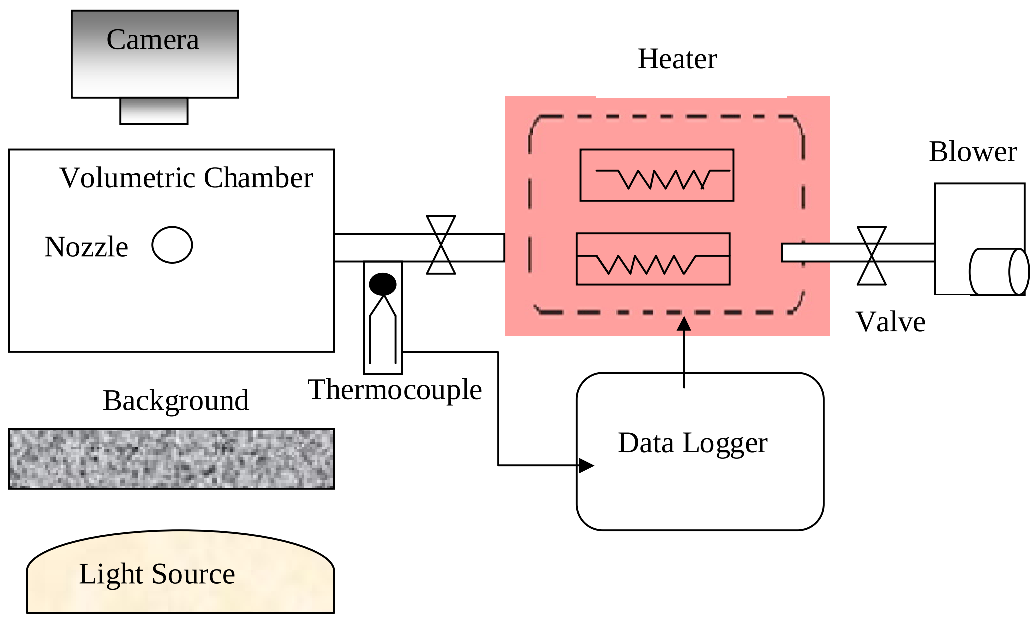

Figure 4.9: BOS experimental setup.

The jet flow exit temperature was maintained at 6 different temperature values for 45 minutes to attain axi-symmetry. The Background Oriented Schlieren imaging was conducted at temperatures of 302 K, 323 K, 373 K, 423 K, 473 K, and 523 K. Based on the background features distortion the temperature and velocity vector fields were estimated.

4.5 The Thermocouple and Hot Wire Anemometer Measurements

The thermocouple probe was used to measure the temperature profiles of the methane flame and hot air jet. The thermocouple measurements were conducted at three different jet exit temperatures: 423 K, 473 K and 523 K. These measurements are taken at Z=3D and Z= 5D. The thermocouple readings were used to validate the temperature field extracted using BOS technique. Since thermocouple probe's thickness was 2mm, based on BOS image calibration, 6x6 pixel temperature information obtained by BOS was averaged and compared with probe measurements.

The methane flame was left burning till it assumed an axi-symmetry and a temperature measurement using a thermocouple probe at 9 Hz acquisition speed were conducted. The mean temperature values of the thermocouple probe are compared with BOS measurements taken in the next chapter.

The accuracy of the velocity vector field measurement was assessed by comparing the computed velocity value with hot wire anemometer measurements. NTC sensor of $\pm 0.5\%$ reading accuracy and $0.1^{o}C$ resolution was used as a hot wire anemometer probe. The description of hotwire anemometry and the thermocouples are shown in Appendix E.

During BOS imaging, calibration was made and one pixel was equal to 0.121 mm and since the probe has a thickness of 0.6mm, 5 pixel's velocity information was ensembled to compare it with the readings recorded by a hot wire anemometer. The hot wire anemometry measurement was conducted at x=0 and y= 0 axis and plane z=3D and z=5D. The jet exit temperature was 302K and 323K.

The time response of thermocouple and hot wire anemometry was 0.15 sec and 0.085 sec respectively. Both thermocouple and hotwire anemometry were mounted on an electronic bed of 3 degrees of freedom. The bed, which was originally developed for LDA experiments, has resolution of 0.02 mm. the procedure followed to mount the probes is discussed in Section 4.6, step 4.

4.6 Experiment Methodology

Experiments need to be designed properly to obtain a maximum benefit from series of experiments in an economical fashion. In order to achieve this goal, experimental procedures was planned and employed as in the following steps.

Step 1: **Aligning BOS and Flow Media Apparatuses**

In order to attain a maximum sensitivity and to use the laboratory space economically, distances Z_{bm} and Z_{bi} are set as shown in Table 4.6. The light source was put as far as possible to assume light rays behave as parallel beam.

Table 4.6: The relative distances between BOS apparatuses and the flow filed

Flow type	*Optical distances*		
	Z_{bm}	Z_{bi}	Distances b/n the background and the light source
CNG jet	281.14 mm	1112.11 mm	1500 mm
Open Methane Flame	300 mm	1300 mm	1500 mm
Hot round jet	300 mm	1300 mm	1500 mm

Step 2: Camera Set-up

Angle of view of a camera describes the angular extent of a given scene that is imaged by a camera. The high speed camera with 60mm lens angle of view was calculated and found as 33^o and 22^o horizontal and vertical angle of views respectively. The frame rate selected was 1000 fps for open flame and round jet. The largest possible spatial resolution at this speed was 1280 x 512 pixels. The lowest possible shutter speed (1/1000 sec) was used to ensure large enough exposure.

Step 3: BOS Experiment

The BOS experiment was conducted by imaging the wavelet noise background with and without the intermediate flow. During the experiment, the ambient temperature and pressure values were 29^oC and 1.007 bar. The recording of the background with and without the intermediate media was made 5 times for one minute duration.

Step 4: Alignment of the Mechanical Probes inside the Flow Media

Hot wire anemometry and thermocouple probes were used to validate the temperature and velocity data measured by BOS. Temperature velocity field measurements at planes 3D and 5D distances along flow central axis were conducted using thermocouples, where D is the diameter of the nozzle (D was equal to 12mm and 6 mm for methane flame and round jet respectively.)

In order to accurately locate the mechanical probe, LED light was put on a movable bed of 0.02 mm resolution (which was made by DANTEC for LDA experiments). When once the position was located, readings were taken. In each 3D and 5D planes at 17 different horizontal positions, the measurement was made. This procedure was repeated 8 times to increase accuracy.

Step 5: Data Reduction

Five data sets of BOS images at either 1000 fps or 4000 fps in one minute duration are too big to handle all data. To ease this burden, systematic data reduction was implemented. The first task was taking the mean image intensity of every 10 frames as this procedure reduces the size of the data by 90%.

Temperature values in methane flame were measured at 30ms interval frames and at every 30 ms interval their neigbourhood frames were convolved with weighting function as shown in Equation 4.11.

$$I_{cm} = [0.1 \;\; 0.2 \;\; 0.4 \;\; 0.2 \;\; 0.1] \otimes [I_{t-2} \;\; I_{t-1} \;\; I_t \;\; I_{t+1} \;\; I_{t+2}]' \qquad (4.11)$$

where I_{cm} *and* I_t are the convolved mean image and image at every 30ms.These convolved images were correlated with mean BOS image of the background without the flow. Additional tasks performed to minimize noise and increase accuracy were :

- Fluorescent lights, fans and air conditioners were switched off to avoid non uniform lighting condition and to attain axi-symmetric flow.
- The background feature, the light source and the camera were placed in strong tripods and image data acquisition was made from other room to minimize vibration and noise.

The above mentioned experimental procedures followed are summarized by the flow chart shown in the Figure 4.10.

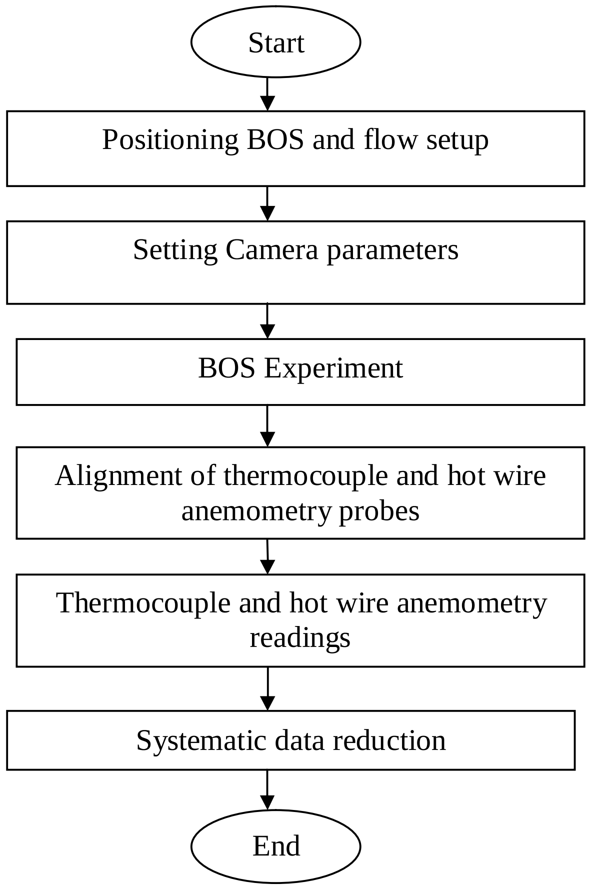

Figure 4.10: Experimental Procedure

4.7 Summary

This chapter discussed the experimental methods planned and carried out for multiple thermodynamic parameters measurement using BOS. The experimental setup was broadly classified as optical setup and fluid flow apparatuses. The optical setup comprised a wavelet noise background, light source, high speed camera and data acquisition control software. The flow setup, on the other hand, was consisted of CNG-DI Injection setup, Labogaz 206 gas flame delivery system and hot air jet apparatus. Thermocouple and hot wire anemometer readings were carried out for calibration and validation purposes of temperature and velocity fields of the flow respectively.

CHAPTER 5

RESULTS AND OBSERVATIONS

5.1 Introduction

This chapter discusses the BOS measurements of temperature, concentration and velocity fields of gaseous flows. The accuracy of the developed intermediate steps of BOS deflection vector estimation algorithms was examined and the sources of errors were conferred. The measured temperature, concentration and velocity fields using BOS are shown. The last section of the chapter compares the temperature and velocity values obtained using BOS with thermocouple and hot wire anemometry readings.

5.2 Deflection Vector Estimation

The deflection vectors obtained by the most commonly used BOS deflection vector computation techniques: Matpiv (region based) [48-52, 58], Horn-Schunck (differential technique) [58, 60], modified Lucas Kanade (differential technique) [58, 61] and our method were compared to the added translation array. Figure 5.1 shows the background displacement vectors of the natural gas flame computed using the four different optical flow procedures. The percentage RMSE of computed displacement vectors by the above techniques from the random translation vectors for injected natural gas, flame and the smoke are shown in Table 5.1.

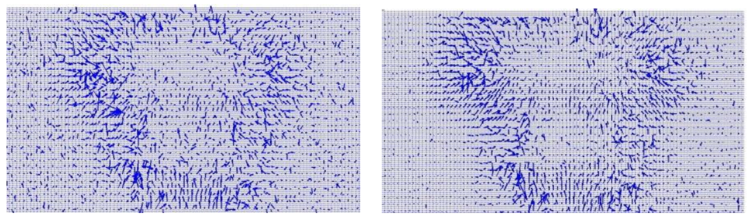

(a) Lucas-Kanade [60] (b) Horn-Schunuk [61]

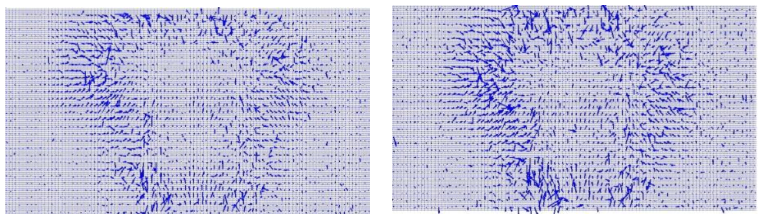

(c) MatPIV [58] (d) Modified OF

Figure 5.1: Background displacement vectors due to the natural gas flame

In Figure 5.2, the modified wavelet based optical flow algorithm was used to extract the background displacement vector for the above mentioned flow conditions.

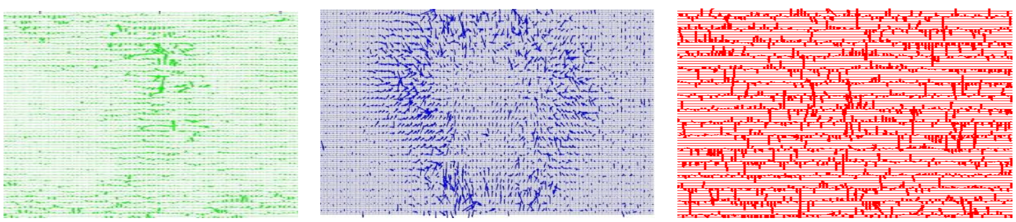

(a) natural gas (b) flame (c) fog

Figure 5.2: The deflection vectors of different flows using the modified algorithm

Table 5.1 shows the comparison of different optical flow algorithms under different transfer media. As shown in Table 5.1, all tested optical flow algorithms work well for the natural gas flow but our method excelled in providing good results for the other transfer channel flow conditions.

The reason that the natural gas jet gave a good optical flow estimation values under all algorithms was that it had no self luminosity and an index of refraction value near to ambient air, as compared with the generated smoke and the natural gas flame. Nevertheless, for the smoke and flame flows, which have higher index of refraction, tend to change the background image intensity significantly when compared to the ambient air. For these flows, the modified optical flow equation gave a superior result.

Table 5.1: Percentage RMS error of optical flow algorithms

Optical flow algorithm	% RMSE		
	Transfer media		
	Injected natural gas	Natural gas Flame	Smoke
MatPIV	1.355	5.635	4.564
Horn-Schunck	1.118	3.332	5.268
Lucas-Kanade	1.117	3.121	3.265
Our method	1.117	1.937	2.015

Once the developed algorithm was accepted that it outperformed the above mentioned methods, the algorithm with and without the motion model was compared with Bernard [89] wavelet based optical flow algorithm. The main reason for this comparison was to find out whether the enhanced motion estimation model or the modified intensity variation terms made the algorithm a better performing one. Table 5.2 shows the relative performance between the three wavelet based optical flow algorithms.

Table 5.2: Comparison of the various variants of the proposed method

Optical flow algorithm	% RMSE		
	Transfer Media		
	Injected natural gas	Natural gas Flame	Smoke
Bernard Algorithm [89]	1.200	2.974	3.729
Modified Intensity variation algorithm only	1.210	2.045	3.664
Algorithm with modified motion model	1.194	3.202	2.392
Algorithm with both Enhanced Motion estimation model + modified Intensity variation	1.117	1.937	2.015

It is shown in Table 5.2 that while using both the motion estimation model and intensity variation terms a minimum % RMSE was obtained for all media. But the affine like motion estimation model had a significant effect on the smoke media. This could be due to the irregular flow nature of the fog. Both Table 5.2 and Figure 5.3 show the intensity correction minimizes percentage RMSE error for the flame data. This is mainly because the luminosity flow behavior of a flame creates a change in intensity. The reason that the conventional optical flow algorithms don't consider the change in intensity constrained their results to be less accurate. Table 5.2 and Figure 5.3 also show that the combined intensity variation and modified motion model algorithms provide superior results in comparison to conventional optical flow algorithms.

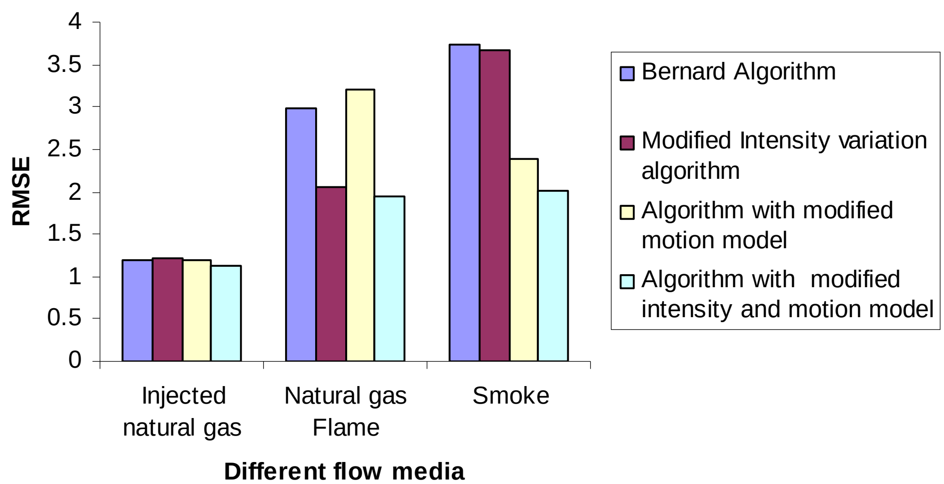

Figure 5.3: Effects of the proposed method parameters

5.3 CNG Concentration Measurement

The experimental setup and the methodology followed to measure the CNG concentration was discussed in chapter four. The validation technique used and the measurement results are discussed in the following sections.

Verifying the experimental repeatability and measuring the accuracy of the optical flow and tomographic algorithms were the two distinct steps used to validate the experimental and image processing procedures in CNG concentration measurement. The structural similarity Index (SSIM) [100] was used to show that the assumed axi-symmetry and acceptable experimental repeatability were achieved. Synthetic data evaluation was used to measure the performance of image processing tasks, which were the optical flow algorithm and optical tomography.

5.3.1 Data Repeatability

Earlier experiments [101] found that oscillations appear at Reynolds number (Re)>160, and a length to diameter ratio of the nozzle (L/D)>7 or (Re-100) x L/D>300. Since the near nozzle air fuel mixture was the important parameter for improved combustion and to avoid self sustained oscillation, this experiment studied the near nozzle flow region at a Reynolds number far lesser than 160.

Non axi-symmetric oscillating flows had a tendency to confer a dissimilar image contrast and luminosity for flow images taken at different spatial and temporal dimensions. The flow was imaged using both conventional schlieren and BOS techniques at a frame speed of 4000 frames per second. The intensity and contrast variation between images at different times and angles by rotating the injector nozzle at every angle of 15o were measured based on SSIM (structural Similarity) index criteria. Wang et al. [100] proposed SSIM as

$$SSIM = \frac{(2\mu_x\mu_y + C1)(2\sigma_{xy} + C2)}{(\mu_x^2 + \mu_y^2 + C1)(\sigma_x^2 + \sigma_y^2 + C2)} \tag{5.1}$$

where μ_x and μ_y are mean intensity images and σ_x and σ_y are standard deviations of images.

$$\sigma_{xy} = \frac{1}{N-1}\sum_{i-1}^{N}(x_i - \mu_x)(y_i - \mu_i) \tag{5.2}$$

x_i and y_i are pixel intensities of image *x* and *y* and C_1 and C_2 are constants added to avoid zero denominators.

Pairs of images were randomly selected from database of BOS and conventional schlieren images. The similarities between random pairs of images were computed using SSIM. The mean value of SSIM for images recorded at the same projection angle with different time was found to be 0.9794 and 0.9664 for BOS and conventional Schlieren images respectively (where unity was a value for identical images). The computed mean SSIM value for pair of images at different angles were found to be 0.9630 and 0.9612 for BOS and conventional Schlieren images respectively. This result gave a provision to assume the flow under study was a steady non-oscillating flow. The SSIM value also confirmed the noise that might occur due to vibration of the camera, background and fuel injector, was at an acceptable level.

5.3.2 Accuracy of the Algorithms

The accuracy of the BOS set up, which was prepared to CNG concentration measurement, was measured using synthetic data evaluation. A known volumetric (density) field of injected fuel data was taken [102] and used as a variation of index of refraction test field in a virtual BOS optical setup. The virtual BOS setup was arranged using a ray casting method. Rays started from virtual camera position, were passed through gasoline vapour volumetric information and struck the observation area. This area was represented by wavelet noise virtual background. The relative distance from the background and the volumetric data to the virtual imaging plane was 5:2. The accuracy potential was defined by a standard deviation of 0.1 pixels in the plane. A similar imaginary setup excluding the volumetric data was used to capture the background image in order to simulate the background image without flow. These pairs of images with and without the known volumetric density field were used as inputs to the optical flow and tomography algorithms in order to calculate the index of refraction (density of the field). The density distribution obtained by the virtual BOS experiment was compared with the given density field and a percentage RMSE error of 1.17 was found. This RMSE value was seen as evidence of the high level of accuracy of the BOS setup.

5.3.3 BOS Results

The BOS results shown below were computed at CNG jet's maximum tip penetration which was at 3ms after the start of injection. The angular deflection vectors, for different cross sectional planes, along the radial axis are plotted as shown in Figure 5.4. Power spectral density estimation was used to find the cut-off frequency for filtering the angular deflection data. Based on the results from power spectral density estimation, a normalized frequency of 0.47 was selected to be a cut-off frequency and higher values than that were considered as noise and removed. A mean of 12 readings at maximum tip penetration was taken.

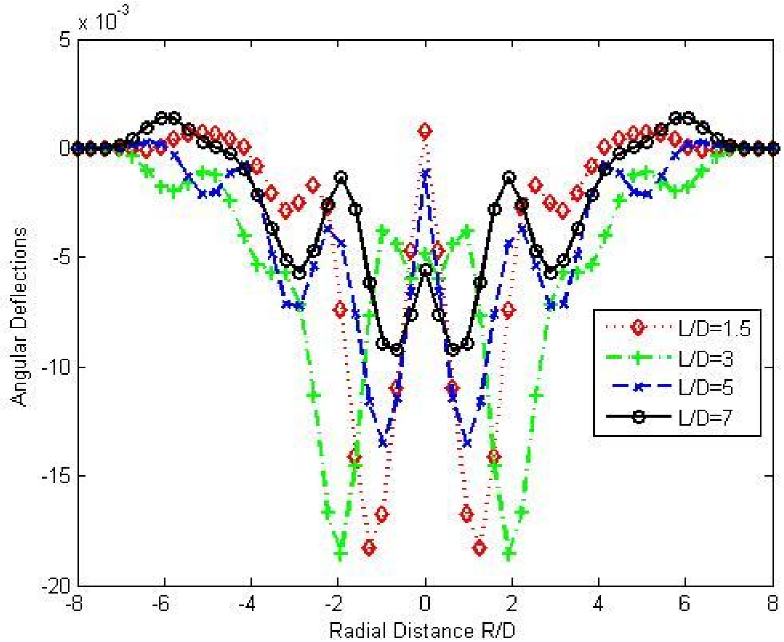

Figure 5.4: Angular deflection vectors along radial axis at maximum tip penetration and 12 bar injection pressure of the CNG jet

The normalized index of refraction was obtained using filtered back projection. Figure 5.5 shows the change in index of refraction of the test field from the ambient index of refraction at different planes perpendicular to the nozzle axis. To add visibility, the change in index of refraction was multiplied by 1000.

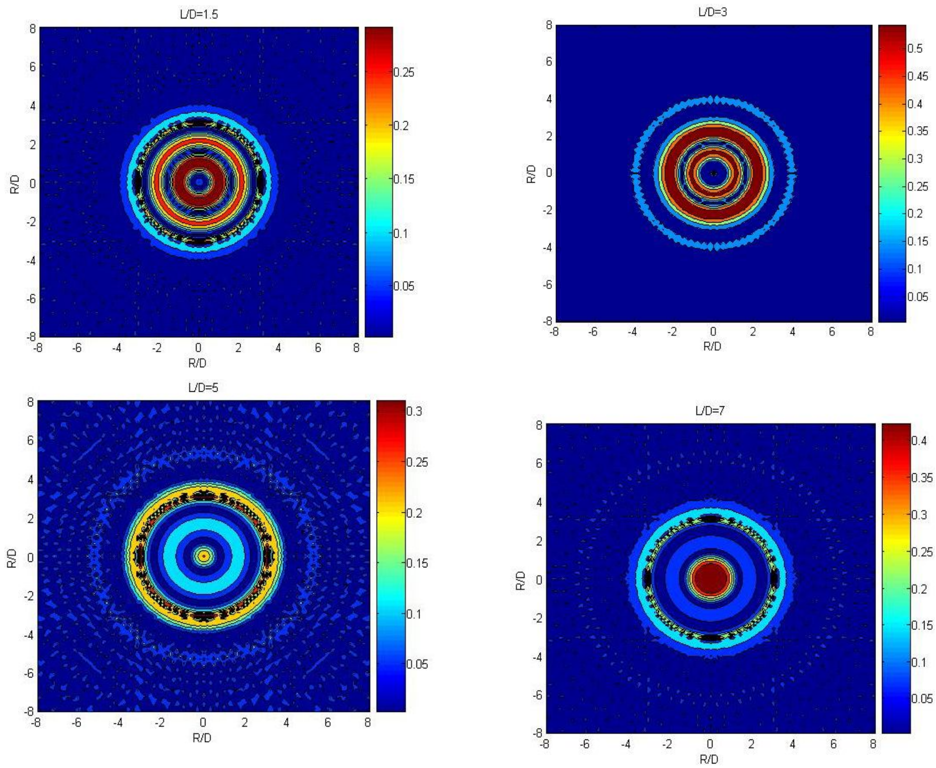

Figure 5.5: Change in index of refraction at different planes perpendicular to the jet axis at maximum tip penetration and 12 bar injection pressure

Figure 5.6 portrays the concentration of the CNG fuel in the near nozzle region. The figure also displays the fuel expansion area at different transverse planes. The fuel concentration was presented in terms of mole percentage.

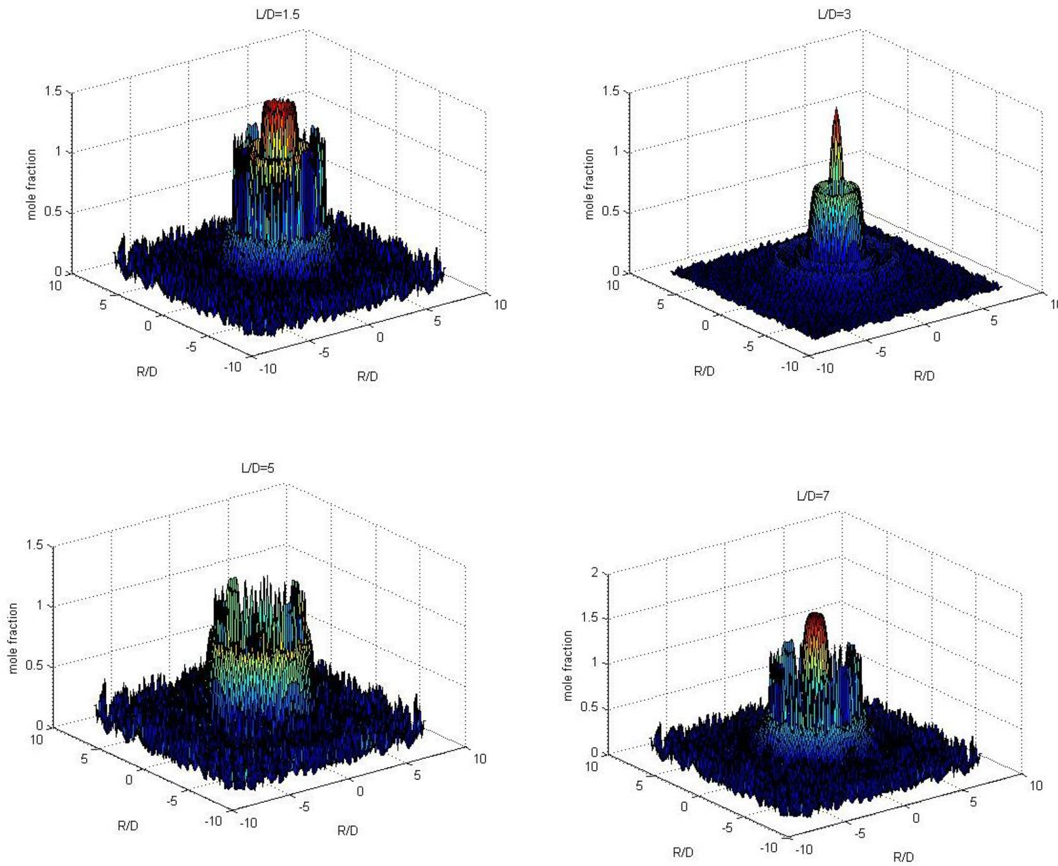

Figure 5.6: CNG concentrations at different planes perpendicular to the jet axis at maximum tip penetration and 12 bar injection pressure

In order to study the behavior of the fuel concentration along jet central axis, density distribution along the jet core axis was computed and plotted in Figure 5.8. The density distribution along centerline decays after having patterns of alternating low and high density regions. The sinusoidal curve like density distribution is believed to subsist because of the under expanded jet behavior. Figure 5.8 shows different injection pressures' normalized density fields of CNG jet along injector nozzle axis at the maximum injection time. The maximum injection time was 3 ms from start of injection.

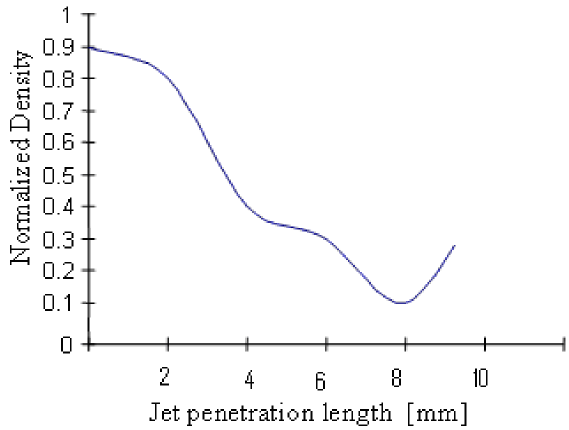

(a) 12 bars

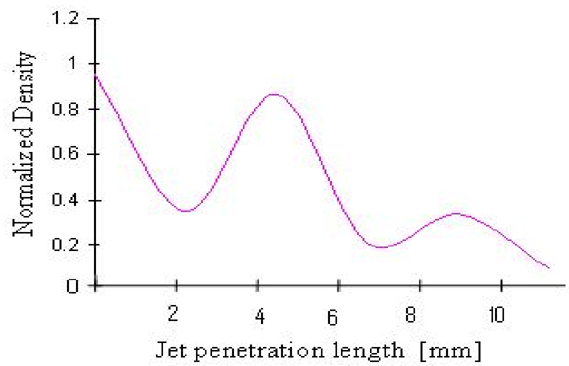

(b) 14 bars

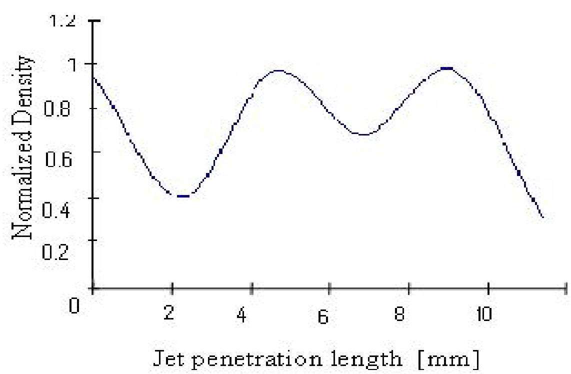

18 bars

Figure 5.7: Normalized density distribution near nozzle along the jet axis at 3 ms after start of injection

Figures 5.8 and 5.9 are depicted in order to look at the density distribution in a plane parallel to the jet axis. Figures 5.8 and 5.9 illustrate the fuel concentration of a CNG jet with 0.25 ms interval at 14 and 12 bars injection pressures.

It can be seen from the figures that as we go away from the end tip of the nozzle, an overall fuel density concentration in the near nozzle region gets higher at the outer conical jet surface than the inner core region.

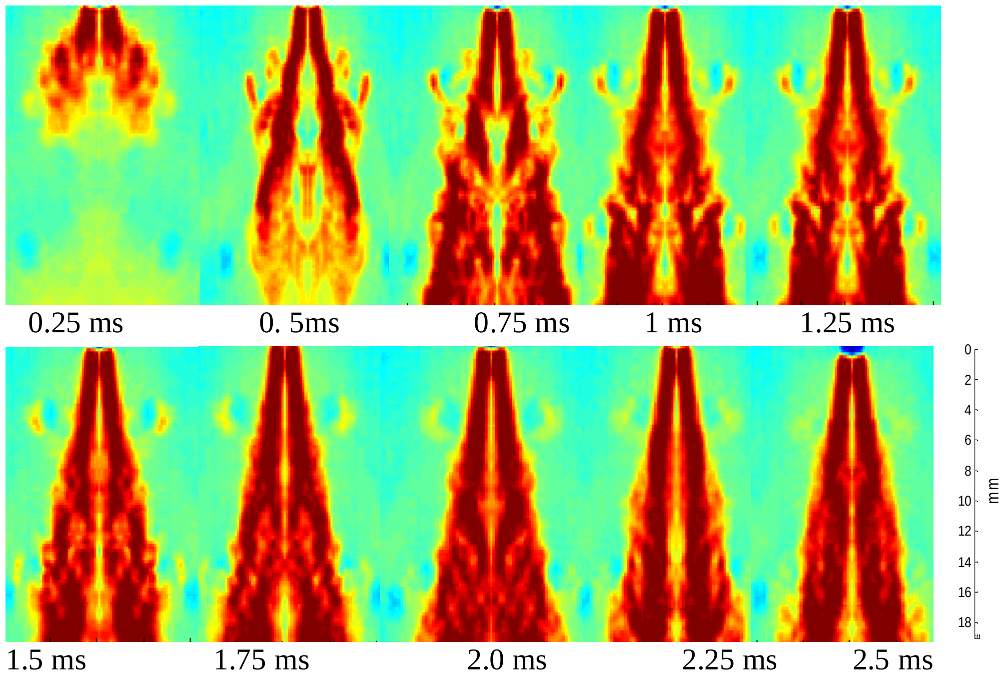

Figure 5.8: CNG concentrations in a plane parallel to the jet axis at 14 bar injection pressure

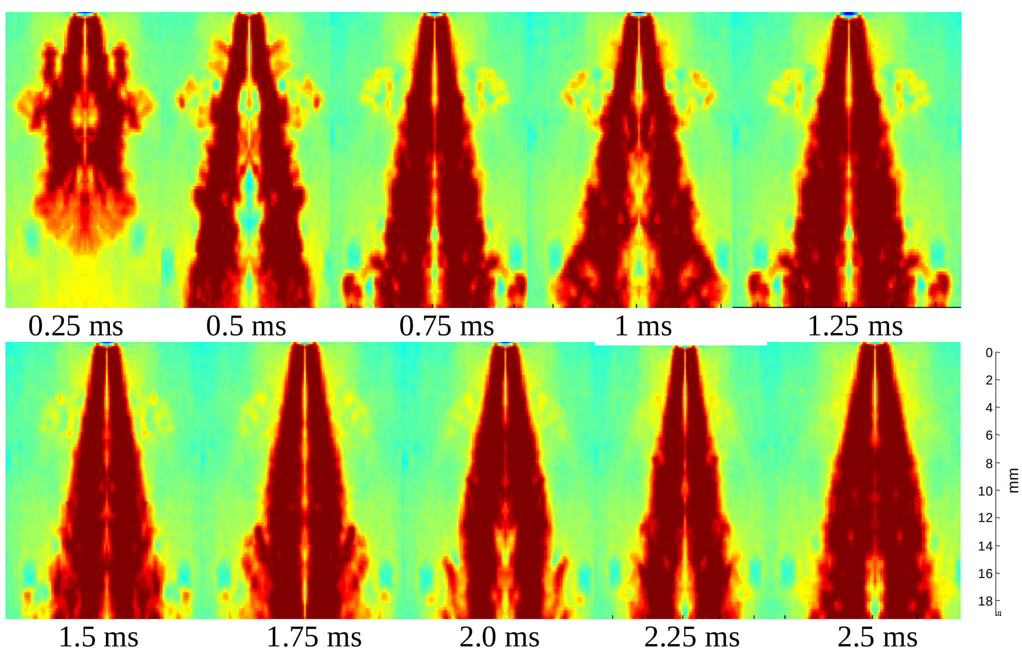

Figure 5.9: CNG concentrations in a plane parallel to the jet axis at 14 bar injection pressure

5.4 Methane Flame Temperature and Concentration Measurement

Open flame imaging was conducted using three techniques namely: direct visualization, Schlieren imaging and BOS. An image taken by direct imaging (Figure 5.10) and conventional Schlieren (Figure 5.11) helped to study the macro-spray parameter namely: axi-symmetry of the flow. The axi-symmetry of the methane flow was studied using SSIM criteria. The flame image recorded using conventional schlieren showed a structural simmilarty index of 0.934 while imaged from different views (Table 5.3). This result shows the flow is near axi-symmetric as SSIM unit of 1 is a value for perfectly identical images.

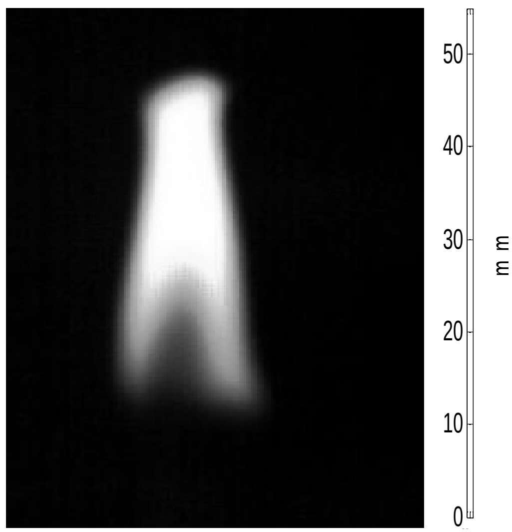

Figure 5.10: Direct Flame Visualization

Once again, SSIM criterion, described in Section 5.3.1, was used to check if the axi-symmetric assumption can be introduced. As it is shown in Table 5.3 the BOS and conventional Schlieren images recorded after the fuel was ignited gave a good similarity as compared with the Schlieren and BOS images of methane gas flow before ignition.

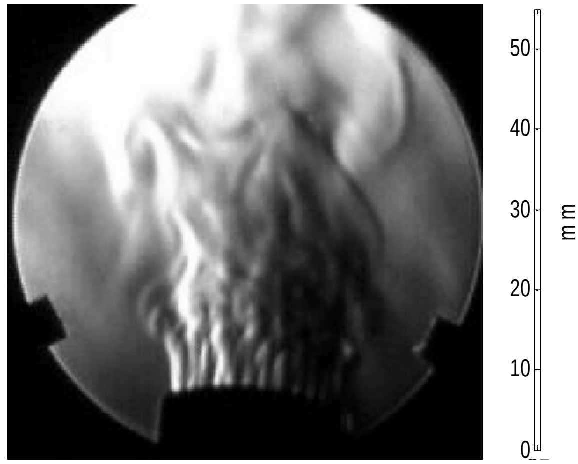

(a)

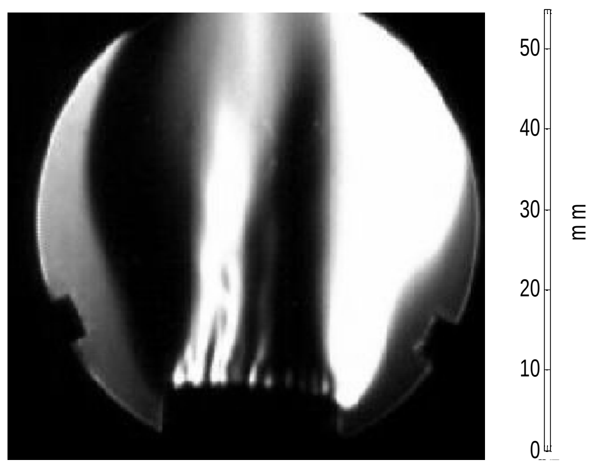

(b)

Figure 5.11: (a) The gas flow Schlieren image before ignition (b) the flame Schlieren image after ignition

In order to measure the concentrations of chemical species created and temperature of the flame, BOS technique was used to estimate the deflection vector of the wavelet background. Figure 5.12 shows the background image taken through the gas flame. Figure 5.12 shows (a) the raw image of the background when there is no flame media between the background and the camera. Figure 5.12(b) shows the raw image of the background recorded through the flame media. No significant change of the background feature is visible to human eye. But implementation of the developed optical flow algorithm helped to detect the translation of the background feature as shown in Figure 5.13.

Table 5.3: Structural Similarity Index Measurement (SSIM) criteria for flame images

Recorded Images	SSIM	
	At different times	At different angles
Direct visualization	0.890	0.815
Schlieren image of the fuel before ignition	0.852	0.823
Schlieren image of the flame	0.921	0.934
BOS Image of the fuel before ignition	0.897	0.854
BOS image of the flame	0.946	0.935

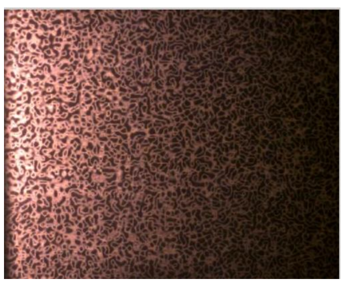

(a)

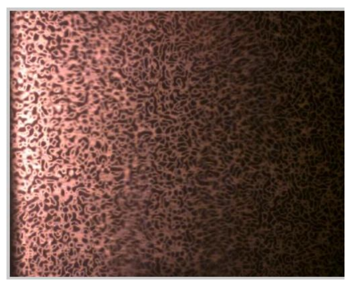

(b)

Figure 5.12: The BOS images (a) without flame and (b) through gas flame media

The background image taken with and without the flame media in between the camera and background were used as image frames to measure the background features displacement. The computed displacement vector field is shown in Figure 5.13.

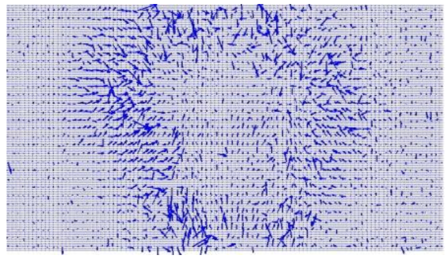

Figure 5.13: Displacement vector field of methane flame

For fast reacting flames, Bilger [96] noted that some scalars, for example mixture fractions, were uniquely related to major species concentrations in the flame. Based on Bilger's assumption, Agrawal et. al [41] inferred the temperature and species mole fraction from rainbow Schlieren measurements of the refractive index difference of pure hydrogen.

Equation 3.38 and ideal gas equations were solved for a given mixture fraction to determine the equilibrium temperature and species concentrations the fuel species and temperature was generated using CANTERA. The calculation showed 50 different species created due to chemical reaction between the fuel and air. The chemical species produced during methane burning are shown in Appendix F.

Species with maximum mole fractions less than 10-5 were removed to adapt a procedure proposed by [41]. This assumption effectively reduced the number of species under consideration to 11. These species with their maximum and minimum mole fractions are shown in Table 5.4. Out of the 11 species mentioned in Table 5.5, the CO2 species mole fractions were selected for study. A table that relates the varying specific mole fractions, temperature and the change in index of refraction with 8 digit precision was constructed based on Equation 3.26. The respective refractive index differences were used to locate the species distribution in the flame.

Table 5.4: Chemical Species with their respective mole fractions

Chemical Species	Maximum Mole fraction (x 10^{-03})	Minimum Mole fraction (x 10^{-10})
H_2	447	0.903
H	69.80	0.001
O_2	142.53	1.21665 x 10^{-13}
OH	3.02	0.001
H_2O	195	4.22 x 10^{8}
CO	207	0.407
CO_2	86.10	0.305 x 10^{9}
NH3	0.12	2.91 x 10^{-9}
NO	3.16	1.36 x 10^{-6}
NO_2	0.31	6.31 x 10^{-19}
N_2	765.75	0.577507 x10^{10}

Figure 5.14 (a)-(c) shows the species distribution of CO_2 concentration in a plane along the axi-symmetric axis of the flame. The measured CO_2 concentration varied from 0.0861 to 0.0305 mole fractions. It is also observed that the majority of CO_2 species was found at the peripheral regions of the flame.

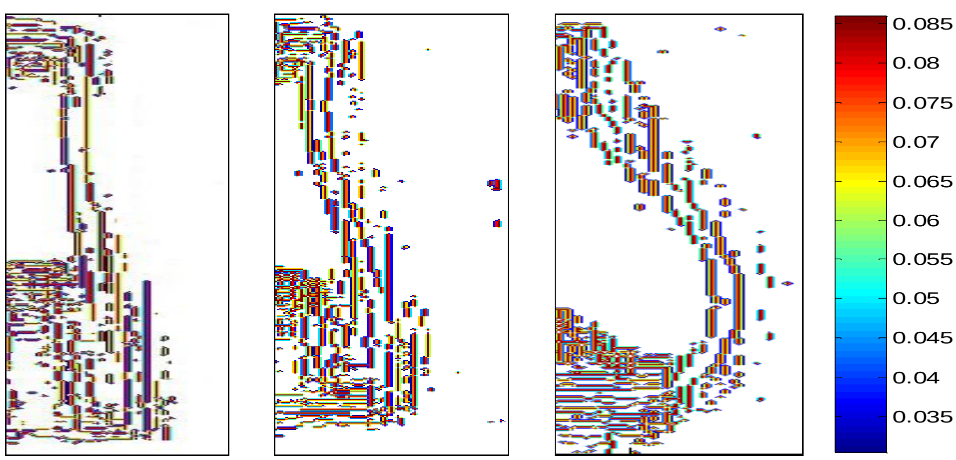

(a) (b) (c)

Fig. 5.14: (a) - (c): Mole fraction of CO_2 in 30ms intervalof the half section in a plane along the axi-symmetric axis.

The temperature field measured at the same time during the above shown CO_2 species concentration is shown in the Figure 5.15. The measured temperature values range from 950 K to 1150 K. The temperature values are plotted as temperature profile regions in steps of 50 K. As shown in the Figure 5.15, the inner core of the flame region has exhibited the highest temperature value.

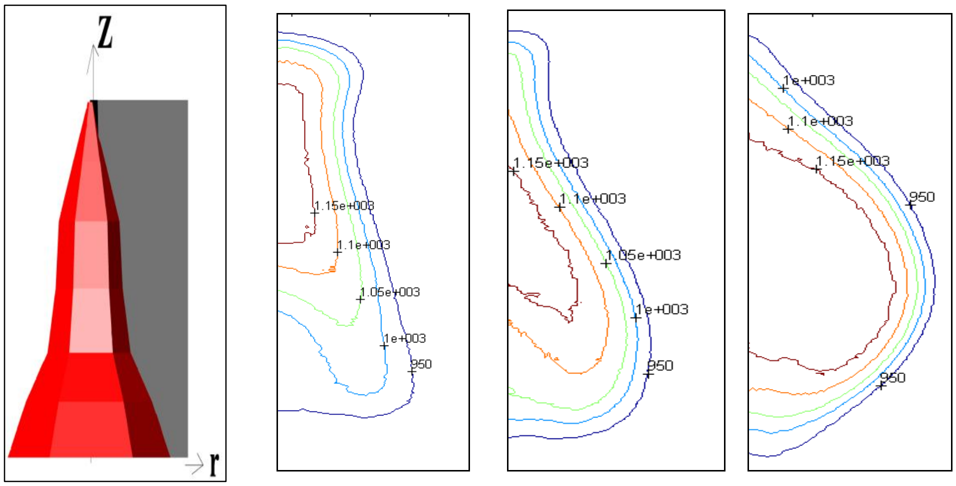

(a) (b) (c) (d)

Figure 5.15: (a) View-plane showing temperature distribution (b) - (d): Temperature distribution contour plot in steps of 50 K in every 30 ms interval

The computed BOS mean flame temperature values were compared to average thermocouple measurements in a radial plane at 3D and 5D from the nozzle at different points and showed good agreement as shown in Figure 5.16.

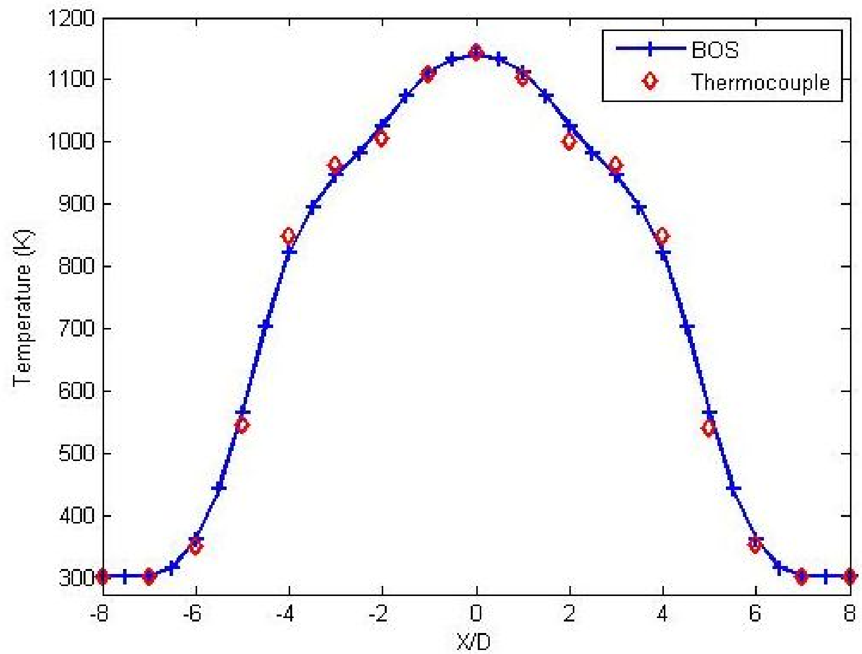

(a)

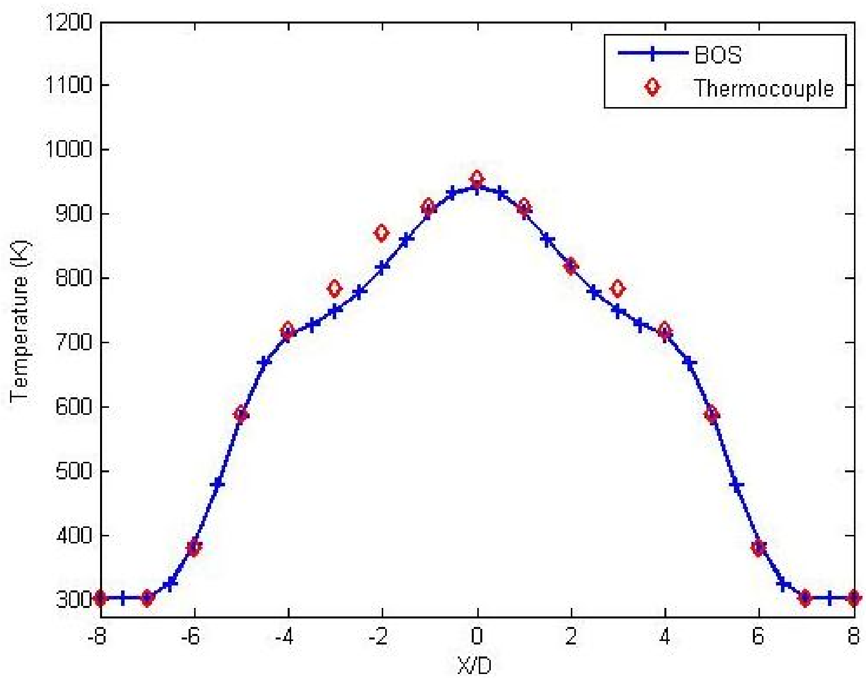

(b)

Figure 5.16: Mean temperature values at (a) Z=3D (b) Z=5D

The instantaneous BOS and thermocouple measurements were averaged in order to get mean temperature values.

Figure 5.17 shows the standard deviation between BOS and thermocouple readings at 3D and 5D distances along the axi-symmetric axis. The results deviation increased as the distance of the measuring plane from nozzle tip increased. The maximum deviation of 4.87 K were obtained at distances 3<= |x|< = 4D to 5D. Higher variation appeared was because these points are in the transition state regions with high fluctuations in thermodynamic parameters.

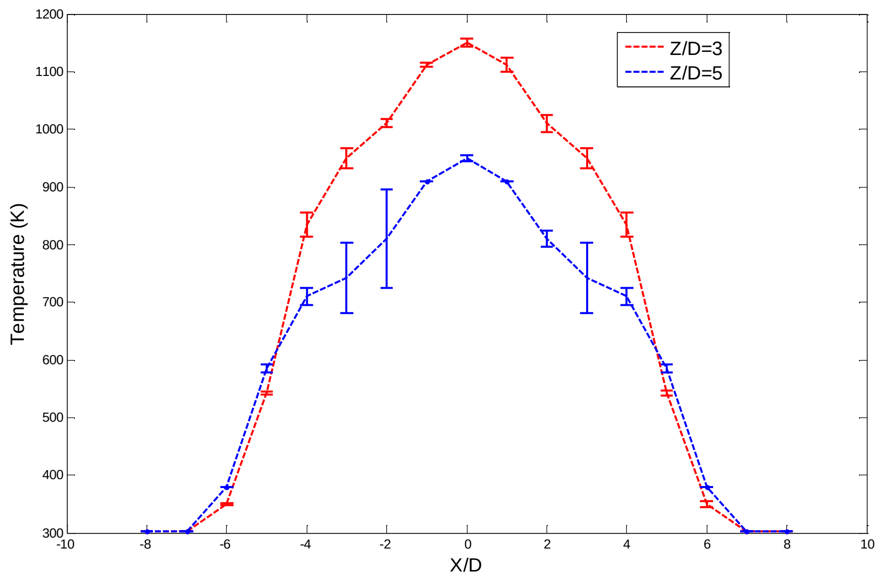

Figure 5.17: Mean temperature and Standard deviation between BOS and thermocouple readings at 3D and 5D planes perpendicular to the flame axis

5.5 Hot Round Jet Velocity Vector and Temperature Fields Measurement

The density distribution of the injected air was calculated using Equation 3.6 to Equation 3.41. The centreline density distribution of the jet as a function of the axial distance to diameter of the nozzle ratio (Z/D) is shown in Figure 5.18. The center-line density fluctuated but exhibited a decreasing trend with axial distance.

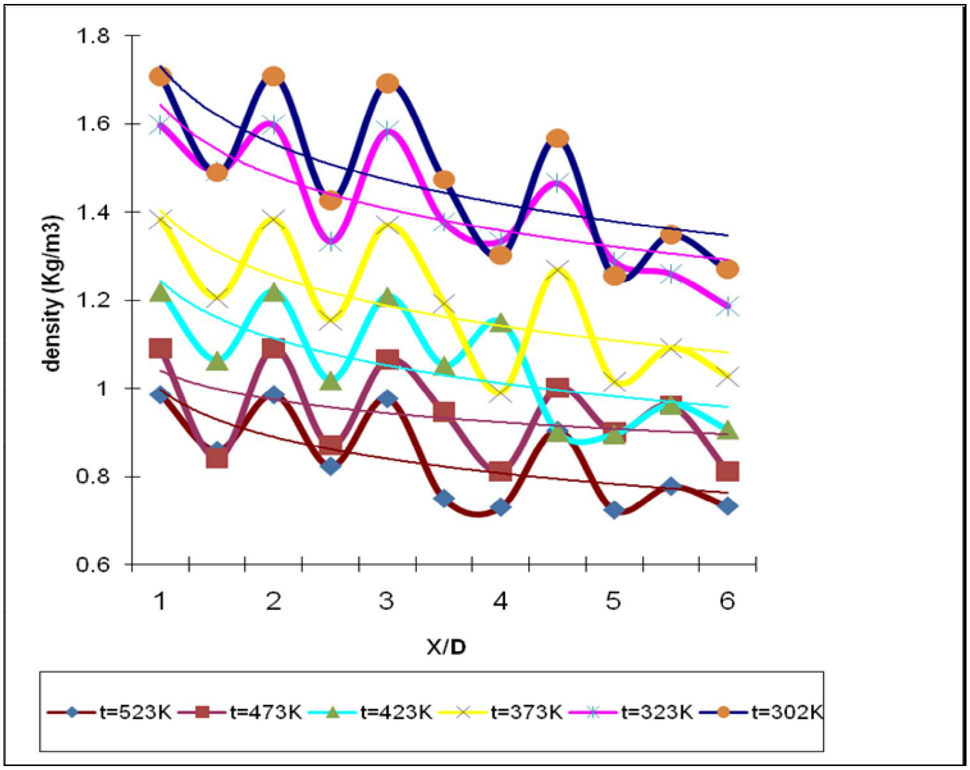

Figure 5.18: Centerline density distribution of different exit temperatures and their respective trend lines.

The alternating high and low density profiles along the jet axis were caused due to the compression and rarefaction created due to the difference of jet exit and ambient pressures. This compression rarefaction phenomenon was also reported by other researches [52, 103] and a similar density fluctuation behavior of underexpanded jet was observed.

The center-line velocity decay for six different jet-exit-temperatures was calculated. The center-line velocity decay for 302 K and 323 K temperature were compared with the hot wire anemometry and shown in Figure 5.19. The figure also showed the center line velocity to jet exit velocity ratio (U/Uo) decay was faster at higher temperatures.

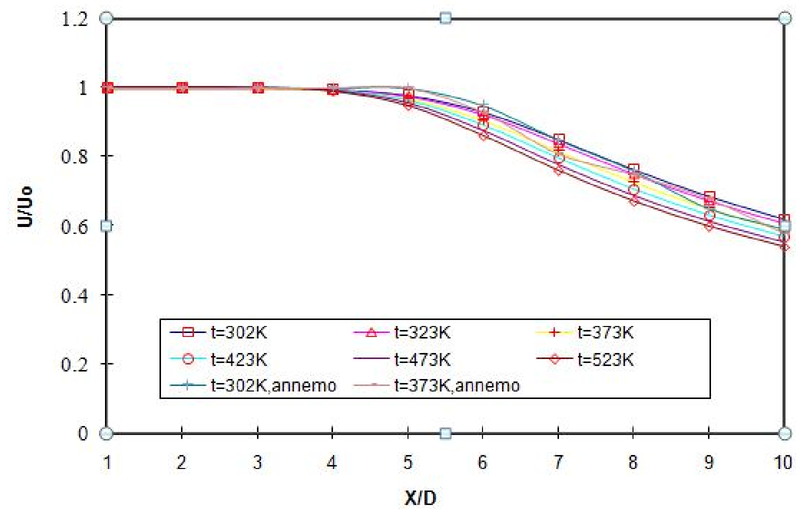

Figure 5.19: Center-line velocity decay at different jet exit temperatures.

The axial velocity distribution normalized by center-line velocity of the jet at 473K is shown in Figure 5.20. As conferred by many researchers, a Gaussian like velocity distribution was achieved.

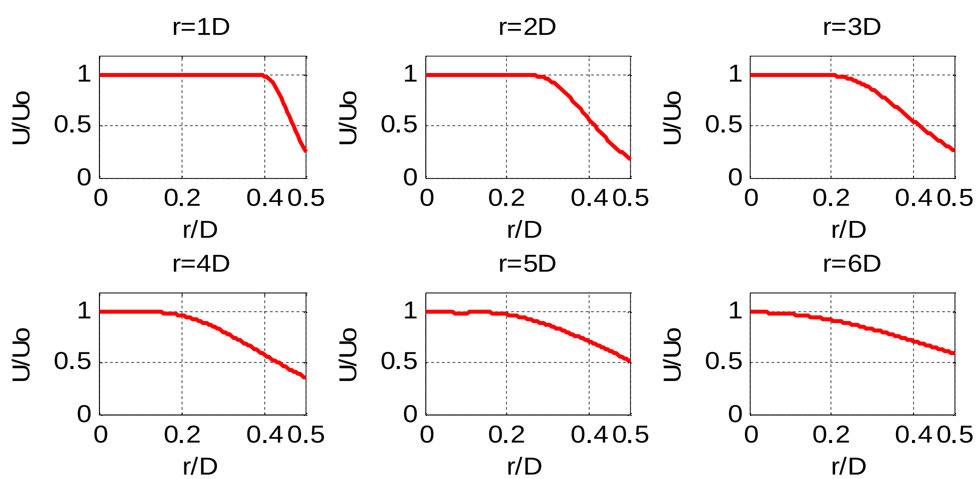

Figure 5.20: The axial velocity distribution of the jet at 473 K

Figure 5.21 and Figure 5.22 shows the averaged radial and axial velocity profiles of a hot jet at an exit temperature of 473 K. As it shown in the Figure 5.21, the velocity core region decreased as the axial distance increases. Velocity core radius of 0.47D was observed at 1D axial distance and it kept on decreasing and the velocity core radius was 0.21D at 5D. The color plate shown at the right side of Figures 5.21 and 5.22shows the magnitude of normalized velocity values.

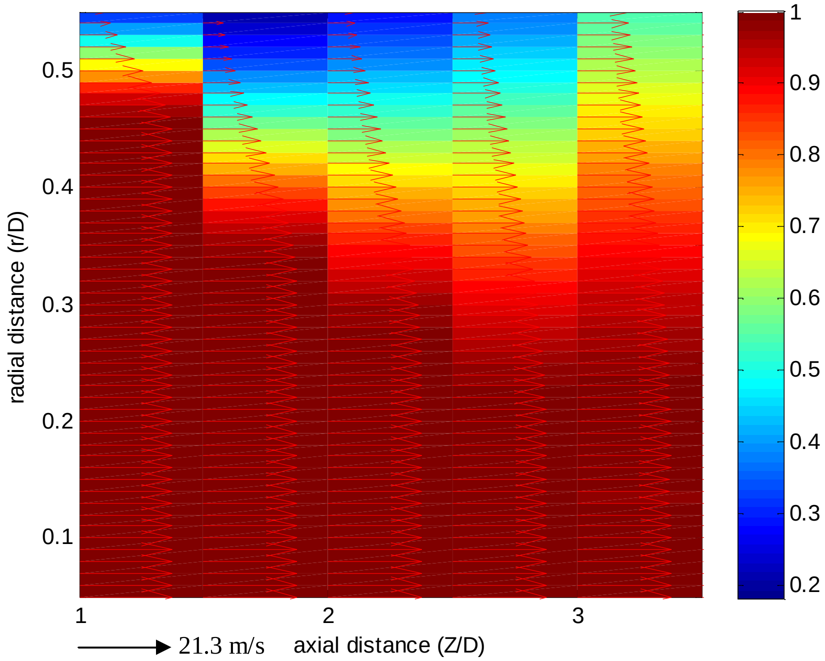

Figure 5.21: Axial velocity of a heated jet at 473 K

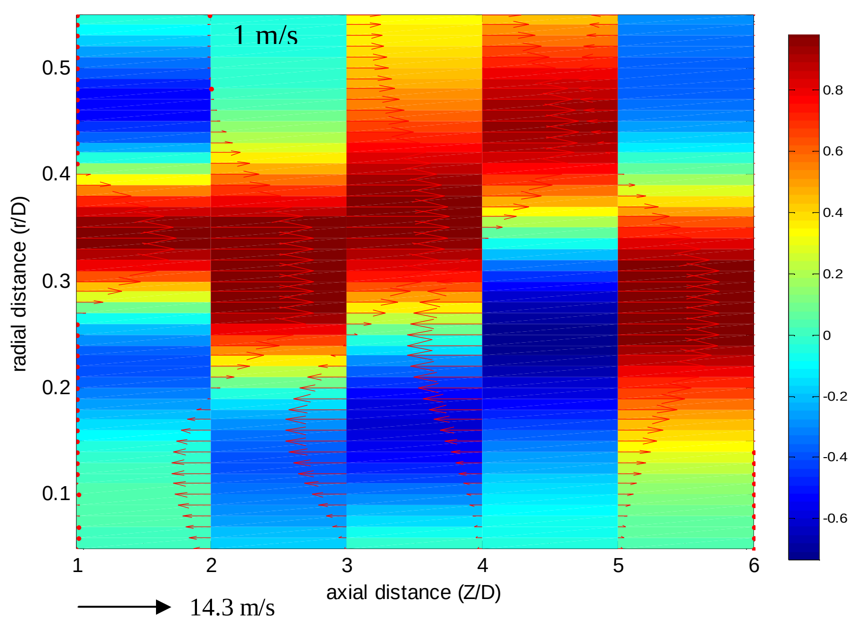

Figure 5.22: Tangential velocity profile of a heated jet at 473 K

The effects directional changes of the tangential velocity and the declining axial core velocity are described by the vorticity in Figure 5.23.

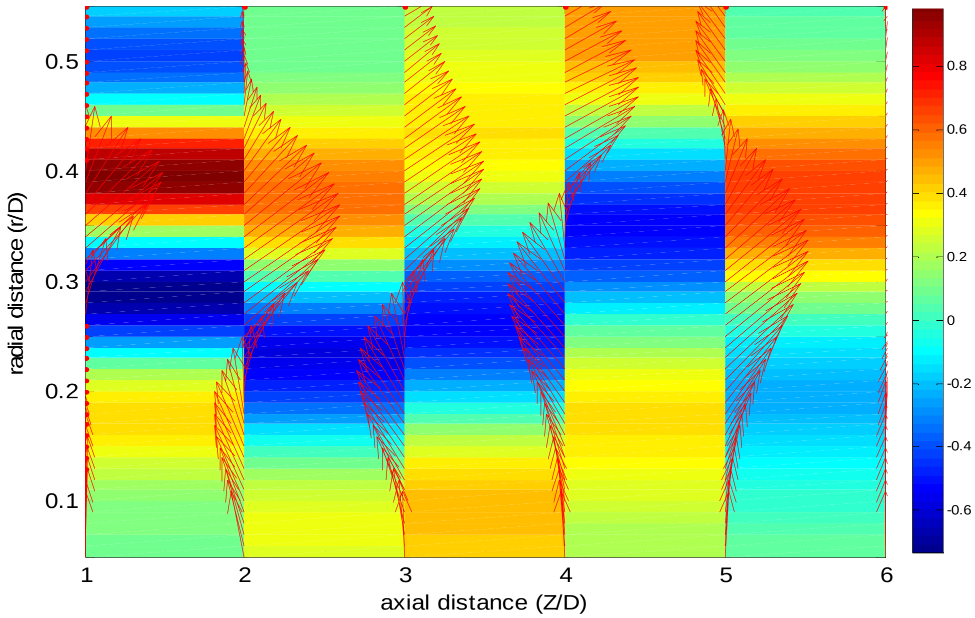

Figure 5.23: The vorticity vector of the injected hot air at 473 K

Figure 5.23 shows vorticity vectors for the velocity profiles of Figure 5.21 and Figure 5.22. Variance of velocity is a component of the flow's kinetic energy. It was used to measure the variances of turbulence. A higher value of fluctuating quantities of axial velocity was recorded at 0.1D to 0.37D along the radial axis. At 0.25D distance along the radial axis was where a maximum variance of tangential velocity measured. Figure 5.24 shows the variance of the radial and axial velocity vectors.

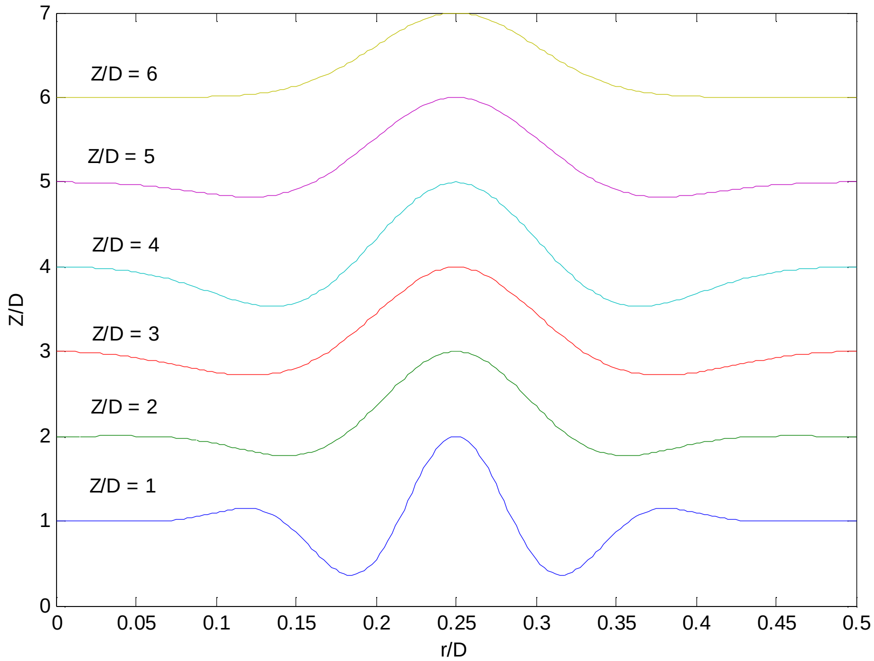

(a)

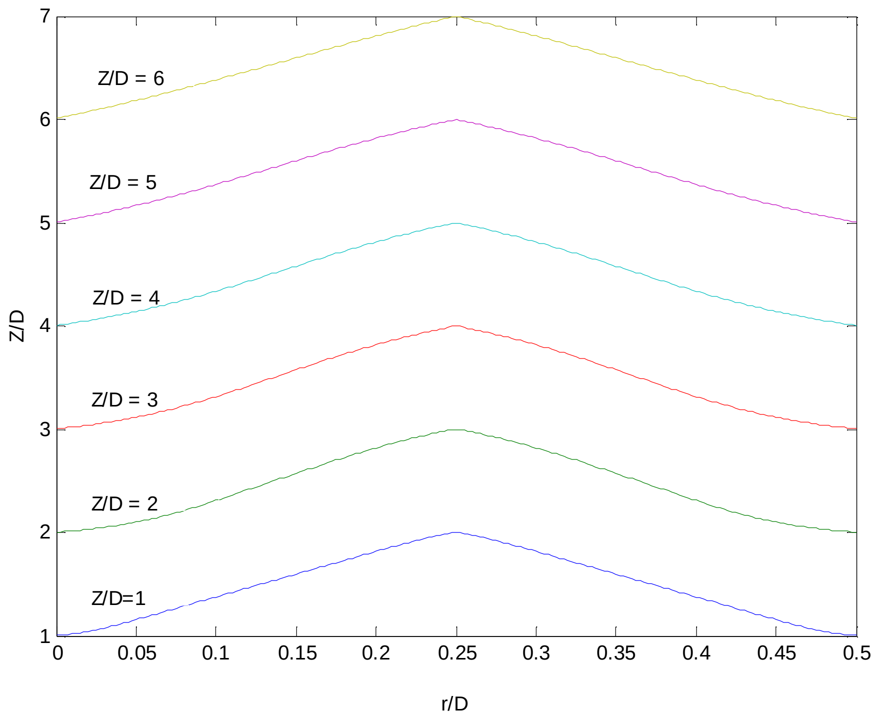

(b)

Figure 5.24: Velocity variance $\overline{v_{\perp i} v_{\perp i}} / U_o$ (a) axial velocity (b) tangential velocity

Turbulence spectra in heated jets are very important information to developers of jet noise prediction tools. Figure 5.25 shows the power spectral density (PSD) of the axial velocity vector at different distances from nozzle. From the figure it is observed that the heated jet noise was more or less independent of the distance and most of the noise intensity values recorded to lie between -40db to -45db.

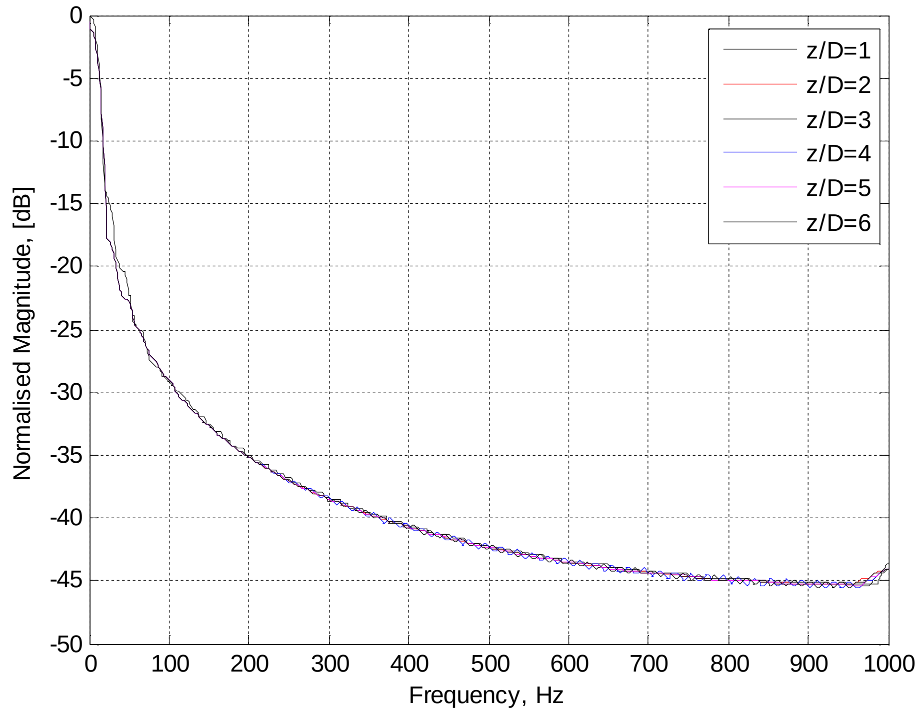

Figure 5.25: Power Spectral density of the axial velocity at T=473 K

The axial and radial velocity measurements using BOS and hot wire anemometry at 323 K is shown at Figure 5.26. The BOS and the hot wire anemometry measurements show a good agreement. Since the hot wire anemometry is a point measurement a measured value sudden jump is observed at certain points.

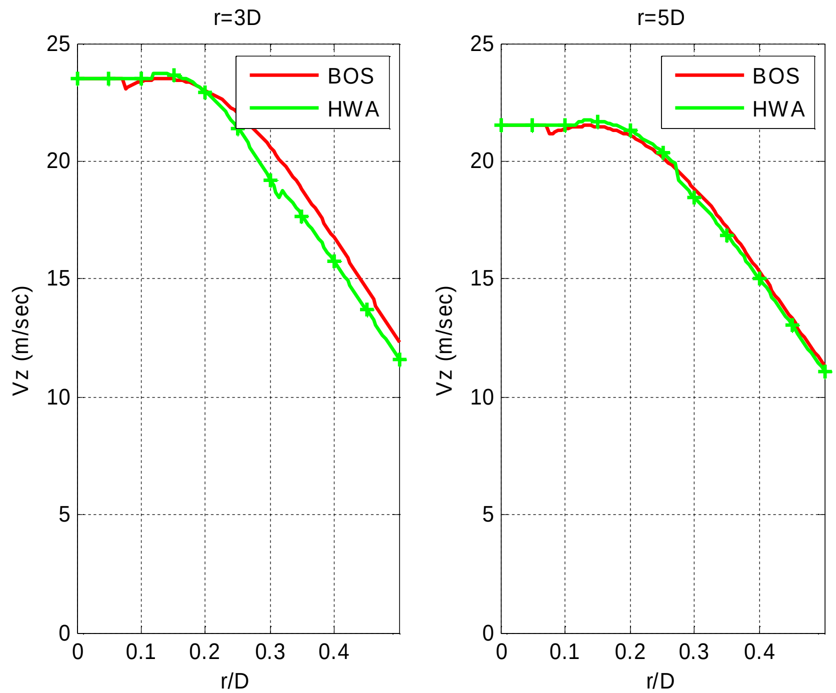

(a)

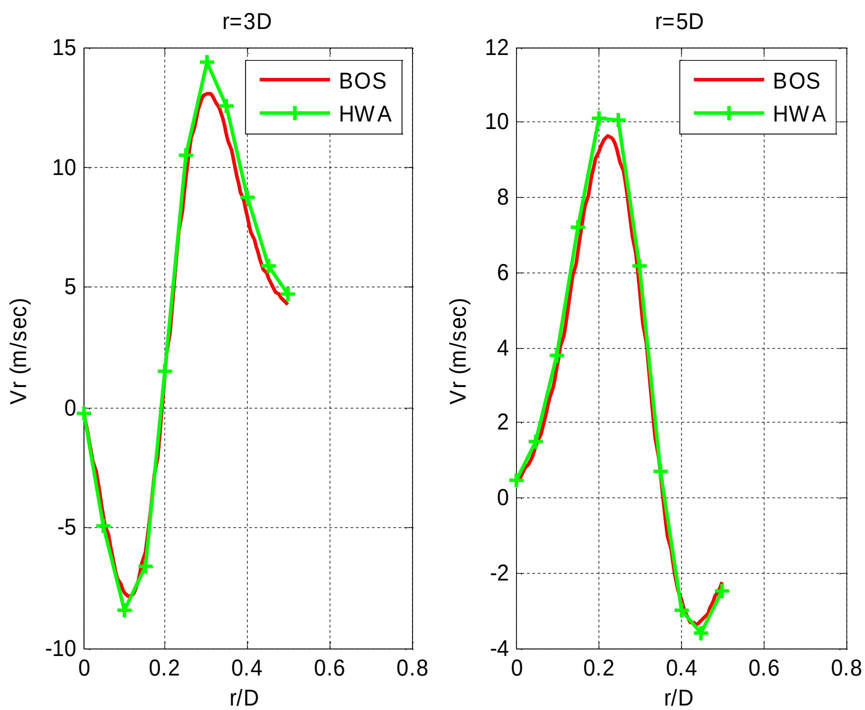

Figure 5.26: (a) axial and (b) tangential velocity measurements using BOS and hot wire anemometry at 323 K exit temperature

The coefficients of variance between the BOS and hot wire anemometry velocity measurements and their derivative parameters were compared with the hot wire anemometry measurements in Table 5.6. The coefficient of variation was calculated as

$$COV = \frac{\sqrt{(\bar{U}_{BOS})^2 - (\bar{U}_{HWA})^2}}{U_{HWA}} X 100\ \% \tag{5.3}$$

where $\bar{U}_{BOS}$ is mean BOS velocity measurement, $\bar{U}_{HWA}$ is mean hot wire anemometry measurement.

As Table 5.5 shows, the radial velocity and the radial velocity variance parameters showed a relatively higher deviations from hot wire anemometry measurements. The calibration temperatures of 302 K and 323 K were selected so as to be below the limiting value for the hot wire of 343 K. A good agreement was achieved between the axial velocity parameters and the probe measurements.

Table 5.5: COV of different velocity parameters

Velocity Parameters	COV	
	T=302K	T=323K
Axial velocity	4.287	4.002
Radial Velocity	5.231	5.421
Center line velocity decay	2.877	2.904
$\overline{v_{\perp i} v_{\perp i}} / U_0$ of Axial velocity	4.287	4.002
$\overline{v_{\perp i} v_{\perp i}} / U_o$ of radial velocity	5.231	5.421
PSD of Axial velocity	0.781	0.853

The coefficient of variation of centerline velocity decay at temperatures of 302 K and 323 K is plotted in Figure 5.27. From the figure it can be shown that the results deviation increased after Z=7D. This is because the potential core velocity which was constant in the zone of flow establishment is no longer unvarying. This velocity fluctuation on zone of established flow, which starts from Z=6.2D [104], is believed to be the main cause for the elevated coefficient of variation.

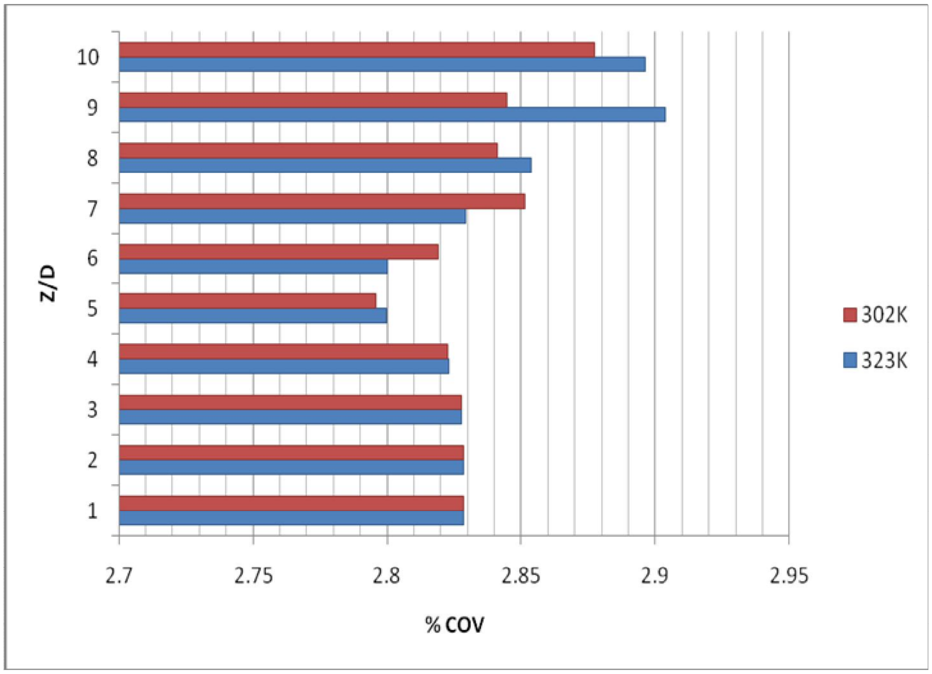

Figure 5.27: Percentage coefficient of variation between BOS and Hot wire anemometry readings of velocity decay at 302 K and 323 K.

The temperature field of the jet at two different perpendicular planes (Z=3D and Z=5D) to the jet axis was measured using BOS and thermocouples. The jet exit temperatures were 423 K, 473 K and 523 K. The BOS results and thermocouple readings were averaged out and their mean temperature results were compared. As compared to BOS temperature data smaller number of thermocouple readings was made. The reason behind small number of thermocouple readings was the slow sensitivity rate of the probe which was 9Hz. Figure 5.28 shows the temperature distribution of the hot jet at 523 K jet exit temperature.

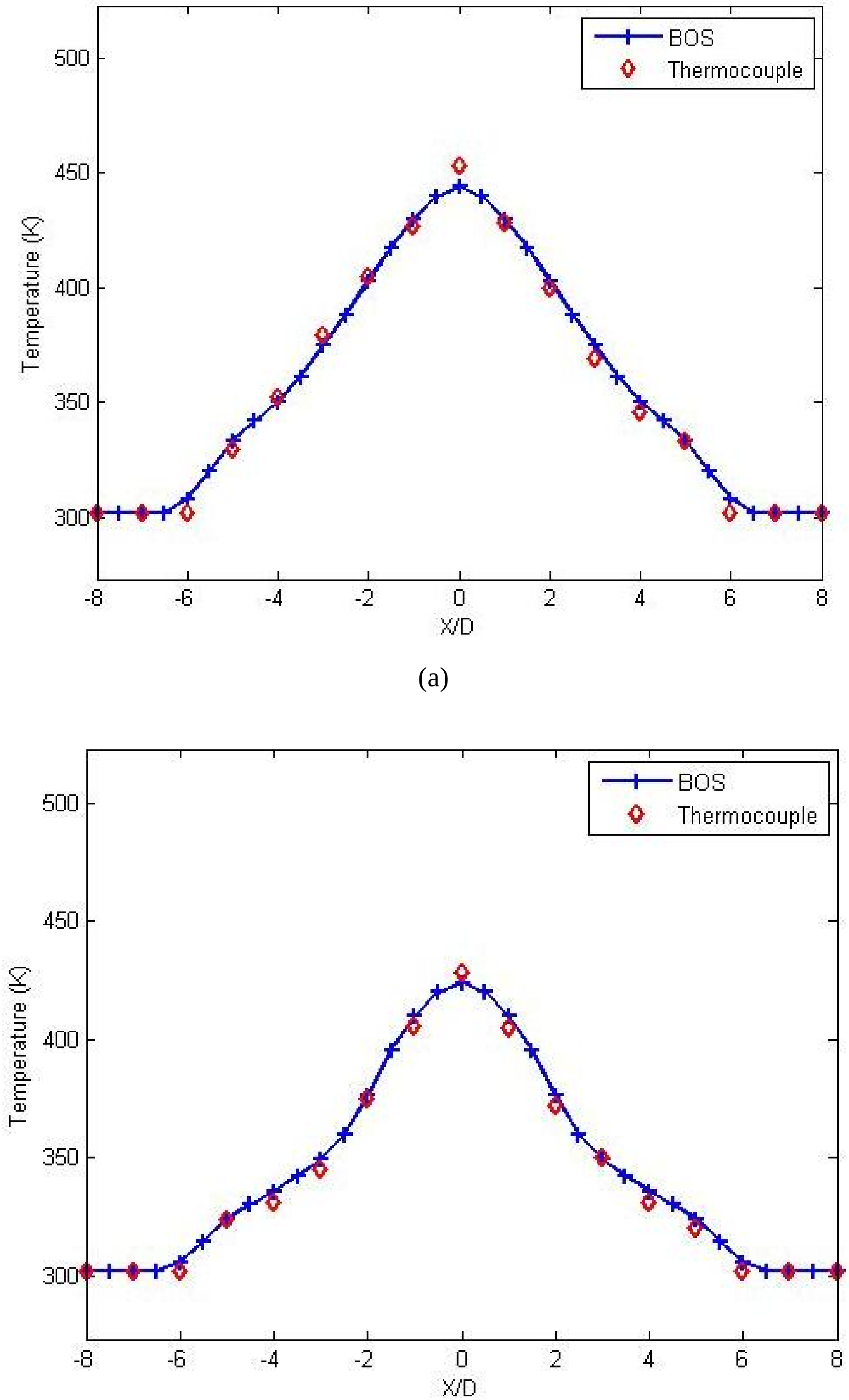

(a)

(b)

Figure 5.28: Temperature field measurement at 523 K (a) at y=0 and Z=3D (b) y=0 and Z=5D

The standard deviation between the BOS and thermocouple results was analysed and shown in Figure 5.29. The figure shows there is a uniform deviation throughout the readings. The maximum standard deviation recorded at 523 K was 2.95 K. This value shows there was a strong agreement between the BOS and thermocouple readings.

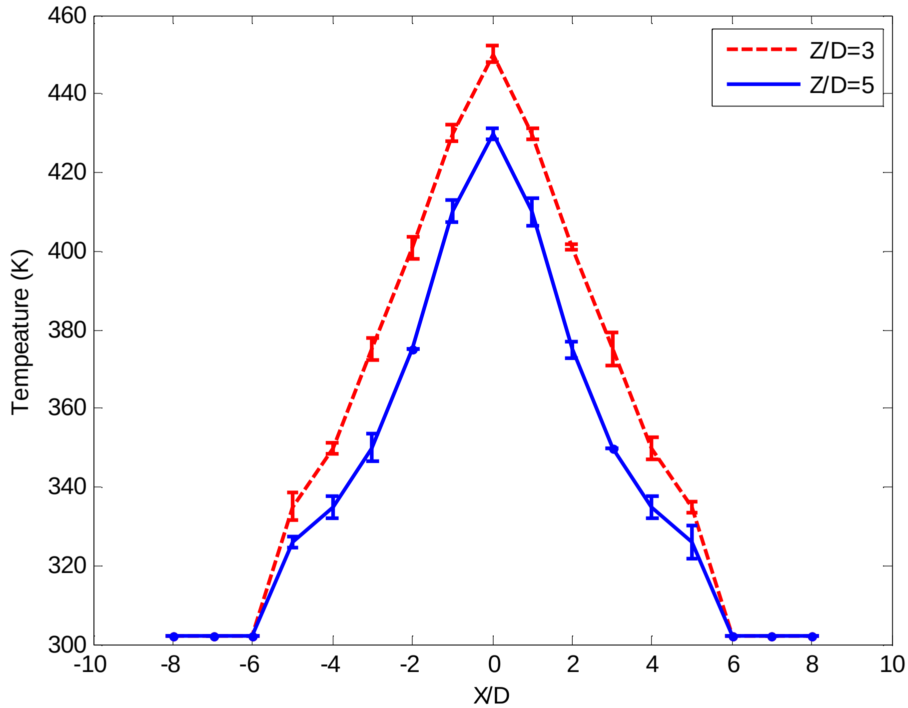

Figure 5.29: Mean temperature and standard deviation between BOS and thermocouple readings at 523 K jet exit temperature

The temperature distributions of jet at exit temperature of 473K in planes 3D and 5D from jet exit nozzle are shown in Figure 5.30. It is shown in Figures 5.28 and 5.30 that the temperature value reduced as the jet exit temperature decreased and as the measuring planes move away from the jet nozzle.

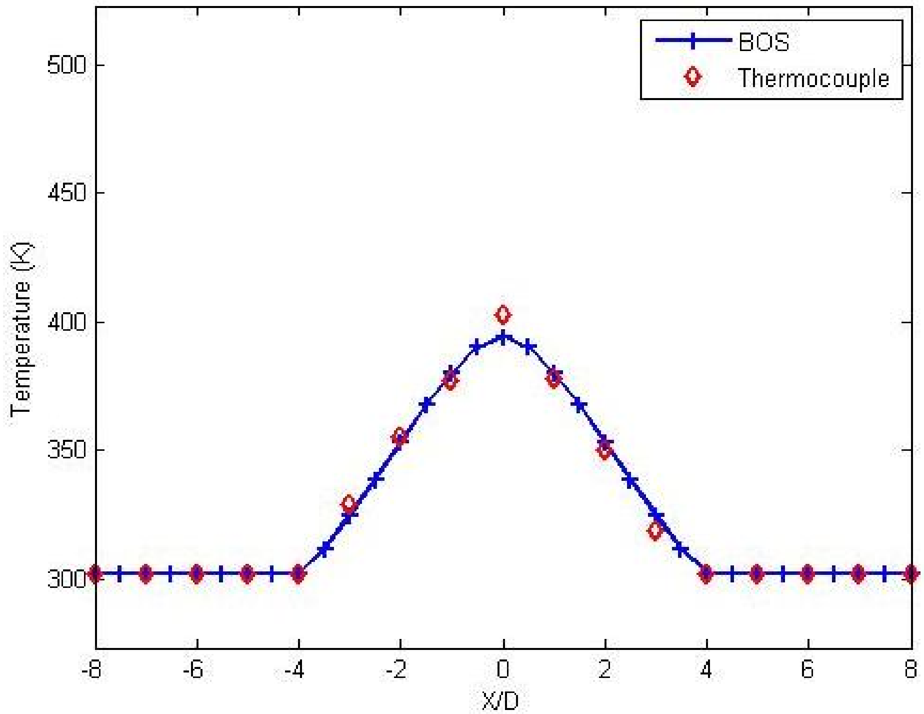

(a)

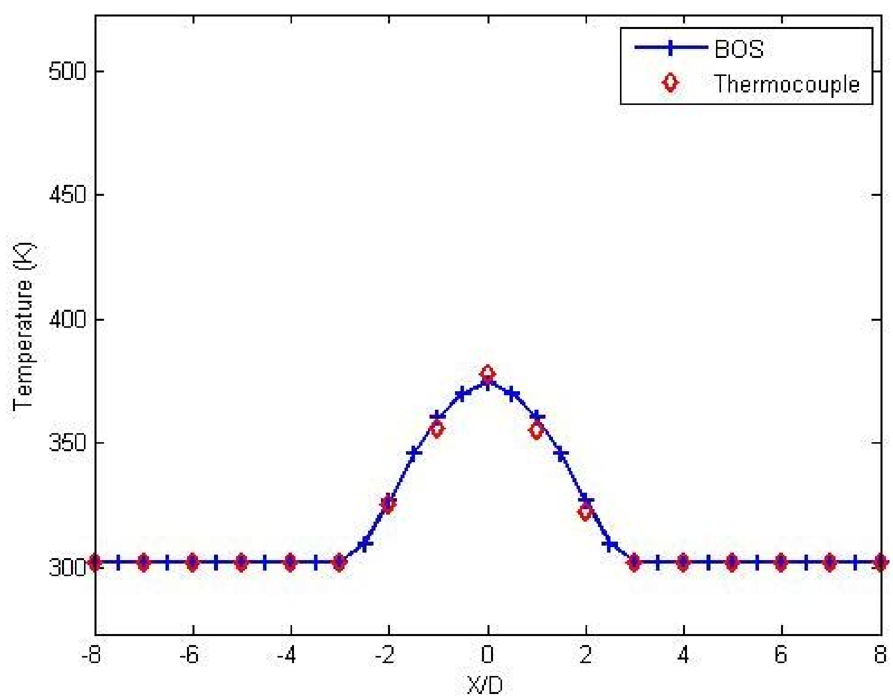

(b)

Figure 5.30: Temperature field measurement at 473 K (a) at y=0 and Z=3D (b) y=0 and Z=5D

Figure 5.31 shows the standard deviation between BOS and thermocouples at 473 K jet exit temperature. An acceptable agreement was achieved between BOS and thermocouple measurements as the maximum deviation observed was of 2.68 K.

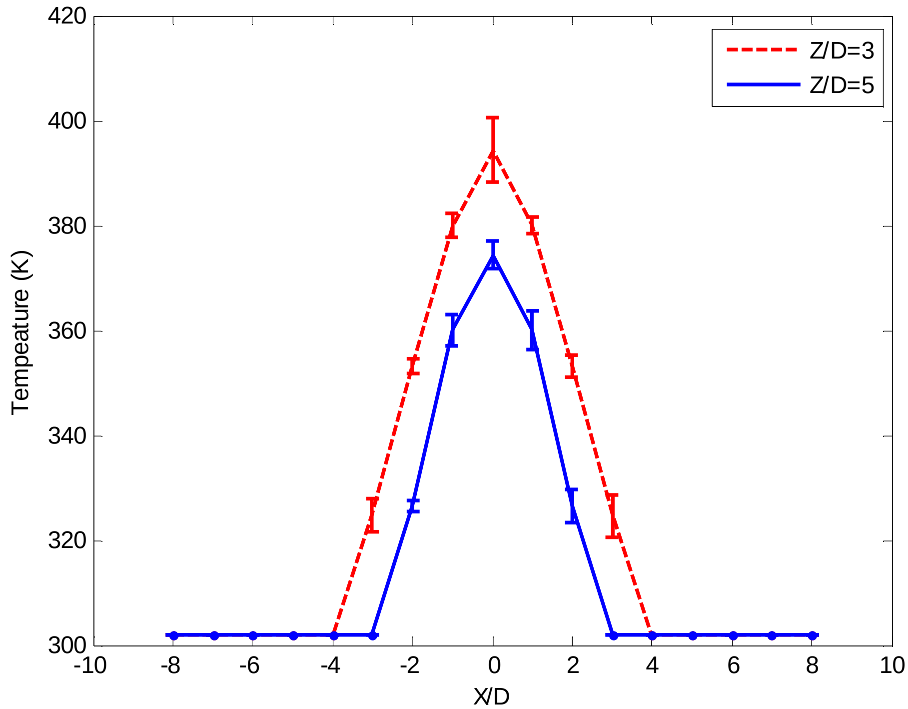

Figure 5.31: standard deviation between BOS and thermocouple readings at 473 K jet exit temperature

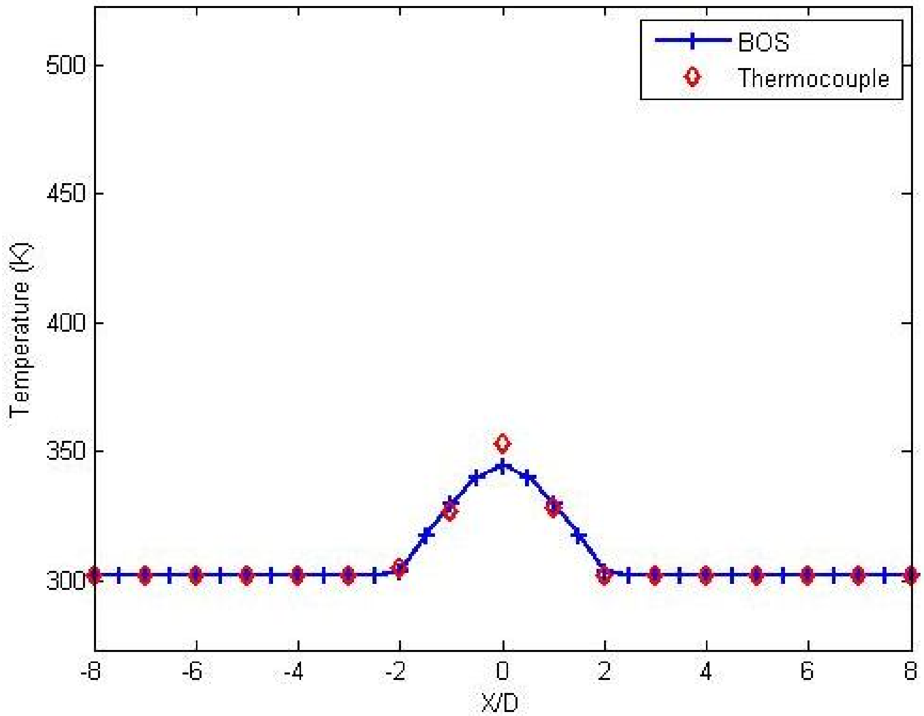

(a)

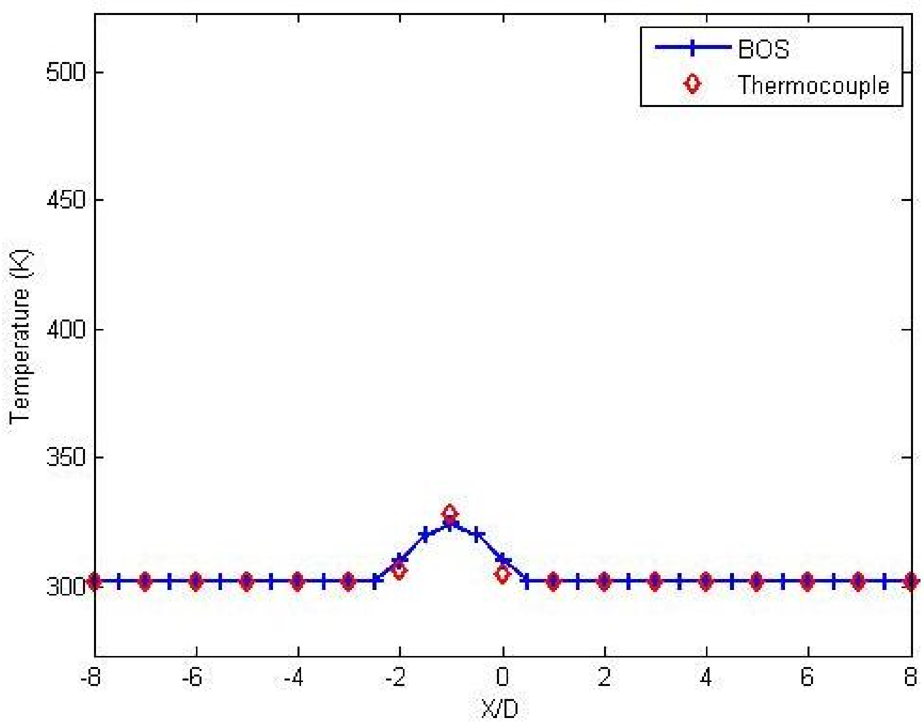

(b)

Figure 5.32: Temperature field measurement at 423 K (a) at y=0 and Z=3D (b) y=0 and Z=5D

The temperature results variation at 423 K, as shown in Figure 5.33, was relatively higher as compared with other standard deviation values computed at elevated exit temperatures. The main reason behind this is quantitative Schlieren techniques use a change in refraction as mode of measuring thermodynamic parameters. This exit temperature of relatively small value (423 K) created smaller change in refraction index which resulted in less sensitive BOS measurement. The non- symmetric velocity profile shown in the Figure 5.33 was believed to arise from BOS Insensitivity when there is a small temperature change.

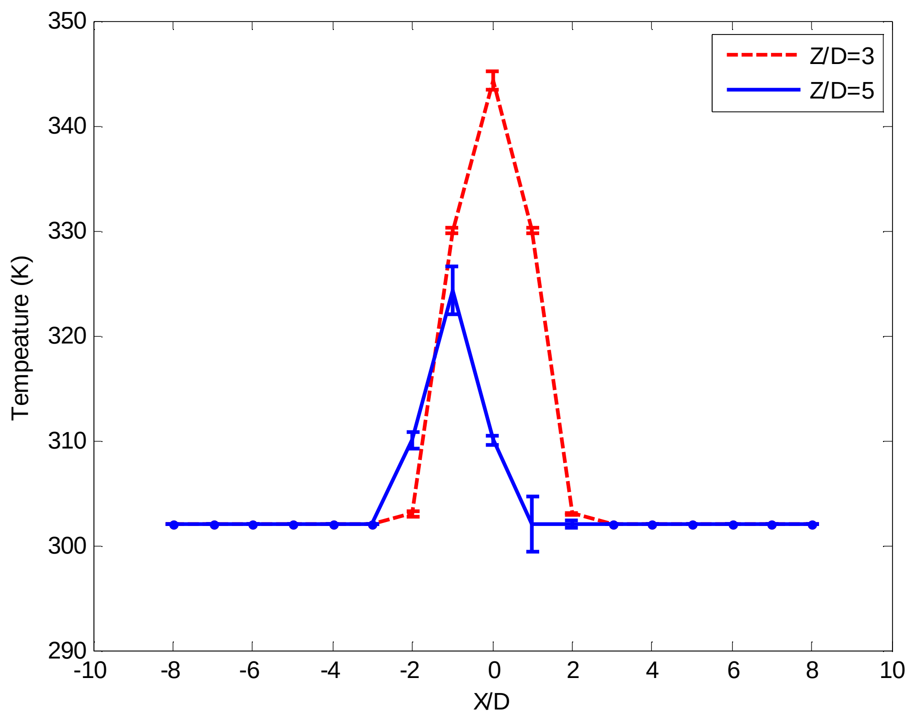

Figure 5.33: Mean temperature and Standard deviation between BOS and thermocouple readings at 423 K jet exit temperature.

5.6 Comparing Results with Other Algorithms

Synthetic data evaluation was made in Section 5.2 and the developed model was shown as the best performing algorithm when compared with other models. In Figure 5.34, the COV between hotwire anemometry and BOS measurements of different algorithms are shown. As it is shown in Figure 5.34, all algorithms have achieved good agreement with the hot wire anemometry measurement. But still the COV of the developed model is the smallest one.

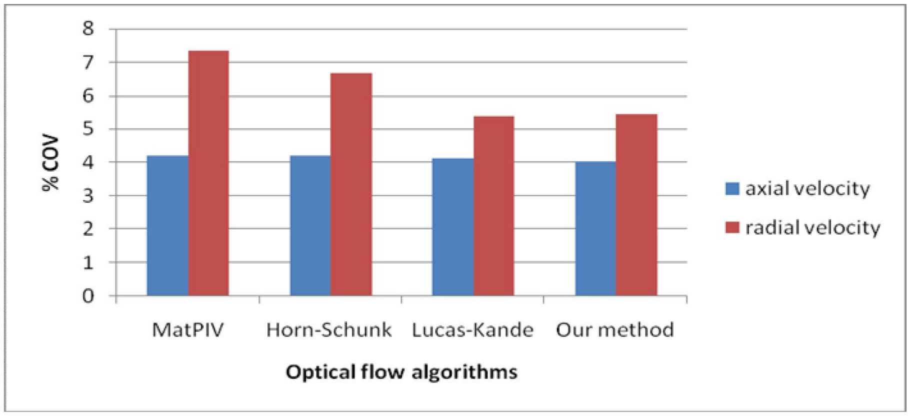

Figure 5.34: Percentage COVbetween hotwire annemometry and BOS measurement using several optical flow algorithms

The flame temperature field measured using BOS with the aid of different optical flow algorithms was compared with thermocouple measurements. The measured standard deviation values are shown in the Figure 5.35. The maximum standard deviation between the developed method and thermocouple reading was 5 K. As it is shown in Figure 5.35, this value was the lowest deviation from the thermocouple reading. Figures 5.34 and 5.35 show the developed model gives superior performance when compared with the existing algorithm.

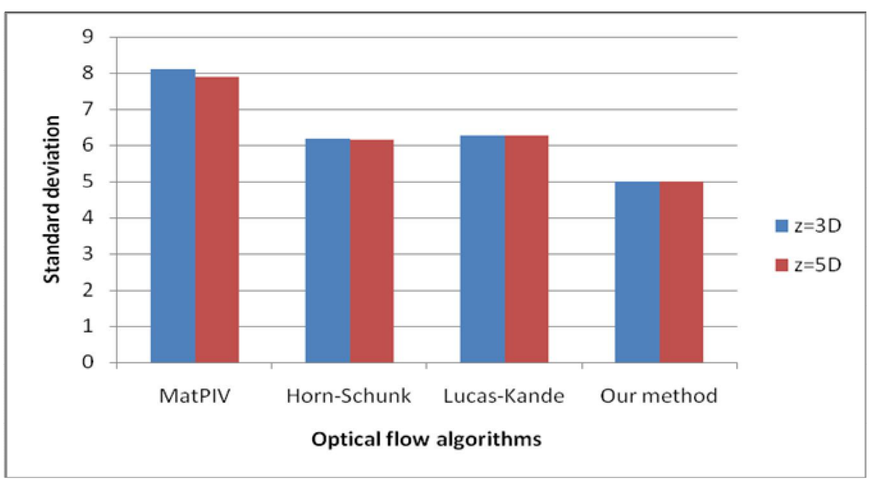

Figure 5.35: Standard deviation between thermocuple reading and BOS measurement using several optical flow algorithms

5.7 Summary

The main findings of this research were shown in this chapter. The developed deflection vector estimation algorithm was tested with several flow conditions. It was also compared with other existing motion estimation algorithms and it gave a superior result especially for flow conditions with considerable different luminosity from surrounding environment.

The BOS experiment was conducted to measure concentration measurements of both reacting and non reacting flows. CNG concentration against the ambient atmosphere was computed and displayed in 0.25 ms time interval. The density distribution of the fuel along the jet axis at maximum tip penetration was also found.

Temperature field measurement was the second thermodynamic parameter extraction carried out under this study. Hot air jet temperature fields were measured at 423 K, 473 K and 523 K and the results were compared with thermocouple readings and a very good agreement was achieved.

Methane flame was used to measure both temperature and mole fractions of the created chemical species. CANTERA, combustion modelling software, was used to estimate chemical species produced by assuming fast reaction between the methane and the air. Based on species concentration calculated by CANTERA and BOS index of refraction measurements, the CO_2 spatial and temporal distributions were computed and plotted.

The temperature fields of the methane flame at two perpendicular planes to the flame axis were measured and compared with thermocouple readings. Once again, the BOS results showed superior agreement with thermocouple readings.

The experiment was extended to estimate the velocity vector field of a hot round jet. The temperature and velocity readings were compared with thermocouple and hot wire anemometry values respectively and a good agreement was achieved.

CHAPTER 6

CONCLUSIONS AND RECOMMENDATIONS

This thesis addressed developing an optical diagnostic tool in the form of Background Oriented Schlieren (BOS). The main novel tasks of this thesis were developing a new optical flow algorithm that can be used in several lighting conditions, multiple thermodynamic parameters extraction and to further extend BOS to measure velocity fields.

6.1 Conclusions

The first task under this study was addressing main optical flow assumptions, i.e, 'the change in intensity between successive images is due to motion of the object features only' and 'the flow of a certain point and its neighbourhood pixels experience a pure translation motion.' It was shown that these assumptions can't sufficiently be used for many BOS applications. It was also shown how the flow conditions of different luminosity affects the background image intensity values in BOS. A method of computing the optical flow equation that considers the intensity variation and both translational and rotational motions of the background feature was proposed. Three different flow conditions, positioned between the camera and the background, were applied to study their effect on varying the intensity values.

The original optical flow equation was modified to incorporate change in intensity and the unknowns of the optical flow equation are computed using wavelet based multi-resolution analysis. The background feature displacement created by these three flows, i.e, injected natural gas, natural gas flame and smoke from fog generator, are computed with the commonly used BOS optical flow algorithms and our modified algorithm. The results have shown flows with self luminosity and high index of refraction tend to significantly vary the background intensity. The incorporated rotational term in the motion estimation field enhanced the accuracy of the algorithm for spurious flow fields like the generated fog. Based on these findings the modified optical flow algorithm gave better results as compared with other existing techniques.

BOS was implemented to measure the concentration of CNG injected jet and open flame. The CNG fuel was injected to a constant volume chamber; the variation index of refraction it created in the transfer function was deconvoluted by the developed optical flow algorithm. The displacement fields obtained based on the optical flow algorithm were validated using synthetic data evaluation. The acquired deflection vector was adapted to index of refraction by means of geometrical optics equation and computed tomography. Gladstone–Dale equation for mixture of gases is used to find out the CNG fuel concentration. Various concentration values at different planes of the jet were computed and displayed.

The spatial and temporal variation of concentration and temperature fields of an open flame was conducted. CANTERA was used to study the possible chemical species created while the methane was burned in the atmosphere. Fifty new species were found. Based on the quantity of their mole fraction 11 species, which constituent a mole fraction of 0.967, was selected and their index of refraction was calculated. This calculated index of refraction was compared with BOS refraction index. Based on this comparison, the amount and locations of CO2, mole fraction distributions of the methane flame were obtained. Mean while, the temperature distribution of the flame was computed. The calculated temperature field, which was found based on the mole fraction of the species, was compared with thermocouple reading and a good agreement was achieved

The BOS technique was further extended to measure the velocity field of a hot air jet. Both rotational and translational motions and the light intensity variations were considered during deflection vector estimation. The axial and the radial velocity terms are derived from the density field measured. Axi- symmetry was assumed based on SSIM criteria.

The axial and radial velocity fields at jet exit temperatures of 302K and 323K were compared with hot wire anemometry measurements. The axial velocity correlation with the probe measurement was found to be better than the radial velocity measurement. The reason behind this was the radial velocity's requirement of additional computational procedures on the already obtained axial velocity data. The velocity information was extracted by manipulating the pairs of BOS images with less than RMSE value of 6. The velocity results obtained showed that quantitative Schlieren was extended to enable the measurement of velocity field accurately.

6.2 Suggestions for Future Works

This study was devoted to develop a tool that extracts multiple thermodynamic parameters. And it is recommended that, the developed technique can be implemented to study the behaviours and variations of flow characteristics.

Usage of several backgrounds and imaging instrument helps in order to get sufficient number of projections of the flow images. This will help to apply BOS for any type of flows other than axi-symmetric flows.

BOS can be employed to study the shock wave propagating out from the explosion center. Successive images before and during the explosion show disturbances caused by the gaseous fireball of the explosion. This technique could be used to track the spherical shock wave propagation away from the explosion center in order to characterize the explosive yield. The developed method can also be applied to visualize flows and perform measurements of shock structures like the vorticity and aerodynamic flow charactherstics created near tip vortex. This area of study is of immense practical importance to aeronautical science and technology.

The assumptions taken during chemical species computations: a chemical equilibrium is attained and the chemical reaction is adiabatic might be preliminary assumptions. A chemical reaction studying model that account for non equilibrium and other thermodynamic phases can give a better result.

REFERENCES

[1] M. Gad-El-Hak, *Flow Control: Passive, Active, and Reactive Flow Management,* Cambridge University Press, London, UK, 2000.

[2] G.S. Settles, *Schlieren and shadowgraph techniques: Visualizing phenomena in transparent media*, Berlin:Springer-Verlag, 2001.

[3] P. Krehl and S. Engemann P. Krehl and S. Engemann "August Toepler — The first who visualized shock waves", *Shock Waves* Vol 5, (1-2), pp1-18, 1995.

[4] B. Atcheson *Schlieren-Based Flow Imaging,* MSC Dissertation, The University Of British Columbia, Canada. 2007.

[5] H. Schardin, "Schlieren Methods and Their Applications," NASA TT-F-12731 (Apr. 1970) [translation from Ergeb. Exakten Naturewiss. 20, 303 (1942)].

[6] P. Peterson, Schlieren and Shadowgraph Photography, Retrieved September 2010, http://encyclopedia.jrank.org/articles/pages/1182/Schlieren-and-shadowgraph-Photography.html,

[7] W. J. Yang, *Handbook of Flow Visualization* 2nd Edition, CRC Press. NY, USA, 2001.

[8] J.V. Pastor, J. M.Garcia, S. Molina, "Analysis Methodology of Diesel Spray and Flame by Means of In-Cylinder Endoscopic Imaging," *The institution of Electrical Engineers, IEE*, Savoy Place, London WC2R 0BL, UK, 2000.

[9] R. Sellens, R. Delijouravesh, "*Non-Orthogonal Optical Spray Pattern Analysis,*" Technical report, Department of Mechanical Engineering, Queen's University, Kingston, Canada, 2000.

[10] J. Shao, Y. Yan "Digital Imaging Based Measurement of Diesel Spray Characteristics" *IMTC 2006 – Instrumentation and Measurement Technology Conference* Sorrento, Italy, 2006.

[11] J. Shao, Y. Yan, "Digital Imaging Based Measurement of Diesel Spray Characteristics," *IEEE Trans. on Instrumentation and Measurement*, 57(9), 2008.

[12] C. Petit, M. Joulin, W. Reckers., “Characterization of Diesel Spray Images Using the Logarithmic Image Processing Framework,” *Image Anal Stereol* 26, 145-155, 2007.

[13] K. R. Kunkulagunta, “Video imaging and Analysis of Common Rail Sprays in an Optical Engine Using Shadowgraphy Technique,” *SAE Paper No 2000-01-1255*, 2000.

[14] A. C. Eckbreth, *Laser diagnostics for combustion temperature and species*, (2nd ed.). New York: Gordon and Breach: Combustion Science and Technology Series, 1996.

[15] A. F. Milke, *Development of a Molecular Rayleigh Scattering Diagnostic For Simultaneous Time-Resolved Measurement of Temprature, Velocity and Density*, Doctoral Dissertation, Case Western Reserve University, USA, 2008.

[16] J. N. Forkey, W. R. Lempert, R. B. Miles, “Accuracy limits for planar measurements of flow field velocity, temperature and pressure using filtered Rayleigh scattering”, *Exp. Fluids*, 24, 151-162, 1998.

[17] N. J, Dam, M. Rodenburg, R. A .L. Tolboom, G.G.M. Stoffels., P.M. Huisman-Kleinherenbrink , J.J. ter Meulen , “Imaging of an underexpanded nozzle flow by UV laser Rayleigh scattering,” *Exp. in Fluids,* 24, 93-101, 1998.

[18] J. Panda, C. R. Gomez, “Setting up a Rayleigh Scattering Based Flow Measuring System in a Large Nozzle Testing Facility”, NASA*/TM 2002-211985*, 2003.

[19] J. Kojima, Q. V. Nguyen, “Measurement and simulation of spontaneous Raman scattering in high-pressure fuel-rich H_2-air flames,” *Meas. Sci. Tech*., 15, 565-580, 2004.

[20] Dantec Dynamics, Laser Optical Measurement systems and Sensors, Retrieved on 2 July 2010, www.dantecdynamics.com,

[21] H. Zhao, N. Landomatos, *Engine Combustion Instrumentation and Diagnostics,* Society of Automotive Engineers. Warrendale, 2001.

[22] W. Paa, D. Müller, H. Stafast, W. Treibel, “Flame turbulences recorded at 1kHz using planar laser induced fluorescence upon hot band excitation of OH radicals,” *Appl. Phys. B,* 86, 1–5, 2007.

[23] N. Jiang, *Development of high repetition rate NO planar laser induced fluorescence imaging,* Doctoral Dissertation, Ohio State University, Columbus, OH, 2006.

[24] K. Verbiezen, A.J. Donkerbroek, R. J. H. Klein-Douwel, A.P. van Vilet , P.J.M. Frijters, X. L. J. Seykens , R.S.G. Baert, W. L. Meerts, N. J. Dam, J.J. ter Meulen, “Diesel Composition: In cylinder NO Concentrations in Relation to Injection Timing” *Combustion and Flame* 151, 333-346, 2007.

[25] B. S. Thurow, N. Jiang, W. R. Lempert and M. Samimy, “Development of a megahertz-rate planar doppler velocimetry for high-speed flows” *AIAA Journal*, 43, 500-511, 2005.

[26] R. L. McKenzie,” Measurement capabilities of planar Doppler velocimetry using pulsed lasers,” *Appl. Optics*, 35, 948-964, 1996.

[27] M. P. Wernet, “Planar particle imaging doppler velocimetry: a hybrid PIV/DGV technique for three-component velocity measurements,” *Meas. Sci. Technol.*, 15, 2011-2028, 2004.

[28] M. Raffel , C. Willert , J. Kompenhans, *Particle Image Velocimetry: A Practical Guide*, Springer-Verlag, Berlin, Germany, 2007.

[29] M. Skotinov, *Quantitative Schlieren methods in gas Dynamics* Nauka, Moskow USSR, 1st edition, 1976.

[30] K. Al-Ammar, A. K. Agrawal, S. R. Gollahalli, D. Griffin, “Application of Rainbow Schlieren deflectometry for concentration Measurements in an Axisymmetric Helium Jet,” *Exp.Fluids* 25, 89-95, 1999.

[31] D. C. Oren, R. P. Durrett and C. R. Ferguson, “Bullseye color schlieren flow visualization” *Exp. Fluids*, 6(6) 357-364, 1988.

[32] G. S. Settles, "Colour-Coding Schlieren Techniques for the Optical Study of Heat and Fluid Flow," *International Journal of Heat and Fluid Flow*, 6 (1), 3-15, 1985.

[33] J. Rheinberg, J. Roy, “on an addition to the metjods of microscopal research by an new way of optically producing color contrast between an object and its background or between definite parts of object itself ” *Microscop. Soc.*, 19, 142-156, 1899.

[34] A. F. Ghoneim, C. J. Marek, A. K. Oppenheim, “Modeling Interface Motion of Combustion (MINOC). A computer code for two-dimensional, unsteady turbulent combustion” NASA technical report, *NASA-TP-2132*, 1983.

[35] W. L. Howes, "Rainbow Schlieren," NASA technical report. *NASA TP-2166*, 1983.

[36] W. L. Howes, "Rainbow schlieren and its applications," *Appl. Opt.* 23, 2449-2460, 1984.

[37] P. S. Greenberg, R. B Klimek, and. D. R. Buchele, “Quantitative rainbow schlieren deflectometry” *Appl. Opt.,* 34, (19), 3810-3825, 1995.

[38] N. K. Butuk, “Fluid flow diagnostics using rainbow schlieren imaging and computer tomography” Doctoral Dissertation The University of Oklahoma, 1997.

[39] S. J. Wu, C. Y. Wang, “A Preliminary Study for 2-D Refractive Index Distribution Imaging Based on Color Schlieren Technique” *In Proc. of Pacific Rim Conference*, 2005.

[40] R. P. Satti, “Flow structure of low-density gas jets and gas jet diffusion flames” Doctoral Dissertation, The University of Oklahoma, 2006.

[41] A. K. Agrawal, N. K. Butuk , S. R. Gollahalli, D. Griffin, “Three-Dimensional Rainbow Schlieren Tomography of a Temperature Field in Gas Flows,” *Appl. Opt.*, Vol. 37(3), 479-485, 2007.

[42] S. B., Verma, “Detection of fluctuating density gradient flow field in shock wave boundary layer interactions using laser Schlieren system”, *Exp.Fluids* 32(4), 527-53, 2002.

[43] D. R. Buttsworth, T. L. Ahfock, “A Pulsed LED System for Schileren Flow Visualization”, technical report of Faculty of Engineering & Surveying technical reports, University of southern Queensland, Australia, 2003.

[44] A. J. Pierce and F. K Lu “Laser Alignment Method for Portable Schlieren System” P*roc.of. 39th AIAA Fluid Dynamics Conference*, 22 - 25 June 2009, San Antonio, Texas.

[45] G. E. A Meier, “Hintergrund Schlierenmessverfahren”, *Deutsche Patent-anmeldung*, DE 199 42 856 A1, 1999.

[46] S. B. Dalziel, G. O. Hughes and B. R. Sutherland, "Synthetic Schlieren" *Proc. of 8th International Symposium on Flow Visualization*, Sorrento, Italy, 1-4 September, 1998.

[47] G. S. Settles, "Recent Developments in Schlieren and Shadowgraph Techniques," *Proc. of 14th International Symposium on Flow Visualization*, Dageu, Korea Italy, 21-24 June, 2010.

[48] H. Richard, M. Raffael, J. Kompenhans J,G.E.A. Meier, "Demonstartion of the Pplicability of a background Oriented Schlieren (BOS) Method" *Proc. of 10th Int Symp Appl Laser Techniques to Fluid Mechanics*, Lisbon, Portugal, 2000.

[49] H, Richard and M. Raffel, "Principle and applications of the background oriented Schlieren Methods" *Meas. Sci. Technol*, 12, 1576-1585, 2001.

[50] M. Raffel, H. Richard, G. E. A. Meier, "on the applicability of background oriented optical tomography for large scale aerodynamic investigations", *Exp.Fluids* 28, 233-241, 2000

[51] L. Venkatakrishnan and G. E. A. Meier . Density Measurements Using The Background Oriented Schlieren Technique. *Exp. Fluids* , 37, 237-247, 2004.

[52] E. Goldhahn , J. Seume , "Quantitative Measurements of Three-Dimensional Density Fields Using the Background Oriented Schlieren Technique" *Exp Fluids*, 43, 241-249, 2007.

[53] F. Leopold, "The Application of the Colored Background Oriented Schlieren Technique (CBOS) to Free- Flight and In-Flight Measurements" P*roc of. Int. Conf. on Instrumentation in Aerospace Simulation Facilities*, Pacific Groove, CA USA, 2007.

[54] F. Leopold "The Application of the Colored Background Oriented Schlieren Technique (CBOS) to Wind Tunnel, Free-Flight And In-Flight Measurements" *Journal of Flow Visualization and Image Processing*,16 (4), 279-293, 2009.

[55]. J. Feng , K. Okamoto, D. Tsuru, H. Madarame, M. Fumizawa, "Visualization of 3D gas density distribution using optical tomography" *Chemical Engineering Journal* 86, 243–250, 2002.

[56] F. Klinge T. Kirmse, and J. Kompenhans, "Investigation of the density and velocity distribution of a wing tip vortex by means of stereoscopic

Background Oriented Schlieren Method (BOS) and stereoscopic Particle Image Velocimetry (PIV)" *Proc. of 12^th^ International Symposium on Application of Laser Techniques to Fluid Mechanics*, Lisbon, Portugal, 2004.

[57] F. Klinge, "Fluid flow rate determining method, involves tracing spatial offset of density variations based on images taken at different times, and determining local flow rate of fluid from offset and interval of times" Patent document *DE102006047286* (2008).

[58] B. Atcheson, W. Heidrich, and I. Ihrke, "An evaluation of optical flow algorithms for Background oriented Schlieren," *Exp. Fluids*, 46, 467-477, 2008.

[59] J. L. Barron, D.J. Fleet, S.S. Beauchemin, "Performance of optical Flow Techniques" *IJCV*, 12(1), 43-77, 1994.

[60] B. K. P Horn and B. G. Schunuck, "Determining optical flow" *Artificial Intelligence*, 17, 185-203, 1981.

[61] B. D. Lucas and T. Kanade, "An iterative image registration technique with an application to stereo vision" *Proc. of DARPA IU Workshop*, 121-130, 1981.

[62] B. Atcheson, I. Ihrke, W. Heidrich, A. Tevs, D. Bradley, M. Magnor, H. Seidel, , "Time-resolved 3D Capture of Non-stationary Gas Flows", *ACM Trans. Graph*. 27, 5, 1-16, 2008.

[63] T. Brox , A. Bruhn, N. Papenberg, and J. Weickert, "High accuracy optical flow estimation based on a theory for warping" *LNCS*, 3021, 25–36, 2004.

[64] H. Liu, R. Chellappa, and A. Rosenfeld, "Fast two-frame multiscale dense optical flow estimation using discrete wavelet filters" *J. Opt. Soc. Am. A*, 20(8), 1505-1515, 2003.

[65] S. Rakshit and C. H. Anderson , "Computation of Optical Flow Using Basis Functions" *IEEE Trans. Image Processing*, 6(9), pp. 1246-1254,1997.

[66] J. N. Pan, Y. Q. Shi, and C. Q. Shu, "Correlation-Feedback Technique in Optical Flow Determination" *IEEE Trans. Image Processing*, 7(7), pp. 1061-1067, 1998.

[67] Vasudeva G., Honnery D R, Soria J, " Non Intrusive Measurement of a Density Field Using a Background Oriented Schlieren", *Proc. of 4th*

Australian conference on Laser Diagnostic in Fluid Mechanics and Combustion, University of Adelaide, Australia,2005.

[68] G. E. A. Meier GEA, (2002) "Computerized Background Oriented Schlieren", *Exp. Fluids,* 33. 181-187, 2002.

[69] U. Kopf, "Application of speckling for measuring the deflection of laser light by phase objects", *Opt. Commun*., 5, 347-350, 1972.

[70] B. R. Sutherland, S. B. Dalziel , G. O. Hughes , P. F. Linden "Visualization and measurement of internal gravity waves by 'Synthetic Schlieren', part I: Vertically oscillating cylinder", *J Fluid Mech* 390:93–126, 1999.

[71] Augenstein, E., Leopold, F., Richard, H., Raffel, "The background oriented schlieren method versus visualization with holographic filters", *Proc. of 4th international symposium on particle image velocimetry*, Göttingen, Germany, 2001.

[72] F. Klinge and M. Reithmuller, "Local density information on application obtained by means of background oriented schlieren(BOS) method" *Proc of 11th International Symposium on Application of Laser Technology to Fluid Mechanics*, Lisbon, Portugal 2002.

[73] G.E. Elsinga, B.W. van Oudheusden, F. Scarano, D.W. Watt "Assessment and application of quantitative schlieren methods: Calibrated color schlieren and background oriented schlieren," *Exp. Fluids* 36, 309–325, 2004.

[74] K. Kindler E. Goldhahn F. Leopold M. Raffel "Recent developments in background oriented Schlieren methods for rotor blade tip vortex measurements," *Exp. Fluids* 43, 233–240,2007.

[75] K. Berger, I. Ihrke, B. Atcheson, W. Heidrich, M. Magnor, "Tomographic 4D Reconstruction of Gas Flows in the Presence of Occluders," *Proc. of the Vision, Modeling, and Visualization Workshop*, Braunschweig, Germany, November 16-18, 2009.

[76] L. Baur J. Tapee, "Background Oriented Schlieren" *Technical Report AAE 490R/590R,* Purdue University, 2002.

[77] M. J. Hargather G. S. Settles "Natural-background-oriented schlieren imaging", *Exp Fluids* 48, 59–68, 2010.

[78] A. Bichal, B. Thurow, “Development of a Background Oriented Schlieren Based Wavefront Sensor for Aero-Optics”, *40th Fluid Dynamics Conference and Exhibit 28* Chicago, Illinois, June - 1 July 2010.

[79] R. C. Gonzalez , R. E. Woods , S. L. Eddins, *Digital Image Processing Using Matlab*, Pearson Prentice Hall, 242-281, New Jersey 2004.

[80] A. J. Smits and T. T. Lim, *Flow Visualization: Techniques and Examples*, Imperial college Press, London, UK, 2000.

[81] C. Gomez-Reino , M.V. Perez , C. Bao , V. Perez, *Gradient-Index Optics: Fundamentals and Applications*, Springer-verlag, New York, 2002

[82] V.Perlick, *Ray Optics, Fermat’s Principle, and Applications to General Relativity* Springer-verlag Berlin, Heidelberg 2000.

[83] M. Bass, *Handbook of Optics*, Vol. I-II" (2nd edition) McGraw-Hill, New York, USA, 1994.

[84] Snell’s Law, Encyclopedia Britanica, Retrieved on Dec, 16, 2010 http://www.britannica.com/EBchecked/ topic/550450/Snells-law

[85] F. Träger, *Springer Handbook of Lasers and Optics* Springer Science+Business Media, LLC New York, 2007.

[86] M. Thomas, S. Misra, C. Kambhamettu and J. T Kirby, “A robust motion estimation algorithm for PIV” *Meas. Sci. Technol*. 16(3), 865-874, 2005.

[87] D. R. Jonassen , G. S. Settles, and M. D.Tronosky , “Schlieren `PIV' for turbulent flows” *Optics and Lasers in Engineering*, 44 (3-4), 190-270, 2005.

[88] S. G. Mallat, “A theory for multi-resolution decomposition: The wavelet representation,” *IEEE Trans. Pattern Anal. Machine Intell*, 11, 674-693, 1989.

[89] C. Bernard, “Discrete Wavelet Analysis: A New Framework for Fast Optic Flow Computation” *Proc. of. European Conf. Computer Vision*, Friburg, Germany, June 2-6, 1998.

[90] X. Pan “Tomographic Image Reconstruction” *proc. of the 41st Annual Meeting of the American Association of Physicists in Medicine*, Nashville, Tennessee, USA July 25-29,1999.

[91] J. Radon Translated by P. C. Parks, “On the Determination of Functions From Their Integral Values Along Certain Manifolds” *IEEE Trans. on Medical Imaging*, MI-5(4), December 1986.

[92] H. M. Hertz “Kerr effect tomography for non-intrusive spatially resolved measurements of asymmetric field distribution” *Appl Opt* 25, 914–921, 1986.

[93] A. C. Kak, M. Slaney *Principles of computerized tomographic imaging*, IEEE, New York, 1988.

[94] W Merzkirch, *Flow Visualization*, Academic, New York, 1987.

[95] D. G. Goodwin, *Cantera User’s Guide*, Division of Engineering and Applied Science California Institute of Technology , Pasadena, CA, 2002.

[96] R.W. Bilger “The structure of diffusion flames”. *Combust Sci Tech* 13, 155–170, 1976

[97] J. E. Bridges and M. P. Wernet, “Effect of Temperature on Jet Velocity Spectra” technical report *NASA/TM—2007-214993*, Glenn Research Center, Cleveland, OH 2007.

[98] R. Cook and T. DeRose, “Wavelet Noise” *ACM Trans. on Graph*, 24(3), 803-811, 2005.

[99] Photron Limited, *FASTCAM-X 1280PCI Hardware Manual*, 2002.

[100] Z. Wang, A. C. Bovik , H. R. Sheikh, and E. P. Simoncelli, “Image Quality Assessment: From Error Visibility to Structural Similarity” IEEE Trans. on Image Processing, 13(4) 2004.

[101] A. Maurel, P. Ern, B.J.A. Zielinska, J. E. Wesfreid, “Experimental study of self-sustained oscillations in a confined jet” *Phys Rev. E* 54, 3643, 1996.

[102] Volume visualization project, retrieved 15 March 2009, http://www.volvis.org

[103] N. J. Dam, M. Rodenburg, R. A. L. Tolboom, G. G. M. Stoffels, P. M. Huisman-Kleinherenbrink and J. J. Ter Meulen, “Imaging of an underexpanded nozzle flow by UV laser Rayleigh scattering” *Exp. Fluids* 24 93-101,1998.

[104] J. H. W. Lee, V. H Chu, *Turbulent jets and plumes - a Lagrangian approach* Kluwer Academic Publishers, Massachusetts, USA, 2003.

PUBLICATIONS

Patent

1. Emishaw D. Iffa and A. Rashid A. Aziz "A Method or Measuring Velocity Field of Compressible Flow of Fluid," PI 2010001427

Peer reviewed journals

1. Emishaw D. Iffa, A. Rashid A. Aziz and Aamir S. Malik "Velocity Field Measurement of a Round Jet using Quantitative Schlieren" Applied Optics, 50(5), 618-625, 2011.
2. Emishaw D. Iffa, A. Rashid A. Aziz and Aamir S. Malik "Concentration measurement of injected gaseous fuel using quantitative schlieren and optical Tomography" Journal of the European Optical Society:RP 5, 10529, (2010).
3. Emishaw D. Iffa, A. Rashid A. Aziz and Aamir S. Malik "Gas Flame Temperature Measurement Using Background Oriented Schlieren" to appear Journal of Applied Sciences.
4. Salah Eldin Mohammed, Emishaw D. Iffa, Masri Bin Baharom, A. Rashid A. Aziz "Spray Characteristic Comparisons of Compressed Natural Gas and Hydrogen fuel Using Digital Imaging" to appear in Journal of Applied Sciences.

SAE Technical paper series

1. Emishaw D. Iffa and A. Rashid A. Aziz "Variable Density Distribution of CNG Jet Injected at Low Injection Pressure" SAE 2009-32-0074

Peer reviewed international conferences

1. Emishaw D. Iffa, A. Rashid A. Aziz and Aamir S. Malik "3D Time Resolved Temperature and Concentration Measurement using Background Oriented

Schlieren Technique " 14th International Symposium on Flow Visualization, Daegu, Korea, June 21-23, 2010.

2. Emishaw D. Iffa, A. Rashid A. Aziz "Gas Flame Temperature Measurement Using Background Oriented Schlieren" The second International Conference on plant equipment and reliability (ICPER) 15-17 June 2010, Kuala Lumpur, Malaysia.
3. Emishaw D. Iffa A. Rashid A. Aziz "A Statistical Evaluation Method of Edge Detection Algorithms for Combustion Spray Images "International Graduate Conference in Engineering and Science (IGCES 2008), J. Bahru, Malaysia, Dec 22-24, 2008.

National Conference

1. Emishaw D. Iffa "Optical and Digital Imaging Applications on Spray and Flame Characterization: Survey" National Postgraduate Conference, Tronoh, Malaysia, March 2009.